3-22-2019

Displacement Damage Effects in GeSn Light Emitting Diodes

Kevin K. Choe

DISPLACEMENT DAMAGE EFFECTS IN GeSn LIGHT EMITTING DIODES

THESIS

Kevin K. Choe, Capt, USAF

AFIT-ENP-MS-19-M-073

DEPARTMENT OF THE AIR FORCE
AIR UNIVERSITY

AIR FORCE INSTITUTE OF TECHNOLOGY

Wright-Patterson Air Force Base, Ohio

AFIT-ENP-MS-19-M-073

DISPLACEMENT DAMAGE EFFECTS IN GeSn LIGHT EMITTING DIODES

THESIS

Presented to the Faculty

Department of Engineering Physics

Graduate School of Engineering and Management

Air Force Institute of Technology

Air University

Air Education and Training Command

in Partial Fulfillment of the Requirements for the

Degree of Master of Science

Kevin K. Choe, BS

Capt, USAF

March 2019

AFIT-ENP-MS-19-M-073

DISPLACEMENT DAMAGE EFFECTS IN GeSn LIGHT EMITTING DIODES

THESIS

Kevin K. Choe, BS
Capt, USAF

Committee Membership:

Michael R. Hogsed, PhD
Chair

John W. McClory, PhD
Member

Buguo Wang, PhD
Member

AFIT-ENP-MS-19-M-073

Abstract

Recent progress in GeSn non-equilibrium growth techniques promises significant near-mid infrared photonic performance compatible with complementary metal oxide semiconductor (CMOS) manufacturing technology. Potential future use on Earth-orbiting satellites requires determination of the suitability of GeSn based photonic devices in high energy proton environments. In this research the electroluminescence (EL) intensity of $Ge_{1-x}Sn_x$ (x = 0, 0.02, 0.069, and 0.094) light emitting diodes was measured before and after irradiation by 2 MeV protons at relatively high fluence levels. Complementary electrical characterization measurements (I-V, C-V, and deep level transient spectroscopy (DLTS)) were also performed to assist with analysis of the EL results, specifically to understand the observed radiation-induced EL degradation percentage as a function of Sn concentration. GeSn devices with higher Sn concentration were up to 10 times more resistant to proton displacement damage than the pure Ge (x = 0) devices. Following exposure to a proton fluence of 4×10^{13} cm^{-2}, the average degradation percentage of the x = 0 and x = 0.094 devices were 47.7% ± 5.8% and 4.7% ± 5.1%, respectively. The most probable mechanism for this trend in EL degradation was inferred through DLTS analysis. In the pure Ge devices, the dominant deep-level defect introduced by proton irradiation was observed as a hole trap located near the middle of the band gap – a condition that maximizes the rate of Shockley Read Hall (SRH) non-radiative recombination. This dominant deep level (attributed to the -/0 transition of the vacancy-phosphorus complex) was observed to maintain an approximately fixed energy

spacing below the indirect conduction band edge. As Sn concentration increased, the band gap decreased, and this dominant defect energy level moved further from the mid-gap level, resulting in less EL degradation. Considering the modest EL degradation observed after irradiation doses equivalent to many years in typical Earth orbits, the results of this research suggest considerable promise for the suitability of GeSn based photonic/optoelectronic devices in space radiation environments.

AFIT-ENP-MS-19-M-073

To my beloved son and daughter. I hope I inspire you both to accomplish your goals in life.

Acknowledgments

I would like to recognize organizations that provided research money, equipment, and the marvelous work support for my research. First, I would like to sincerely thank the Air Force Office of Scientific Research (AFOSR) for providing the 2018 research budget for this particular project. I would like to thank Ohio University (OU) for access to the proton beam time. Also, I would like to express my appreciation to Arizona State University (ASU) for providing Group IV optoelectronic test samples. Without these "back-bone" resources, this research would have not have been possible.

I would like to recognize some bright instructors, scientists, engineers, and technicians who worked with me locally at the Air Force Institute of Technology (AFIT). First, I would like to thank my research advisor, Lt Col Michael Hogsed, who strived to equip me with the knowledge that was necessary to overcome hardships this research presented along the way. I went from knowing very little about radiation effects on electronic devices, to being able to present and solve high level difficulty radiation effects problems on semiconducting materials. I would also like to thank my research committee members, Dr. John McClory and Dr. Buguo Wang, who provided useful advice during this research. Also, I appreciate Jake Miguel, a SOCHE intern student, who assisted with laboratory equipment setup for this research.

Lastly, I would like to express my appreciation to my family. Full dedication to schoolwork could be almost intangible while being a father of two young kids. I was able to give my all with both time and effort to my schoolwork because my wife, Anne Choe, supported me by taking care of two kids. I did not have to worry about anything at home while that strong woman was standing at my side and ensuring everything was taken care of. I would like to thank my son and daughter, Eben and Keeva, who lost their father for the past 18 months to his schoolwork. To my family, thank you for your

support and understanding. I will continue to strive to be a better husband, a better father, and a better scientist.

Kevin K. Choe

Table of Contents

Page

List of Figures

Page

List of Tables

Page

DISPLACEMENT DAMAGE EFFECTS IN GeSn LIGHT EMITTING DIODES

I. Introduction

1.1 Motivation

Because many photonic devices are used in space systems, it is essential to understand how these photonic devices are affected by the space radiation environment. Satellites operate in earth's magnetic field, within the Van Allen belt, where high-energy protons (energy 100 keV to 100 MeV) and electrons (10 keV to 10 MeV) are trapped as shown in Figure 1 [1] [2]; These high energy protons are known to cause displacement damage in satellite electronic components. Optocouplers are important satellite components that rely on light emitting diodes (LEDs) for their function. LEDs vary in design and functionality, and these differences can affect how they respond to radiation environments.

Recently, Germanium-Tin (GeSn) LEDs have been developed, which show promising photonic performance for Sn content exceeding 7% [3]. The growing interest in these group IV materials for electronic applications inevitably requires identifying and understanding the electrical properties of the defects introduced after high energy particle irradiation. High energy protons pose the most significant threat to photonic devices in the near-Earth space environment and are thus most relevant to the intended application of this study.

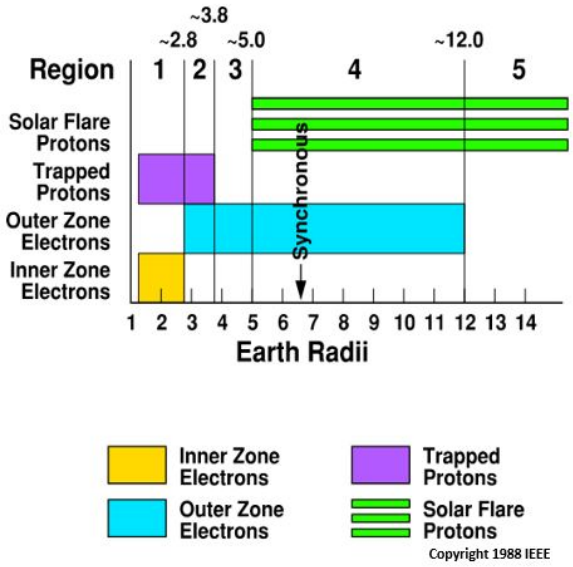

Figure 1. A plot depicting the belt-like structure of particle regions around Earth. Protons (E > 30 MeV) are trapped within approximately 3.8 Earth Radii (1 Earth radius = 6380 km). Reproduced with permission from [1].

Although neutron radiation effects in some GeSn thin films were studied in 2016, proton radiation effects had not been investigated. The primary investigation method used in 2016 was photoluminescence (PL), a technique that can provide insight into the material optical properties, but not device-level performance. Electroluminescence (EL) results from recombination of electrically-induced (pumped) electron-hole pairs (EHP). Although this luminescence mechanism is similar to PL, EL is more representative of the intended device function, and is thus the preferred technique in the present study.

1.2 Research Purpose

High energy protons and other forms of particle radiation cause deep-level defects, which create non-radiative recombination paths in semiconductor materials. This mechanism degrades the luminescence efficiency (corresponding to decreased intensity of emitted light) of photonic devices. The purpose of this research was to quantify and

explain the degradation in EL emitted from GeSn LEDs due to radiation (proton)-induced deep-level defects, with particular focus on the effect of Sn content.

1.2.1 EL Objectives

Quantifying EL degradation (due to controlled defect concentrations) in GeSn LEDs of varying Sn content was the core objective of this research, however, an EL measurement capability suitable for this research did not already exist at AFIT. Hence, the preliminary objective of this research was to construct an EL measurement system. In order to realize such capability, the following objectives had to be accomplished: (1) discover proper experimental setup (i.e. building device schematics and planning experimental procedures) and acquire laboratory equipment and devices; (2) find equipment parameters (i.e. define appropriate duty cycle) which could apply an appropriate level of bias and current to samples (large enough to rectify and induce optimum luminescence for measurements but not so large as to exceed the threshold for electrically harming the samples); (3) define the measurement parameters which could provide results that could be tied to ongoing deep level transient spectroscopy (DLTS) analysis.

1.2.2 DLTS Objectives

If EL results quantitively demonstrate a light output degradation trend in test samples, DLTS results can help determine which deep-level defects dominate the non-radiative recombination process. Deep-level defects, in particular, decrease the radiative efficiency of light emitting diodes. Such defects are often associated with the displacement damage that accumulates in certain radiation environments. Much is

known about defect properties in pure Ge and some data have been published on defect properties in Ge-Sn [4] [5] [6], but very little is known about the dependence of these properties on Sn concentration. It is unknown whether the impurity defects due to Sn doping or vacancy defects caused by proton displacement damage contribute more to the degradation of the electrical property (results shown in the EL study). Typical DLTS analysis is capable of detecting the dominant majority/minority carrier traps, respectively, in both the traditional fashion and the current injection mode.

II. Theory

2.1 Group IV LED

GeSn has been recently highlighted as a cutting-edge group IV semiconductor material. Sn is known as a zero-band gap semiconductor (E_g = 0 eV), and the only element in group IV with a direct gap (lowest transaction at wave vector k = 0); thus, it is classified as a semiconductor since a finite band gap appears at some points in momentum space. Ge has an indirect band gap of 0.66 eV and a direct band gap of 0.8 eV for a difference of 0.14 eV [7]. The various band gap energies of the GeSn alloys used in this study (depending on Sn content) are listed in Table 1.

Table 1. Device intrinsic region properties

Sn Conc. [mol. %]	Carrier Conc./ type [cm^{-3}]	Thickness [nm]	Strain [%] "-/+" compressive/ tensile	Band gap at 295 K [eV]
0.0	5×10^{16}	790	+ 0.11	0.66
2.0	2×10^{16}	530	- 0.14	0.62
6.9	2×10^{17}	400	- 0.22	0.54
9.4	2×10^{17}	300	-0.32	0.46

Fundamentally, Ge is a well-known indirect (band gap) semiconductor; its crystal momentum in the Brillouin zone of the bottom of the conduction band and the top of the valence band are not aligned as shown in Figure 2. In an indirect semiconductor, phonons are required to exchange momentum with transitioning electrons. Hence, when phonon-induced recombination occurs, excitation energy is generally released in heat form (thermal energy) in non-radiative recombination.

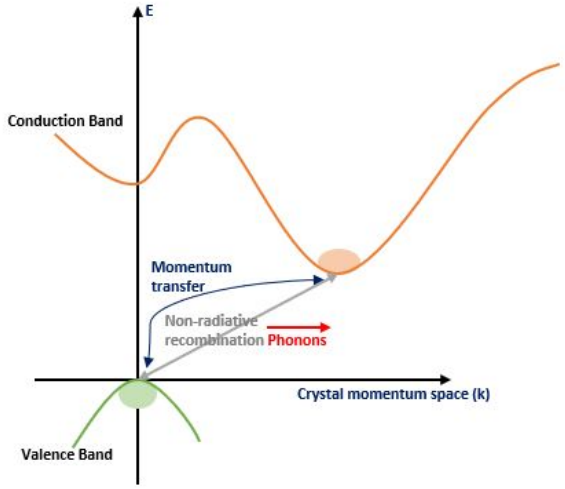

Figure 2. An E-k plot visualization of non-radiative recombination in indirect semiconductors. E shows the energy level of the semiconductor and k is related to the crystal momentum of the semiconductor. Reproduced with permission from [8].

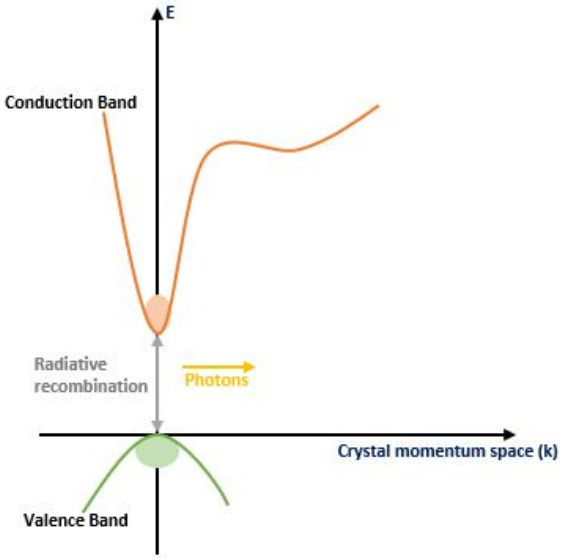

Figure 3. An E-k plot visualization of radiative recombination in direct semiconductors. EHP recombinations in direct semiconductors result in light emission. Reproduced with permission from [8].

On the other hand, electron-transitions between the bands do not require phonon-assisted momentum exchange if the crystal momentum in the Brillouin zone of the bottom of the conduction band and the top of the valence band is aligned as shown in

Figure 3. As a result of EHP recombination in direct (band gap) semiconductors, such as group III-V materials, excitation energy gets released in the form of light (i.e. photons). This recombination process is known as "radiative recombination". Therefore, radiative recombination is a required feature for all photonic devices and EL measurements.

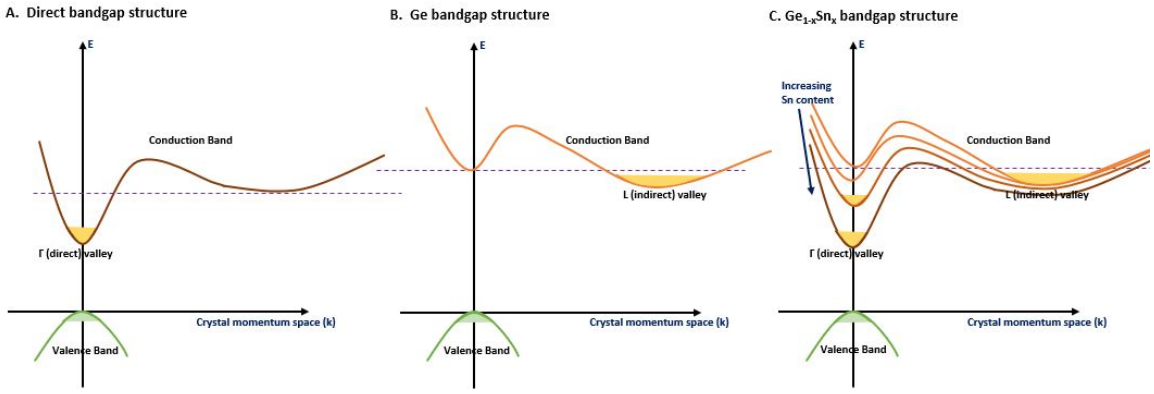

Figure 4. Semiconductor E-k diagrams. Plot "A" represents the band structure of an ideal direct semiconductor. Plot "B" shows the band structure of Ge material which depicts electron population concentrated on the L-point that hinders radiative recombination. Plot "C" is the band gap structure of GeSn alloy; the conduction edge of the valley is strained by Sn content which increases the electron population on the Γ-point. Reproduced with permission from [9].

With Sn concentrations in the range of 7%, the indirect semiconductor Ge transitions to a direct semiconductor. As shown in Figure 4B, radiative recombination is hindered by the momentum mismatch in unstrained Ge. However, when Sn content is added, the band gap of the GeSn alloy shrinks and the population of electrons at the Γ-point (direct valley) increases and results in radiative recombination more readily [9]. Although it is proven that a certain amount of Sn can improve the light emitting property of Ge, it remains unknown how Sn content affects the susceptibility of the EL properties to radiation-induced displacement damage. Hence, the primary objective of this research was to quantify the EL degradation due to defects introduced in group IV devices via proton irradiation.

Both PL and EL studies have been conducted on the GeSn materials produced by Arizona State University (ASU) [10] [3]. Figure 5 shows that the projected indirect-to-direct transition was at the intersection of the extrapolated lines around 6.7% Sn content; the addition of Sn decreases the band gap at the gamma point relative to the L point so the samples with higher Sn are expected to result in higher EL signals, as has been demonstrated [11].

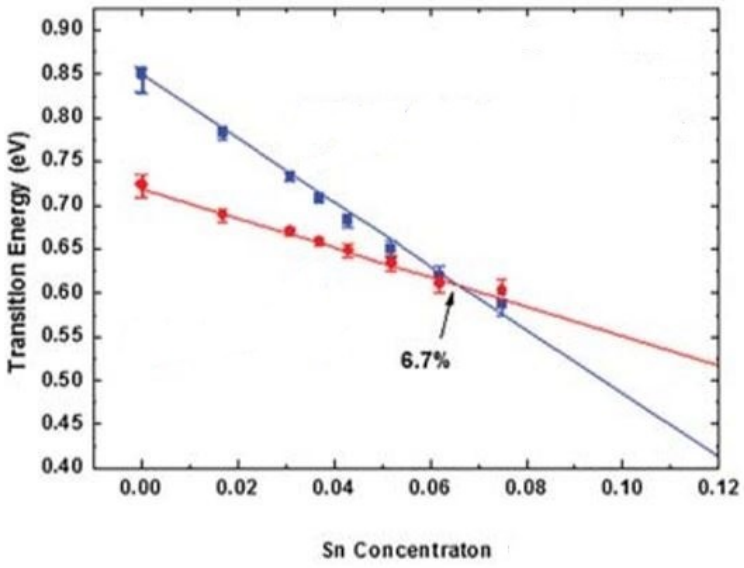

Figure 5. Direct gap emission plot (blue) versus indirect gap emission plot (red) extracted from the PL study of the GeSn device: the projected indirect-to-direct transition was at the intersection of the extrapolated lines around 6.7%. Reproduced with permission from [10].

2.2 Proton Displacement Damage

Most radiation effects in the natural space environment can be attributed to protons since they are plentiful and highly energetic (and therefore not readily shielded) [12]. For this reason, this research exclusively focused on the radiation effects of protons. Incident protons can cause atomic displacement in material upon collision; due to their heavy mass, protons can easily transfer a large fraction of their incident energy in

such collision events. While a larger fraction of proton energy gets transferred to the electron clouds of the target atoms, only a small fraction of energy loss (< 0.1%) causes lattice disorder in the target material. When a target semiconductor nucleus is displaced from its site by an incident proton it becomes a primary knock-on atom (PKA) as illustrated in Figure 6 [12]. The collision cascade continues until the magnitude of energy transferred to PKA is reduced to less than the threshold required for displacement. While most of these vacancy-interstitial pairs recombine in time, some vacancies fail to recombine and leave permanent damage to the target material; the cumulative damage that results is known as proton displacement damage. The rate of vacancy-interstitial pair recombination depends on temperature, bias condition, and material characteristics. Depending on semiconductor type and the operational environment, proton displacement damage results in different effects to a device.

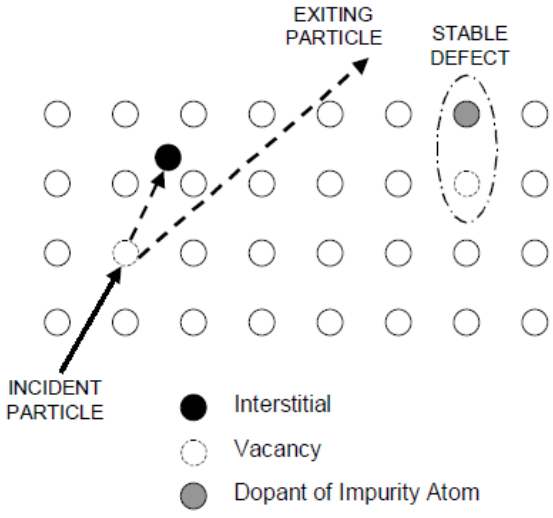

Figure 6. Depiction of proton displacement damage: an incoming proton generates a vacancy-interstitial PKA pair. Reproduced with permission from [12].

Previous studies on proton radiation effects in photonic devices have demonstrated that the majority of hetero-structure LEDs, based on III-V compound semiconductors, were relatively insensitive to proton irradiation, whereas, amphoterically doped devices showed degradation of optical power output upon proton irradiation (Figure 7) for reasons that are not entirely understood [13] [14] [15] [16].

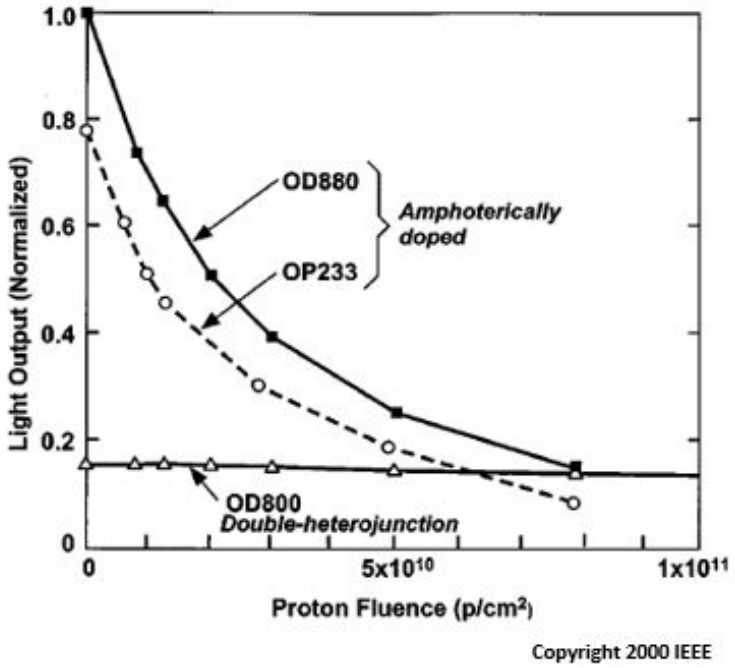

Figure 7. Degradation of optical power output for two amphoterically doped LEDs and the double-heterojunction LEDs. Reproduced with permission from [13].

Since the test samples for this research were hetero-structure devices, pre-rad/post-rad EL results might be expected to show little to no change at the fluence levels shown in Figure 7. All LEDs presented in this figure were made of Gallium-Aluminum-Arsenide (GaAlAs). The two amphoterically doped devices (OD880 and OP233) were significantly degraded at a 50 MeV proton fluence of about 10^{10} cm^{-2}. That is equivalent to a total dose of about 1.4 krad (GaAs). The double-heterojunction LED (OD800) was

far less sensitive to radiation damage, but it also had a considerably lower initial light output compared to the amphoterically doped LEDs [13].

According to Figure 7, a typical LED showed light output degradation to the fullest when the induced 50 MeV proton fluence was around 10^{11} cm^{-2}. Regardless of the trend shown above, the devices in this experiment could be expected to respond to radiation damage differently since they were made of different material. Hence, the fluence levels and particle energies required to create significant displacement damage effects in these devices had to be considered through literature research (pg.13) and simulations.

Displacement damage can alter the electrical properties of a semiconductor in many ways because of the presence of radiation induced defect levels in the band gap of a semiconductor (Figure 8). Known mechanisms resulting from such defect levels include: (1) the trap-assisted generation of EHP, (2) the trap-assisted recombination of EHP, (3) carrier trapping, (4) the compensation of donors or acceptors, and (5) the tunneling of carriers [12]. Of the five possible mechanisms mentioned above, trap-assisted recombination of EHP is expected, for the devices in this study, to be the most important mechanism of degradation in EL intensity. When the energy level associated with a defect is located in the deep-level, close to the mid gap, it can readily exchange momentum with carriers, resulting in non-radiative recombination by release of thermal energy rather than photons. Carrier trapping, in which a carrier is captured at a defect and then released to its original band, is another important mechanism in this study, because it forms the basis of the DLTS technique for characterizing trap levels.

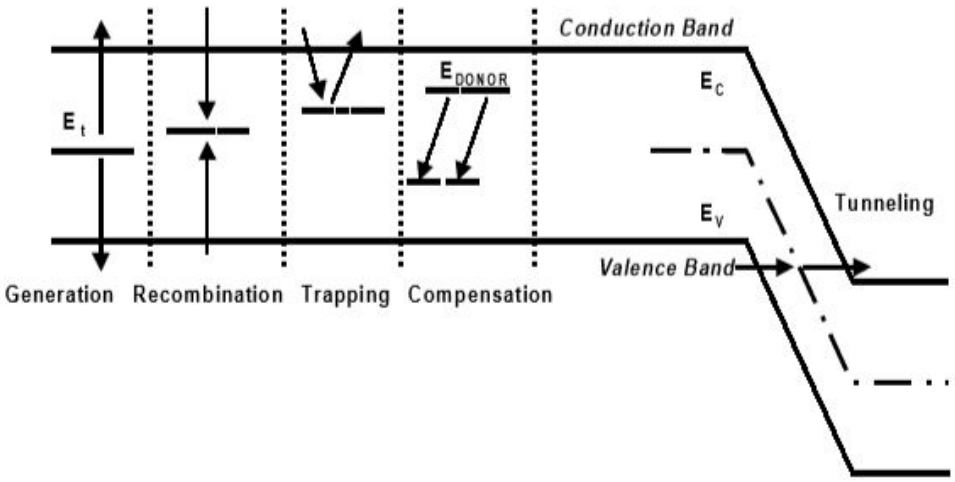

Figure 8. Possible electrical effects which could occur due to displacment damage. Reproduced with permission from [12].

The principal cause of performance degradation in a number of device types is the reduction of the minority carrier lifetime [12] [17]. After irradiation, the minority carrier lifetime is impacted, typically showing noticeable reduction, due to proton induced introduction of defects (i.e. recombination centers). LEDs are relatively radiation hard since their carrier lifetimes in the active device regions are usually short.

In Ge crystals, simple vacancies and interstitials are mobile, even at liquid nitrogen temperatures (~77 K), so it is expected that a large proportion of these simple defects will combine with one another or impurities to form more stable defect complexes during and immediately after irradiation. These processes fall within the category of short-term annealing. Other annealing processes may take place at room temperature over a long term (days to months). In fact, long-term annealing is often observed in devices operating in space [12]. The same long-term annealing processes may take place in minutes to hours when high temperature is applied, although entirely

different annealing processes (i.e. dissociation of defect complexes that were stable at room temperature and reformation into more stable defect complexes that were less abundant at room temperature) may also be observed.

Previous research showed small PL improvements in GeSn alloys followed by large degradation via radiation effects [18]. With a combination of the isochronal/isothermal annealing processes, it was worthwhile to study the annealing effects in these materials, whether or not it was beneficial to the recovery of the LED's electroluminescence property.

2.3 Total Dose and Particle Energy

Non-ionizing energy loss rate (NIEL) must be considered when assessing displacement damage. NIEL is the part of the incident particle energy transferred via Coulomb, nuclear elastic, and nuclear inelastic interactions which produce the initial vacancy-interstitial pairs and phonons. With the same radiation source, energy, and fluence, the magnitude of NIEL can vary depending on the target material. Figure 9 shows the particle energy spectrum and the associated NIEL in Ge semiconductors [19]. According to the figure, the lower energy protons (on the order of 1 MeV on this scale) cause greater displacement damage than higher energy protons. For proton energies below approximately 100 MeV, Coulomb elastic scattering is dominant and produces atomic recoils with energies in the hundreds of eV. At higher energies, nuclear elastic scattering becomes more important, resulting in recoils with smaller energies. Generally, the elastic cross section decreases as the incident proton energy increases, although, it remains larger than the inelastic cross section at all the energies on this scale. In this

experiment, a 2 MeV proton source was used as it could be obtained locally and affordably.

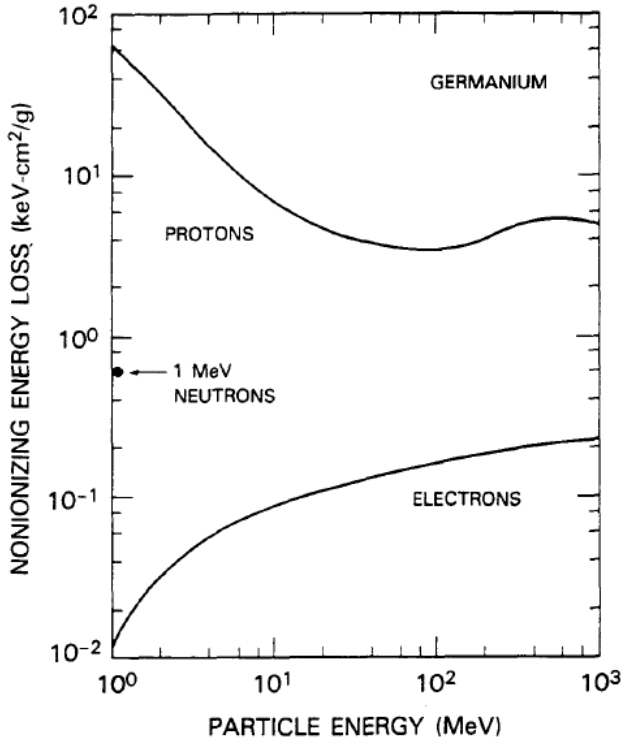

Figure 9. NIEL and particle energy relationship in Ge semiconductors. Reproduced with permission from [19].

Based on previous DLTS experiment results and neutron displacement damage research [18], 2 MeV proton fluence levels on the order of 10^{14} cm^{-2} were deemed necessary for observation of clear EL degradation and characterization of radiation-induced deep-level defects. With this reference level in mind, four fluences (between 2×10^{12} cm^{-2} and 4×10^{14} cm^{-2}) were chosen. The European Space Agency's online suite of tools, Space Environment, Effects, and Education System (SPENVIS) was used to determine the relevance of these fluence levels to equivalent displacement damage doses expected in actual space environments. Figure 10 shows equivalent mono-energetic

proton fluence levels required to create the cumulative unshielded displacement damage expected over 18 years in geosynchronous (36,000 km) orbit. The equivalent 2 MeV proton fluence for this simulated satellite mission lifetime is on the order of 10^{12} cm^{-2}; in other words, the lowest fluence used in this study is roughly equivalent to the highest displacement damage dose one might expect an unshielded satellite component to receive over 18 years in geosynchronous orbit.

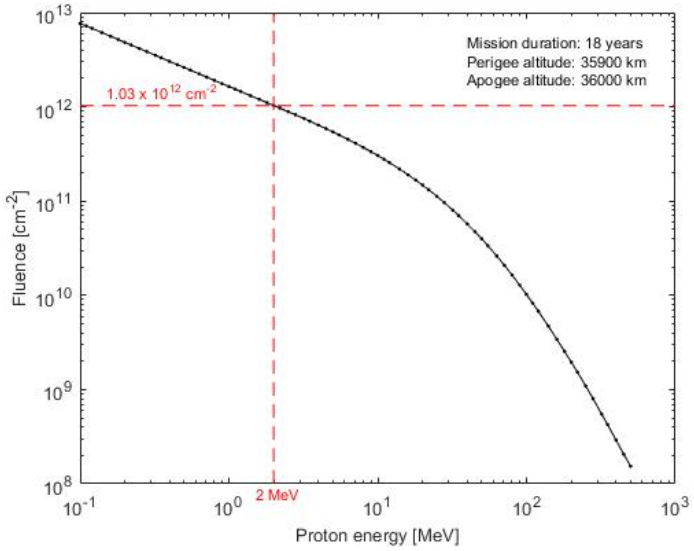

Figure 10. Equivalent monoenergetic proton fluence levels required to create the cumulative unshielded displacement damage expected over 18 years in geosynchronous orbit.

III. Experiment Setup

3.1 Test Sample Description

The GeSn test devices for this experiment were fabricated and provided by ASU [3] [20]. Figure 11 shows a schematic representation of the test devices.

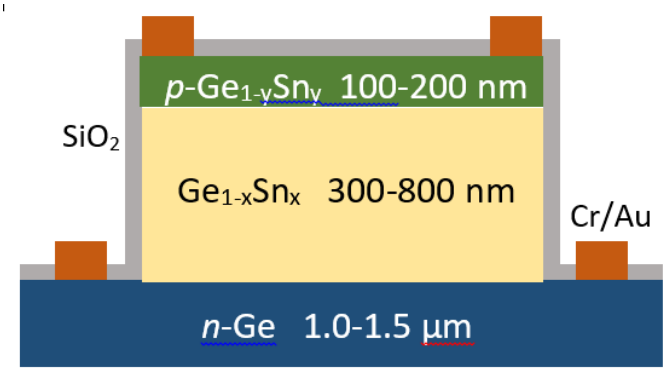

Figure 11. A schematic of the test sample fabricated from ASU: hetero-structure p-i-n geometry (p-$Ge_{1-y}Sn_y$/i-$Ge_{1-x}Sn_x$/n-Ge).

The test devices were fabricated on Si wafers in hetero-structure p-i-n geometry using ultra low-temperature (T<300˚C) depositions of the highly reactive chemical sources Si_4H_{10}, Ge_4H_{10}, Ge_3H_8, and SnD_4. Active device areas were defined in circular mesas 360 µm and 580 µm in diameter and Cr/Au metallization was deposited for ohmic contacts to the p and n regions (Figure 11), which were doped with 2×10^{19} cm^{-3} boron and phosphorous atoms, respectively. The intrinsic regions of these devices were unintentionally doped at levels around 10^{16}-10^{17} cm^{-3}, with the pure Ge sample being n-type and the GeSn samples being p-type. The Sn content in the GeSn intrinsic layer varied from 0% to 9.4%. The properties of the intrinsic regions of these devices are listed in Table 1.

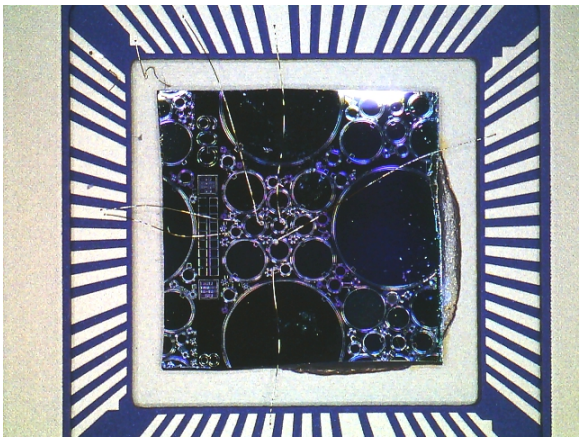

Figure 12. The packaged and wire-bonded sample.

The fully processed wafers received from ASU were diced into ~5 mm × 5 mm samples and packaged at AFIT. The packaging enabled microscopic-sized active regions to gain access to macroscopic electrical pin-connections. An EPO-TEK® H20E compound was applied between the device and the package and heated for 20 min at 100 C until the compound dried. Gold wires (of 25 μm in diameter) were then connected to appropriate regions to drive bias current to active regions (Figure 12); the inner ring of metalization was the applied bias connection and the outer ring of metalization was the ground connection.

3.2 Sample Selection

Sn content in the $Ge_{1-x}Sn_x$ samples varied as follows: x = 0, 0.02, 0.069, and 0.094. With varying Sn concentrations, each sample was presumed to have different device quality and luminescence intensity. For instance, there was expected improvement in luminescence with Sn content, but more defects were also expected as the Sn concentration was increased.

In each device, several different device sizes could be found and emitted different EL intensities; typically, the smaller devices emitted stronger EL. Hence, two different medium-to-small sized device mesas (diameters of 360 μm and 580 μm), were used in this research. Samples were irradiated by the predetermined 2 MeV proton fluence of 2×10^{14} or 4×10^{13} cm^{-2} (Table 2) for the first experiment series. For the second experiment series, the following proton fluences were used: 4×10^{12} cm^{-2}, 4×10^{13} cm^{-2}, and 4×10^{14} cm^{-2} (Table 3).

Table 2. Test devices used during the first experiment series, their Sn content, and proton fluence levels to which they were irradiated.

Sample ID	Sn Content [%]	2 MeV Proton Fluence [cm^{-2}]
Ge472-5	0	4×10^{13}
Ge472-6	0	2×10^{14}
PIN13-3	2	4×10^{13}
PIN12-6	6.9	2×10^{14}
PIN12-7	6.9	4×10^{13}
PIN54Bp-2	9.4	4×10^{13}

Table 3. Test devices used during the second experiment series, their Sn content, and proton fluence levels to which they were irradiated.

Sample ID	Sn Content [%]	2 MeV Proton Fluence [cm^{-2}]
Ge472-7	0	4×10^{14}
Ge472-8	0	4×10^{12}
Ge472-9	0	4×10^{13}
PIN13-8	2	4×10^{14}
PIN13-6	2	4×10^{13}
PIN12-5	6.9	4×10^{14}
PIN12-9	6.9	4×10^{13}
PIN54Bp-3	9.4	4×10^{14}
PIN54Bp-5	9.4	4×10^{13}

3.3 Laboratory Setup

All the necessary equipment was readily available or newly purchased since some parts of this research (e.g. DLTS) were part of an on-going project at AFIT. In the subsections below, plans for each study and equipment setup are explained.

3.3.1 EL Study and Setup

Pre-rad and post-rad EL measurements were taken at room temperature. Two different setup configurations were utilized for EL measurements: one for the actual EL measurement and another setup for optimizing the position of a fiber optics cable, which was located in front of the sample on the X-Y-Z translational mount; this procedure was completed prior to EL measurement for better light detection. Descriptions for each configuration can be found in the subsections below. When the EL equipment is properly set up, the samples' EL intensity (displayed by the lock-in amplifier in millivolts) and injection current (driven by a Source Measure Unit (SMU) in milliamps) relationship can be measured. Most of the equipment parameter values for EL measurements were kept constant (Table 4), except the applied current.

Table 4. Equipment parameter values for EL measurements.

Equipment	Parameters	Parameter Values
InGaAs Detector	Frequency	1 MHz
	Gain	70 dB
SMU	Pulse width	3 ms
	Source Current	Varied by measurement
lock-in Amplifier	Sensitivity	10 mV
	Display Scale	Varied by sample
	Gain	60 dB
	Integration Time	1 sec
	Low-pass filtering	24
Function Generator	Frequency	60 Hz

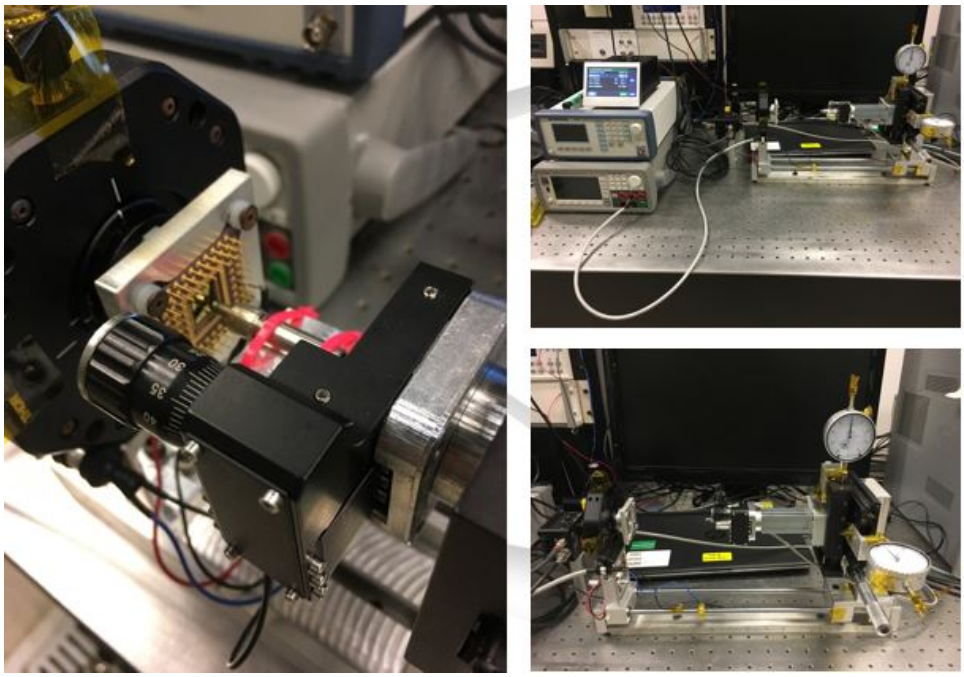

Figure 13. EL measurement equipment. The left picture shows a close-up view of the final EL setup which shows the close proximity of the fiber optic tip to the device being measured; the pictures on the right show the zoomed-out view of the setup. In this final setup, two length indicators were attached to the X-Y-Z translational mount in order to enable return to the same rough position at different phases of the experiment (i.e. pre-rad, post-rad, and annealing steps).

3.3.1.1 Setup for EL measurement

The setup for EL measurement is shown in Figure 14. When the device receives the bias current from a SMU, which pulses at the frequency the function generator produces, the device emits light at that same frequency. One end of the fiber optics cable (low hydroxyl silica fiber bundle) was located within one millimeter of the face of the device to collect EL photons. This one-meter fiber bundle transmitted 400-2400 nm light with negligible attenuation. The EL from these devices was previously observed to fall within the range of 1400-2400 nm, with peak intensities at approximately 1600 nm, 1700, nm, 2100 nm, and 2300 nm for Sn concentrations of 0%, 2%, 6.9%, and 9.4%, respectively [20]. The other end of the fiber optics cable was connected to a

thermoelectrically cooled Indium-Gallium-Arsenide (InGaAs) photodetector. The wavelength range of the detector was 900-2570 nm. The InGaAs photodetector then provided a signal to the lock-in amplifier, which received a reference signal from the function generator and displayed a relative measure of the detected light intensity on a millivolt scale. The lock-in amplifier significantly improved the signal to noise ratio of the detection current [21]. The experiment was not suited to make absolute measurements of EL intensity from the test devices, but rather comparisons of the pre-rad and post-rad EL intensities.

The current and voltage setup for the SMU had to be carefully selected to maximize EL intensity while avoiding significant Joule heating in the devices and contact bond wires. The EL studies conducted on similar devices by ASU [21] suggested that an injection current density of 200 A/cm^2 produced optimal EL intensity. For 580 μm diameter devices, this equated to about 530 mA. This level of current was right at the limit of what the 25 μm gold wires could carry continuously without melting; the metallization on the samples most likely had a similar limit as well. In addition to the need to not overload the wires and metallization, significant localized heating (due to high-power density in the devices) had to be considered.

The duty cycle was defined by the frequency and pulse width of the injection current. The duty cycle was set at 18% (with a frequency of 60 Hz and pulse width of 3 ms) which was low enough to avoid melting the gold wire but high enough to produce a detectable signal in the lock-in amplifier.

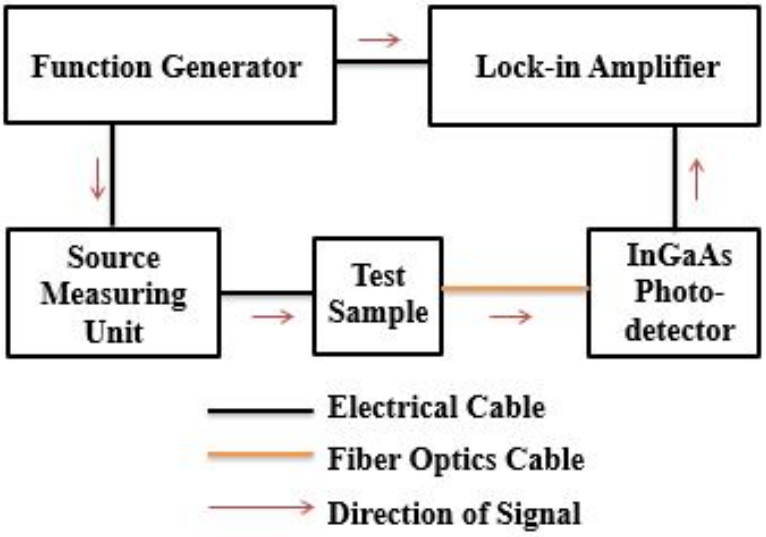

Figure 14. The setup configuration for the EL measurement. While the sample emitted a considerably weak signal which was buried in detector noise, the lock-in amplifier was used to suppress the noise and display a relatively clear detection signal.

For the devices that emitted the lowest EL intensities the amplified signal showed significant noise fluctuations, so, an Arduino was built and connected in between the lock-in amplifier and a laptop computer which stored the collected data. This newly added feature collected 100 lock-in amplifier readings in 30 seconds and averaged them to provide a single point average value with standard deviation.

While most equipment parameters (Table 4) were kept constant, the current source in SMU was a controlled experimental variable. The source current started at 0.1 A and was increased by 0.1 A each step until the reading plateaued; generally, the upper-end current was less than 1.5 A. The SMU compliance level was set at 3 V to enable current to be sourced up to levels around 2 A.

3.3.1.2 Setup to Optimize Sample Position

Prior to measurement, the fiber optics tip had to be positioned to maximize the EL collection from a device. The configuration in Figure 15 was used to find the optimal location for the fiber optics tip, so the InGaAs detector could receive the most photons from the device in light emission mode (Figure 14). The fundamental idea of this configuration was to utilize the photovoltaic effect of the sample. The test device could function as photodiodes when reverse biased, generating an electrical signal (photocurrent) when it was illuminated by a high-powered commercial LED which operated at 60 Hz (the same frequency the SMU used in EL mode) and 200 mA. This photocurrent was displayed as a voltage proportional to the detected LED light intensity in the lock-in amplifier. While the LED shined on the sample, the position of the fiber optic tip could be adjusted via the X-Y-Z translational mount to the exact location where the lock-in amplifier displayed the highest detection reading.

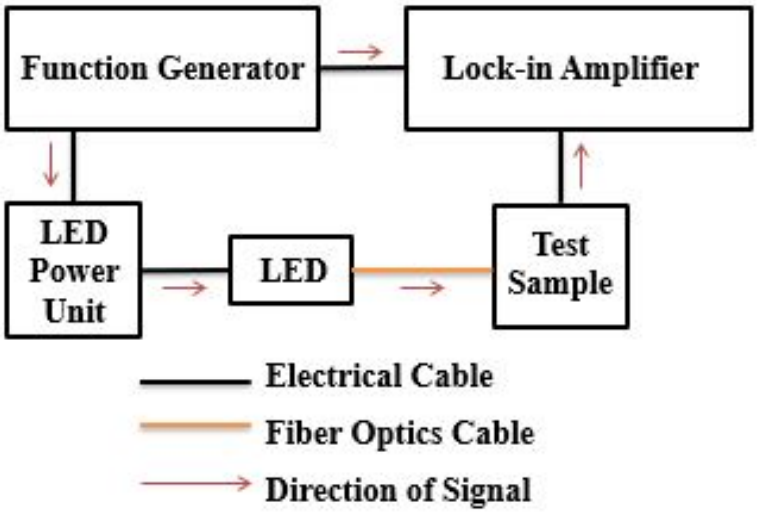

Figure 15. The setup configuration to optimize sample position. In order to find the optimum position of the fiber optics before EL measurements were taken, the previous configuration (Figure 14) was modified so the sample could function as a photodiode, providing a signal to indicate how well the fiber optic was positioned.

3.3.2 DLTS Study and Setup

The DLTS system was a fully automated system of temperature control and electrical measurement. The pressure in the chamber was kept under vacuum (below 1 millitorr) to allow for a range of temperatures without surface effects (i.e. H_2O condensation at low temperatures). The temperature range used for DLTS measurements was typically 24 K to 220 K.

The equipment setup for the DLTS was fairly simple since the system had been fully integrated and was previously used at AFIT. Figure 16 shows the configuration of the DLTS measurement. A typical DLTS measurement for each device took up to two days, accounting for mean time to allow the entire chamber to return to room temperature.

Typically, lower Sn samples (e.g. 0 % and 2 %) were more favorable for DLTS analysis because the concentration of defects (e.g. impurities) in the higher Sn samples were already high (prior to irradiation), so observing the clear peaks in their rate-window spectra was challenging. Regardless, a few good representative rate-window spectra taken from higher Sn samples were used to complete the data comparison to the lower Sn samples. Like the EL measurement procedure, the DLTS measurements were taken once for pre-rad at room temperature and a few times for post-rad at various annealing temperature steps.

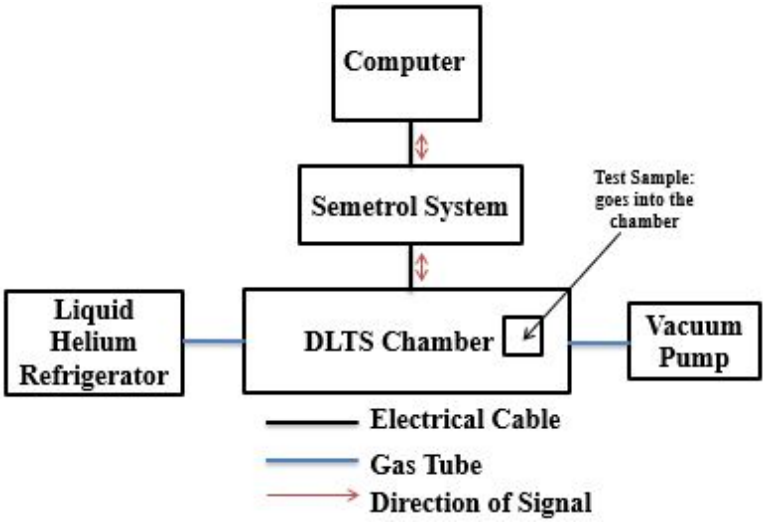

Figure 16. The configuration of the DLTS measurement. The chamber was connected to both a liquid helium refregerator and a vacuum pump which controlled temperature and pressure. The Semetrol system received commands from the computer to control temperature in the chamber and collect data.

In the active layer (i-region) of the n-type Ge sample electrons are the majority carriers and holes are the minority carriers, whereas, the opposite is true in an active layer of the p-type GeSn alloys. Depending on the carrier of interest in the analysis, minority carrier spectrum could be obtained by the current injection DLTS technique; while, majority carrier spectrum could be obtained by the conventional DLTS technique. When peaks or valleys could be clearly distinguished in the rate-window spectra, Arrhenius fitting of the corresponding peak temperatures at different rate windows was used to find the activation energy associated with the traps.

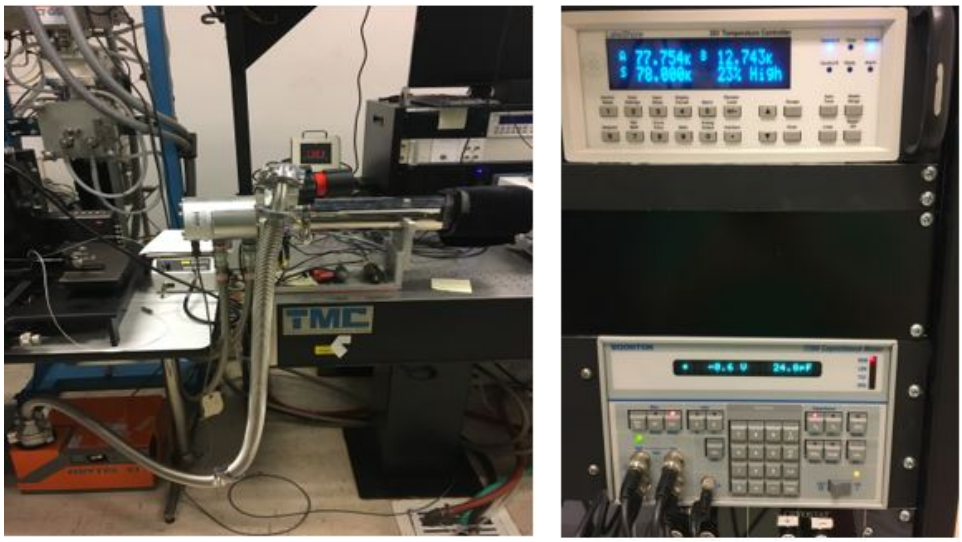

Figure 17. The Semetrol system used for DLTS, C-V, and I-V measurements. The chamber shown in the left picture was connected to a liquid helium refrigerator and a vacuum which controlled the experimental environment for a sample during measurement. The right picture shows the chamber-temperature control unit and the capacitance meter which worked in conjunction with software installed in the desktop computer.

3.4 Overall Research Procedures

Figure 18 shows all of the experimental procedures planned in chronological order. A set of measurements (EL/I-V/C-V/DLTS) were taken once for the pre-rad phase and three times (counting the annealing procedures) for the post-rad phase. For the annealing process, after the first series of post-rad measurements were taken at room temperature, devices were respectively subjected to a series of measurements after being heated to 393 K and 473 K. During each annealing process, the devices were put in the oven/nitrogen furnace and heated for 30 min. Initially, the first batch was annealed in a large, open-spaced (not vacuumed) oven which later became a concern for non-uniform heat treatment. Therefore, all later annealing procedures were performed in a nitrogen furnace; this maintained low-risk heat treatment.

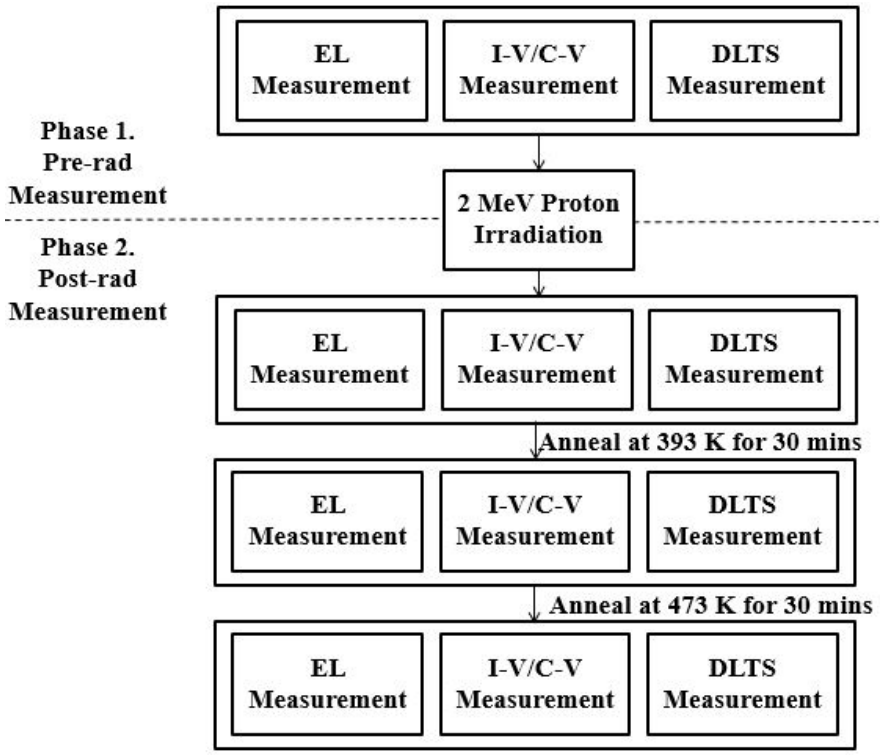

Figure 18. Overall project progression steps. There were four major measurements (EL/I-V/C-V/DLTS) that were collected during the two phases.

A single DLTS measurement took up to 8 hours. In order to open the chamber to swap out samples, the chamber temperature had to be raised from 24 K to room temperature after the helium refrigerator was turned off; this process took about 12 hours. Each I-V and C-V measurement took less than a minute, but also required a 12-hour waiting period between samples for temperature dependent measurements. Each EL measurement took up to 2 hours; EL measurements were not temperature dependent. Therefore, 46 devices were used in EL measurement while 10 devices were used in the temperature dependent measurements.

3.4.1 Proton Irradiation Procedures

The samples were irradiated by a 2 MeV proton beam at Edwards Accelerator Laboratory, Ohio University (OU). Fluences up to 4×10^{14} cm^{-2} were applied over a period of 5-50 min. For the first radiation experiment series, the GeSn samples were irradiated by a 2 MeV proton beam with a proton fluence of 4×10^{13} and 2×10^{14} cm^{-2} at room temperature; the predetermined fluence level varied by sample (Table 2). For the second experiment series, the following proton fluences were used: 4×10^{12} cm^{-2}, 4×10^{13} cm^{-2}, and 4×10^{14} cm^{-2} (Table 3).

As shown in Figure 19, the sample was attached to a thin stainless-steel target holder by double-sided carbon tape (carbon for electrical conductivity). Behind the target holder, a 39.9 cm^3 block of copper functioned as a heat sink to prevent sample temperature from rising more than a couple degrees above room temperature.

Figure 19. Edwards Acclerator beam line (left) used as the radiation source in this research. Its vacuum chamber (right) had a sample holder hanging on its lid; the sample was attached to a block of copper and its pin area (everywhere on the packaged sample but the actual sample area) was covered with conductive foam to prevent electrostatic charge buildup.

As mentioned in the previous sections, early time recombination of vacancy-interstitial pairs and the formation of more stable defect complexes were expected in freshly irradiated samples, but some longer term room temperature-induced annealing processes were also known to be possible, and these had to be minimized until post-rad measurements (especially DLTS) could be taken. Therefore, after the samples were irradiated, they were stored in a nitrogen dewar at 77 K until they were transported back to AFIT and used for post-rad analysis.

3.5 Two Different Experiment Series

Two different experiment series were conducted throughout this research. Each experiment series used a different number of samples and a different level of irradiating proton fluence; the overall experiment procedures were identical as explained in the sections above. The samples in the first experiment series consisted of two 0% Sn samples (i.e. pure Ge), one 2% Sn sample, two 6.9% Sn samples, and one 9.4% Sn sample were prepared and taken to OU for proton irradiation on 30 August 2018. Two different predetermined proton fluences were applied to samples as shown in Table 2: 4×10^{13} cm^{-2}, and 2×10^{14} cm^{-2}. This preliminary investigation revealed differences and patterns in EL/I-V/C-V/DLTS results throughout the four research phases (pre-rad, post-rad, 393 K annealing, and 473 K annealing).

The number of devices prepared for the second experiment series was about three times the number of devices investigated in the first experiment series. Two samples were prepared per Sn group; on average, four devices (two two-different sized device mesas each) were prepared per sample. With a greater number of prepared samples, an

individual sample in each Sn group was irradiated at one of the three following predetermined proton fluences (Table 3): 4×10^{12} cm^{-2}, 4×10^{13} cm^{-2}, and 4×10^{14} cm^{-2}. This second batch of samples was irradiated at OU on 9 November 2018.

Higher fluence resulted in more clear peaks in the DLTS rate-window, thus fluence levels twice as large as the preliminary experiment were used in the second experiment series. With the previous DLTS results, typically, the hole traps became dominant in the 0% and 2% Sn samples at 2×10^{14} cm^{-2}. Since 6.9% and 9.4% Sn samples had ten times greater majority carrier concentration (2×10^{17} cm^{-3}) than the 0% and 2% Sn samples, ideal irradiating fluence also had to be about ten times greater than 2×10^{14} cm^{-2} in order to observe clearly dominant hole traps in high Sn samples. However, achieving a fluence of 2×10^{15} cm^{-2} was not achievable due to limited time availability at OU. Hence, a fluence level that was twice the amount of the one used in the first experiment series was selected.

An additional fluence of 4×10^{12} cm^{-2} was applied to a few samples to demonstrate the hardness of the samples against lower doses. While using the low fluence level, the samples which were irradiated were not ideal for DLTS analysis for the same reason stated in the previous paragraph. However, it was useful to confirm the degree of radiation-induced EL degradation in this fluence range. As mentioned in the Theory section (Figure 9), the fluence on the order of 10^{12} cm^{-2} is considered representative of long-lasting satellite missions in unshielded geosynchronous orbits.

IV. Results and Analysis

4.1 Chapter Overview

In this chapter, the collected data are consolidated, analyzed, and discussed. The more detailed data collected from individual devices are shown in the Auxiliary plots of Appendix C for reference.

4.2 EL Analysis

4.2.1 Initial Quality Analysis

Prior to irradiating the samples, the EL intensity was measured and listed from smallest to largest to represent the initial sample quality and validate the EL intensity dependence on Sn content (Figure 20). Previous PL research results showed a direct-to-indirect band gap transition at 6.7% Sn content in samples [10] and the highest EL intensities were achieved for Sn content above this crossover point [3]. Considering these results, the samples with higher Sn content were expected to show the strongest EL intensity. This expectation was upheld upon quantitative analysis, but as shown in the figure below, the selected devices reflected a considerable range of pre-rad EL intensities without an obvious dependency on Sn content.

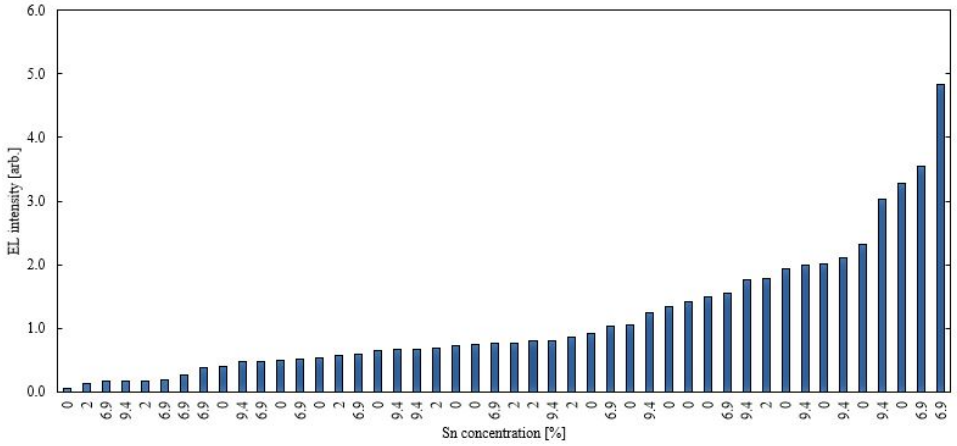

Figure 20. All device pre-rad EL intensities listed from smallest to largest (left to right) in order to show the luminescence quality of the as-grown samples.

Various physical differences (e.g. non-uniform film thickness, non-uniform concentration of unintended-dopants such as boron and phosphorous atoms) could have caused variations in the EL intensities among the different devices. The objective in this study was to quantify the changes in EL intensity that were exclusively affected by the proton fluences and Sn content. Therefore, (1) was used to calculate the magnitude of EL change (ΔEL) in percentage which accounted for the sizes of the quantities (i.e. pre-rad EL and post-rad EL) with arbitrary units:

$$\Delta\text{EL} = \frac{(Pre - rad\ EL) - (Post - rad\ EL)}{(Pre - rad\ EL)} * 100 \qquad (1)$$

The auxiliary ΔEL results for each sample during the four experiment phases (i.e. pre-rad, post-rad, 393 K anneal, 473 K anneal) can be found in Appendix C.2 Figure 62 through Figure 66. While the pre-rad device quality could be inferred by either pre-rad leakage current density or pre-rad EL intensity, neither showed a clear correlation with

ΔEL (Figure 21 and Figure 22), which implied that ΔEL must be dependent on other factors such as Sn content or irradiation fluence.

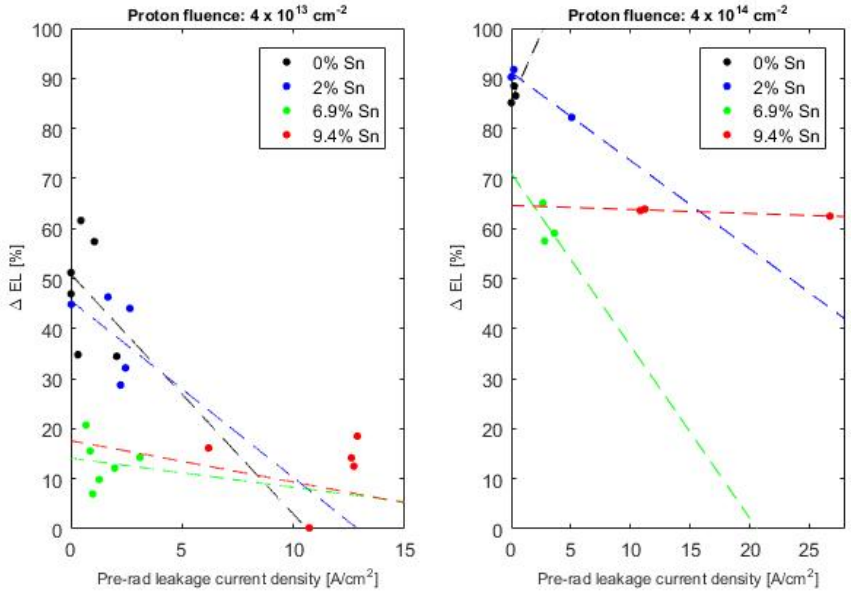

Figure 21. Linear regression lines showing that no clear trend was observed in the relationship between the ΔEL and the pre-rad leakage current density.

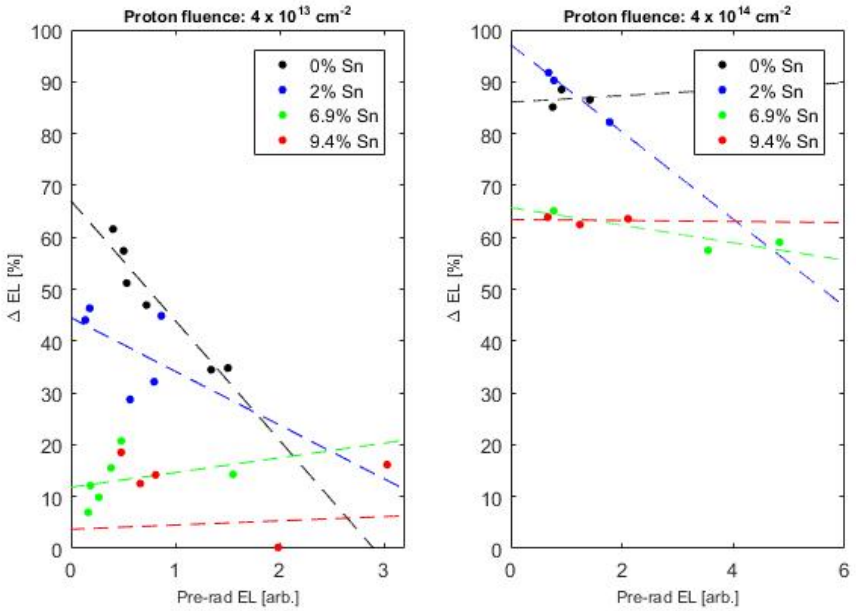

Figure 22. Linear regression lines showing that no clear trend was observed in the relationship between the ΔEL and the pre-rad EL intensity.

4.2.2 Pre-rad and Post-rad ΔEL Analysis

When the relationship between ΔEL and Sn content was considered (Figure 23), the higher Sn samples showed less susceptibility to radiation-induced EL intensity degradation. The $Ge_{1-x}Sn_x$ devices with higher Sn concentration were up to 10 times more resistant to proton displacement damage than the pure Ge (x = 0) devices. Following exposure to a proton fluence of 4×10^{13} cm^{-2}, the average degradation percentage of the x = 0 and x = 0.094 devices were 47.7% ± 5.8% and 4.7% ± 5.1%, respectively. Figure 24 and Figure 25 show the magnitude of EL degradations.

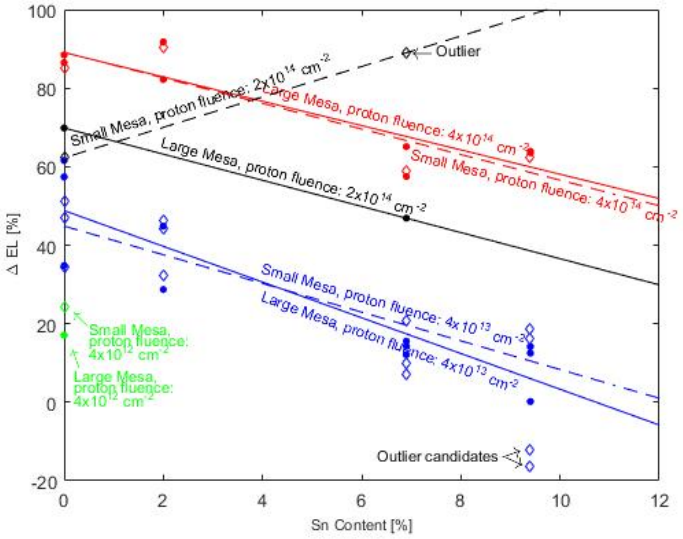

Figure 23. Plot showing how ΔEL related to Sn content at various fluence levels.

The plot shown in Figure 23 was created as a "precursor" to the plots shown in Figure 24 and Figure 25 and shows how the ΔEL related to their Sn content at various fluence levels. Small-size device mesas are indicated by diamonds, and larger-size mesas are indicated by standard dots. The solid lines and the dashed lines are the linear fit of large mesa data and small mesa data respectively.

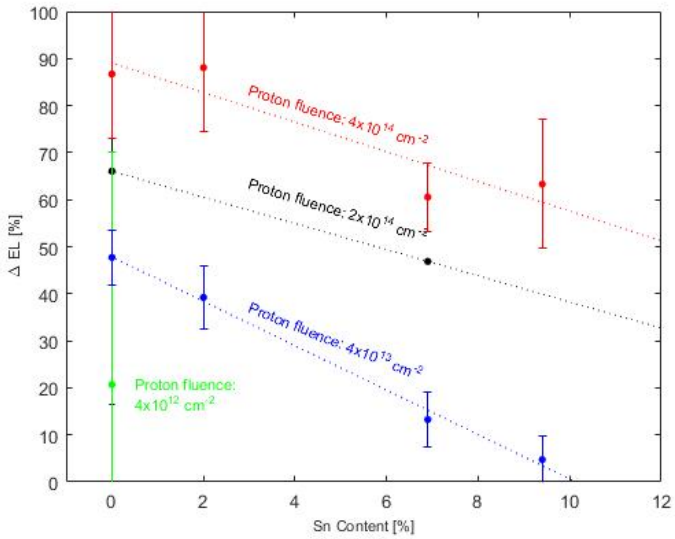

Figure 24. ΔEL dependence on Sn content and irradiating proton fluence.

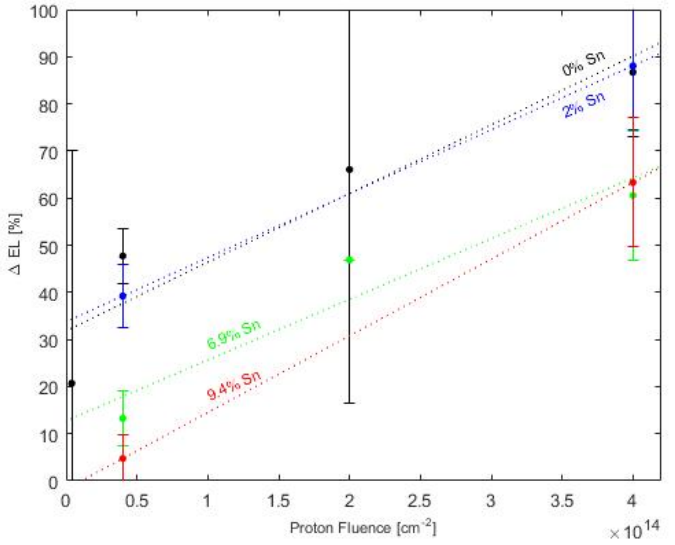

Figure 25. ΔEL versus fluence plot showing another perspective of EL dependency on both Sn content and proton fluence level.

During the EL measurements, z-axis spacing between the tip of the EL fiber optics and the sample was not precisely reproducible between the pre-rad and post-rad measurements, and this was suspected to be a significant cause of variability in EL readings. In the beginning of this experiment, quantifying this variability was prioritized

since it could compromise the EL results if the magnitude of difference in readings were large. Therefore, EL measurements on a device were taken at least twice to calculate the percent difference with (2):

$$Percent\ difference = \frac{|EL_{min} - EL_{max}|}{(\frac{EL_{min} + EL_{max}}{2})} * 100 \quad (2)$$

EL_{min} and EL_{max} are the lowest and the highest EL readings taken on a device, respectively. A variability of up to 30% in a series of EL measurements on the same device was evident; however, these worst-case readings were infrequent. In general, if the EL readings were high and stable, the signals' variability was below approximately 8% (7.8% on average; 5.4% median). The averaged values encountered the worst EL readings, thus the highest EL readings were chosen for final analysis instead.

In Figure 23, a total of three data points were initially considered outliers. Two of the three data points indicated 16.4% and 12.05% ΔEL improvement (Figure 26) following irradiation; considering inconsistent z-axis spacing due to human error caused approximately a 5% percent difference for these two data points, these two significant ΔEL values could not simply be omitted. Potential reasons for these EL improvement observations could only be speculated with the given data, but there was no plausible explanation for a true radiation-induced increase in the luminescence from these two devices. Thus, these points were likely outliers due to measurement uncertainty and other generally unknown errors. Including these two points in the 10^{13} cm^{-2}/9.4% Sn group, the result sample mean and the 95% confidence interval (CI) did not greatly change the overall linear-regression line (Figure 24). Therefore, these data were additional indications of the variability and confirmation that the degradation was

insignificant in 4×10^{13} cm^{-2}/9.4% Sn samples, and they were not removed from the final EL plots as shown in Figure 24 and Figure 25. The 95% CIs shown in Figure 24 and Figure 25 were calculated using the following equation [22]:

$$95\%\ CI = \pm t^*_{n-1} * (\frac{MSD}{\sqrt{n}}) \quad (3)$$

where n is the sample size, t^*_{n-1} is the 95% critical value for the t distribution with $n-1$ degrees of freedom, and MSD is the mean of standard deviation calculated from each sample group.

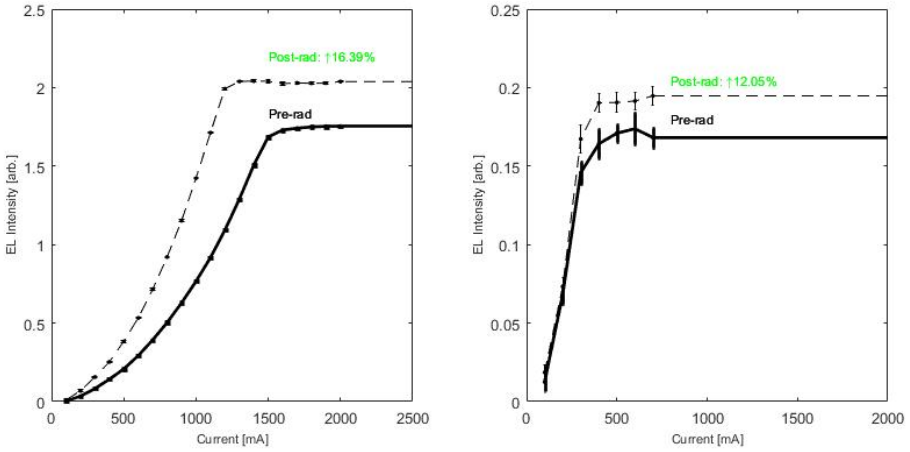

Figure 26. 9.4% Sn devices on the same sample which showed "improved" EL intensity after being irradiated by 4×10^{13} cm^{-2}.

Another outlier candidate (Figure 23) was a 6.9% Sn sample irradiated at 2×10^{14} cm^{-2}. Unlike the other two data points mentioned in the previous paragraph, this datum was removed in the successor plots since its corresponding I-V plot indicated a closed-circuit breakdown behavior after irradiation (Figure 27). This behavior occurred in a few fragile samples which were damaged by a relatively high applied current (greater than 1 A); whereas, other samples could withstand an applied current above 1.5 A with a 15%

duty cycle. Thus, these particular EL data were not considered trustworthy. Further discussion considering the sample damage due to applied current can be found in the "4.3 I-V Analysis" section.

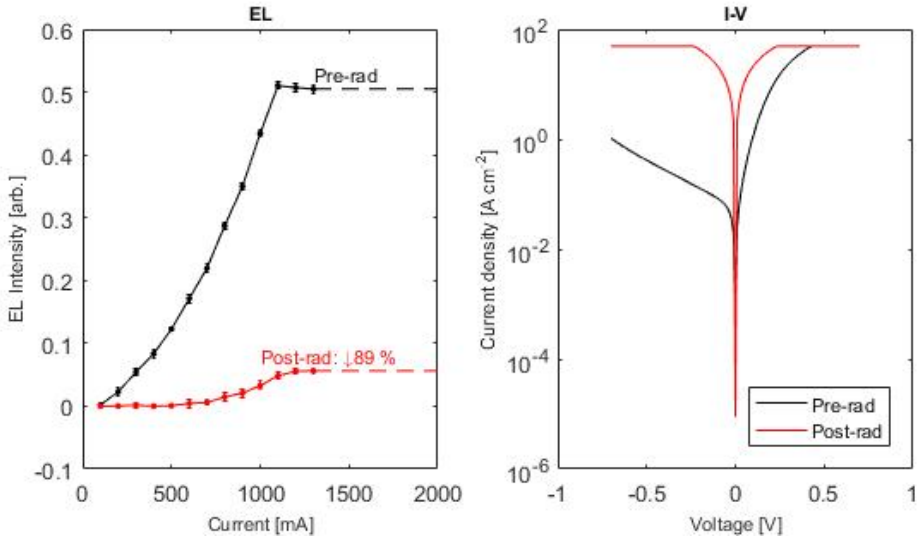

Figure 27. 6.9% Sn devices showing significant EL degradation after being irradiated by 2 × 10^{14} cm^{-2}. This ΔEL data point was removed from the final EL analysis because its corresponding I-V plot showed a closed-circuit breakdown behavior.

4.2.2.1 Positive Effects of Sn in ΔEL Analysis

If the quality of the higher Sn samples was systematically less than that of =the lower Sn samples, one might expect that introducing additional defects with radiation would not cause much degradation on that basis alone. In order to clarify that Sn concentration had a positive effect on radiation response, it needed to be proven that higher Sn samples' pre-rad EL was not systematically weaker than the lower Sn samples. In Figure 28, each data point is the sample mean, and the associated error bars are their $\pm 1\sigma$ values that indicate the range of variables in the sample population. These plots show that higher Sn samples were generally better at emitting light as the lower Sn

samples prior to irradiation and that higher Sn samples' EL degraded relatively less compared to the lower Sn samples. Therefore, the theory of Sn's positive contribution to the radiation response was valid.

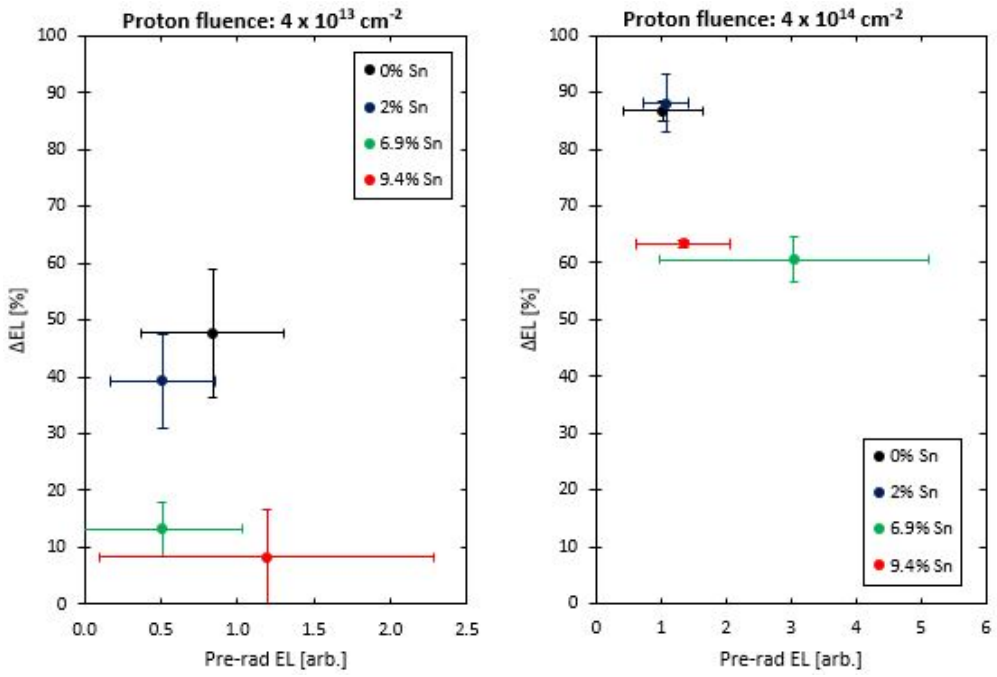

Figure 28. ΔEL versus pre-rad EL plots showing that higher Sn samples had relatively stronger EL intensity prior to irradiation, and their EL degraded less than the ΔEL of the lower Sn samples following irradiation.

4.2.3 393 K and 473 K Annealing ΔEL Analysis

Extrapolating from the previous PL research result [18], in which 333 K annealing accelerated recovery from radiation-induced EL degradation, the intensity of EL was expected to improve when higher annealing temperatures (up to 473 K) were applied. In Figure 29 and Figure 30, the data in the 474 K anneal plot represent the change in EL intensity relative to the data in the 393 K anneal plot, not relative to the pre-rad data.

Each data point is the statistical sample mean of data which are in the same Sn content group. The 95% CIs were calculated using (3). In Figure 30, the data points in 4×10^{12} cm^{-2} group did not have 95% CIs because they could not be computed with a sample population of n = 1 (i.e. the *t* distribution with 0 degrees of freedom does not exist). Unlike the ΔEL used in the previous section, ΔEL data were not absolute values since the change of EL could indicate either EL improvement or degradation; EL improvement was expected via annealing affects.

The first two annealing plots in Figure 29 represent the data collected during the first experiment series while the other two annealing plots in Figure 30 represent the data collected during the second experiment series. These summarized annealing plots showed different outcomes for the annealing effects: (1) the first figure shows a majority of samples' EL intensity degraded following 393 K anneal while their EL improved following 473 K anneal; and (2) the second figure shows most samples' EL intensity gradually improved following each anneal at 393 K and 473 K. When the 95% CIs were employed in the result plots, the sample means and 95% CIs of both plots in the second figure clearly resided within the ranges of 95% CIs of both plots in the first figure.

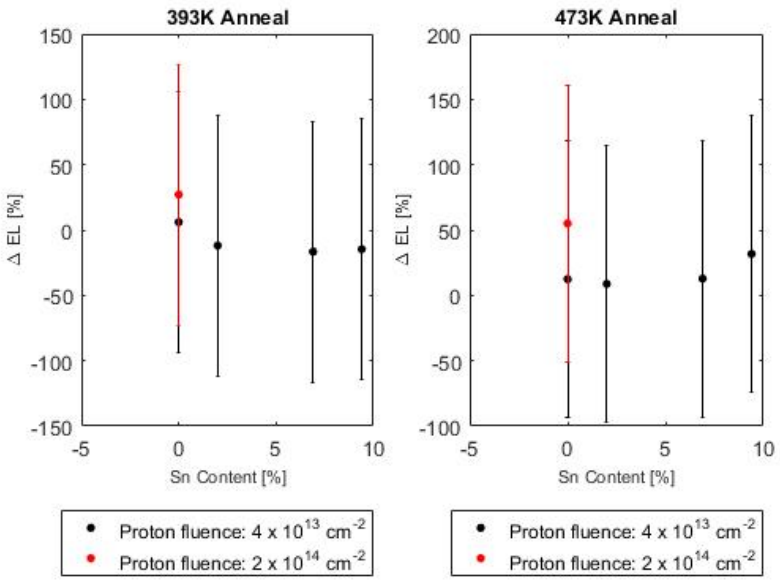

Figure 29. ΔEL values in the 393 K anneal (left) plot showing the EL changes from the post-rad data; the ΔEL values in the 473 K anneal (right) plot show the EL changes from the 393 K anneal data.

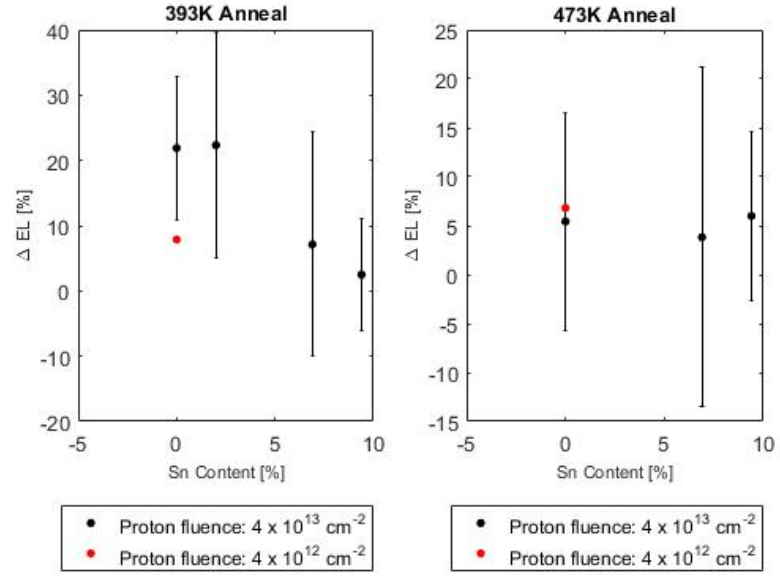

Figure 30. ΔEL values in the 393 K anneal (left) plot showing the EL changes from the post-rad data; the ΔEL values in the 473 K anneal (right) plot show the EL changes from the 393 K anneal data.

For all data in the 4×10^{13} cm^{-2} fluence group in both figures above, the 95% CIs in Figure 30 were far greater than the 95% CIs in Figure 29. However, the 95% CIs could be narrowed with a higher sample size according to (3). All data in the figures above were aggregated along with their Sn groups or fluence groups (Figure 31 and Figure 32), which reflect the relationship between the annealing temperatures and ΔEL. In Figure 32, the data points in the 4×10^{12} cm^{-2} fluence group in both plots do not have error bars because each of their sample population is n = 1 which made the 95% CI calculation intangible. Namely, the first figure shows the effects of the Sn content while the second figure shows the effects of the fluence level. In Figure 31, the low Sn samples resulted in the largest EL degradation as discovered in the previous sections. In addition to that observation, both of the high Sn samples (6.9% Sn and 9.4% Sn) showed EL degradation following 393 K anneal while the low Sn samples (0% Sn and 2% Sn) showed the recovery of EL when annealed with the same temperature. At 473 K anneal, all samples showed EL recovery; especially, the 9.4% Sn samples that recovered the EL intensity of their pre-rad state, $\Delta EL > 0$ (Figure 33). Without further investigation and application of new measurements, these EL improvement observations could not be explained, however the large overlap between the 95% CIs suggests that any apparent trends, or lack thereof, in the mean values cannot be given much credibility.

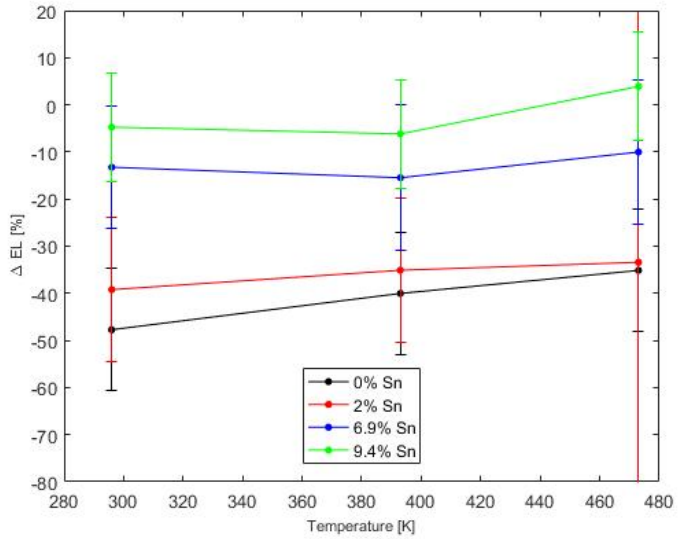

Figure 31. ΔEL values resulting from the comparison between the post-rad/anneal data and the pre-rad data. All data points in the figure above represent the various Sn samples which were irradiated at 4×10^{13} cm^{-2}.

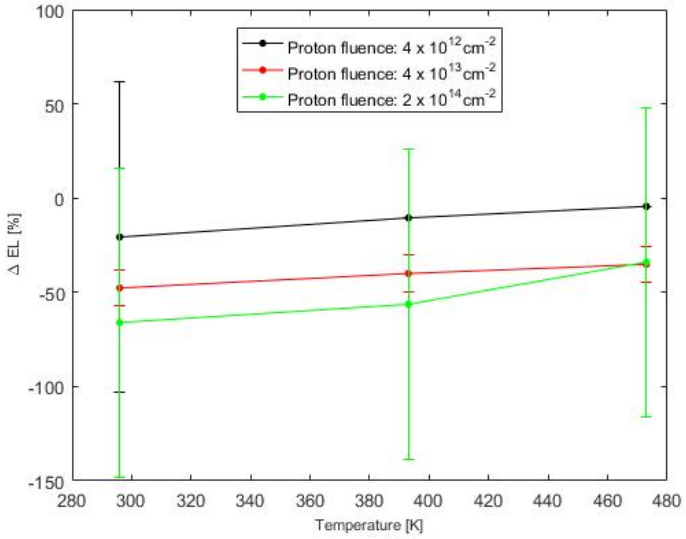

Figure 32. ΔEL values resulting from the comparison between the post-rad/anneal data and the pre-rad data. All data points in the figure above represent the 0% Sn samples that were irradiated by the various fluences.

The data in Figure 32 showed that the 0% Sn samples recover their EL following 393 K anneal. As expected, higher irradiation fluence resulted in higher EL degradation. The

samples that were degraded the most in the 2×10^{14} cm^{-2} fluence group also showed the largest recovery after a 473 K anneal; the variance for this datum is large, however. Nevertheless, the other two fluence groups showed a very similar and consistent EL recovery trend following 393 K anneal for low Sn samples.

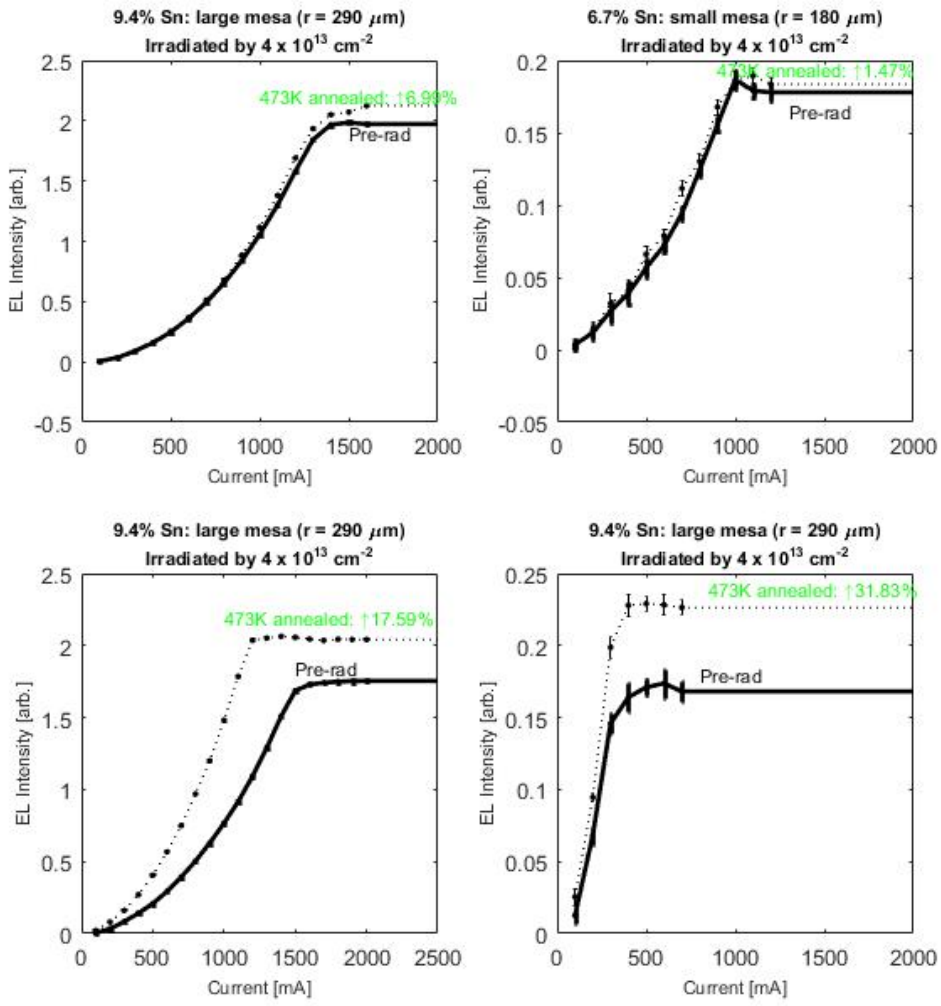

Figure 33. The four exceptional cases where 473 K annealed EL intensity exceeded pre-rad EL intensity. The first plot represents a sample from the first experiment series and the other plots represent samples from the second experiment series; the third and the fourth plots are the devices from the same sample.

4.3 I-V Analysis

4.3.1 Initial Quality Analysis

Prior to irradiation, I-V data were collected at room temperature to determine the initial quality of samples. Samples in the same Sn content group showed slightly different I-V profiles; this observation was anticipated since the samples were considered prototype-grade and manufactured for research purposes. In a typical p-i-n diode, the depletion region extends only partially into the intrinsic region and becomes wider when reverse bias is applied. The current that flows through the depletion region is called leakage current or dark current. As shown in Figure 34 and Figure 35, there is more leakage current at reverse bias and less ideality of the exponential increase in forward bias observed in the samples that contained higher Sn. Both the forward and reverse bias currents represent a less ideal diode property (i.e. less like the ideal diode equation) with greater Sn concentration.

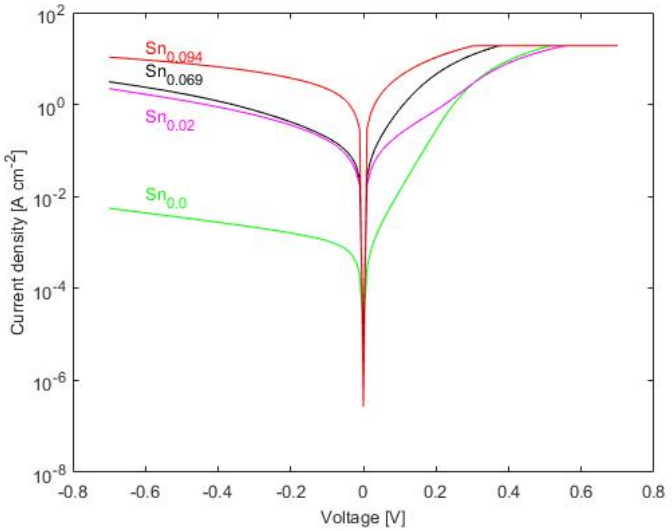

Figure 34. Room temperature pre-rad I-V data collected for large device mesas which had a radius of 290 µm. The current data were normalized by the size of mesa in order to derive current density for analysis.

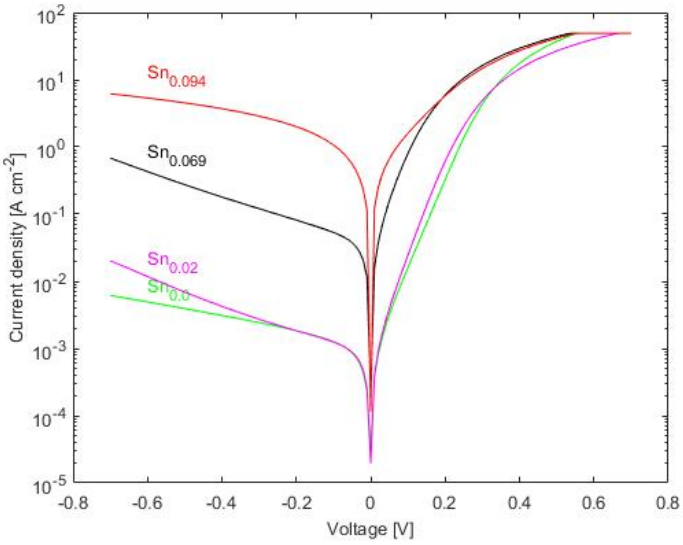

Figure 35. Room temperature pre-rad I-V data collected for small device mesas which had a radius of 180 µm. The current data were normalized by the size of mesa in order to derive current density for analysis.

The quality of the as-grown samples was investigated with the leakage current density of pre-rad I-V data measured at -0.7 V (Figure 36). The overall trend represented a relatively clear correlation between the leakage current density and the Sn content, except the 2% Sn sample's leakage current data were scattered throughout the plots. As mentioned in the paragraph above, higher Sn samples generally showed a higher leakage current density.

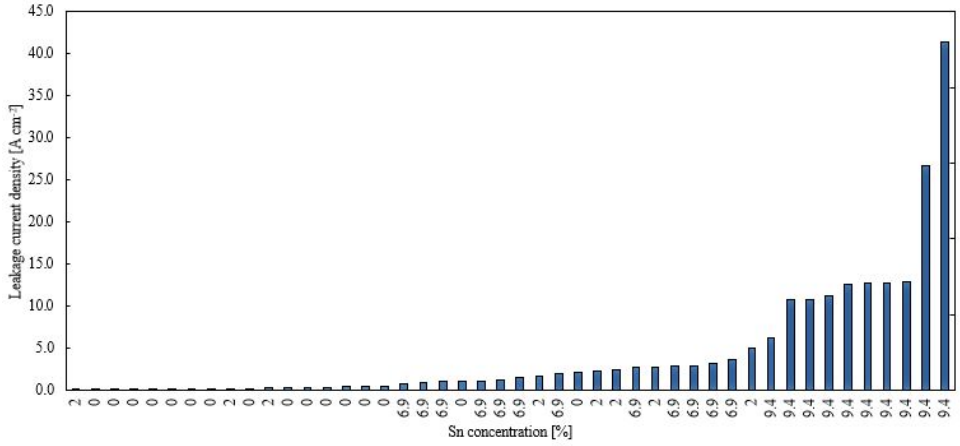

Figure 36. Leakage current densities of all devices at -0.7 V listed from smallest to largest (left to right).

Absent other considerations (such as the dominant physical mechanism suggested by the DLTS results), one might speculate that ΔEL could be directly affected by initial quality of devices, and only indirectly related to Sn concentration. When the pre-rad leakage current density data and the ΔEL data were compared (Figure 37), the Sn samples generally had more leakage current density before irradiation but their EL degraded less after irradiation, compared to the lower Sn samples. In general, high Sn samples have high initial defect densities/leakage currents, but their band structure causes them to have more direct transitions that bypass non-radiative recombination paths. Thus, while there were benefits in radiation hardness, the higher Sn concentration in the GeSn alloy correlated with increased radiation-induced leakage current.

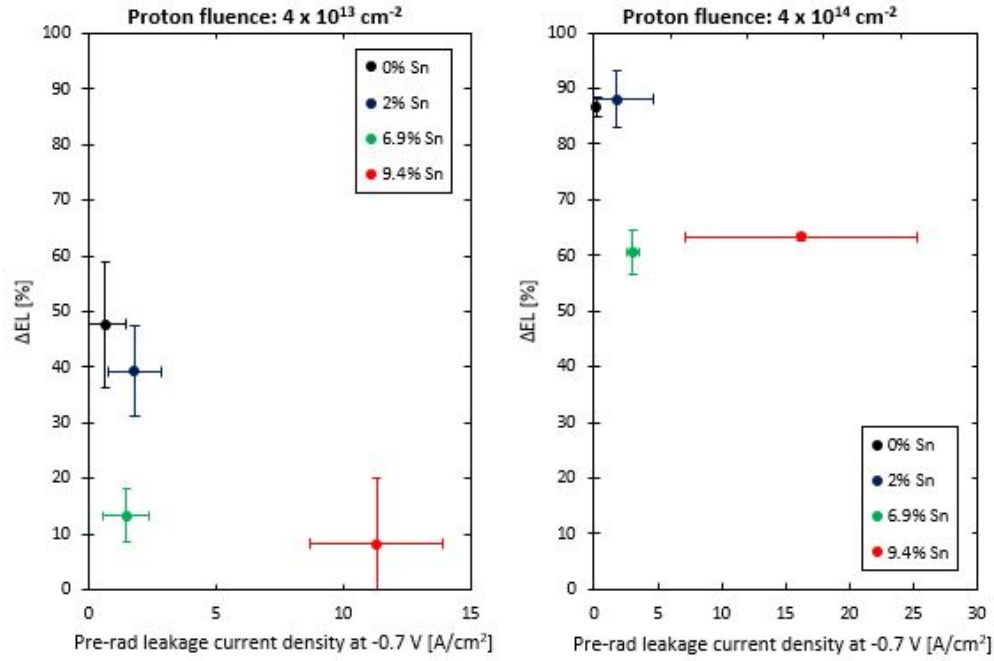

Figure 37. ΔEL versus pre-rad leakage current density plots showing that higher Sn samples generally had a larger leakage current density prior to irradiation, and their EL degraded relatively lower than the ΔEL of the lower Sn samples following irradiation.

4.3.2 I-V Analysis of Irradiated Samples

In theory, comparing the pre-rad and post-rad I-V plots could provide corresponding evidence of radiation-induced degradation to support the ΔEL results; the amount of leakage current density was expected to increase after irradiation in some correspondence to degradation in the EL as shown in Figure 38. In this specific case the magnitude of EL degraded from the pre-rad to the post-rad plots, and the leakage current density on the reverse bias side of the corresponding I-V plots, increased as expected. Likewise, as the EL intensity gradually improved in the two annealing processes at 393 K and 473 K, the leakage current density reduced in each annealing step.

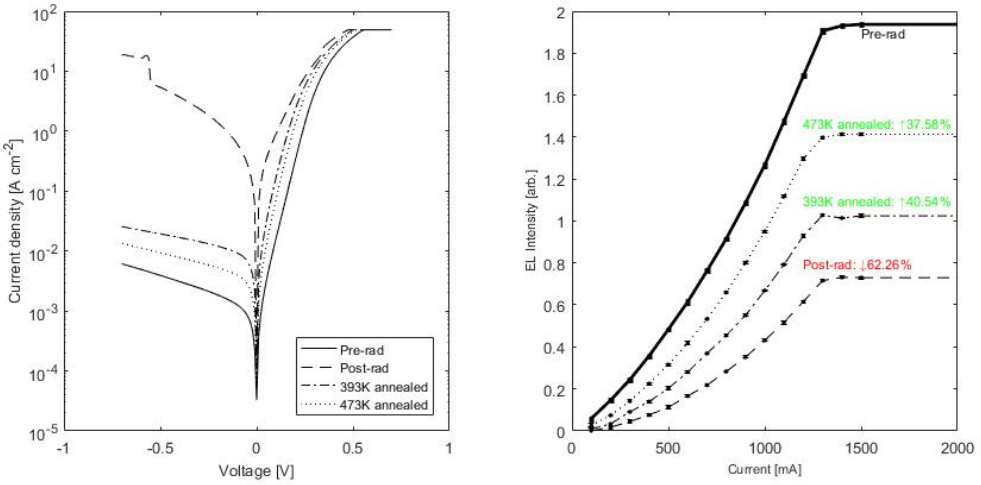

Figure 38. One of a few I-V curves (left) and its corresponding EL plots (right) showing clear correlation. Both I-V data and EL data of a small device mesa (r = 180 µm) were measured on a pure Ge sample (0% Sn) which was irradiated at 2×10^{14} cm^{-2}.

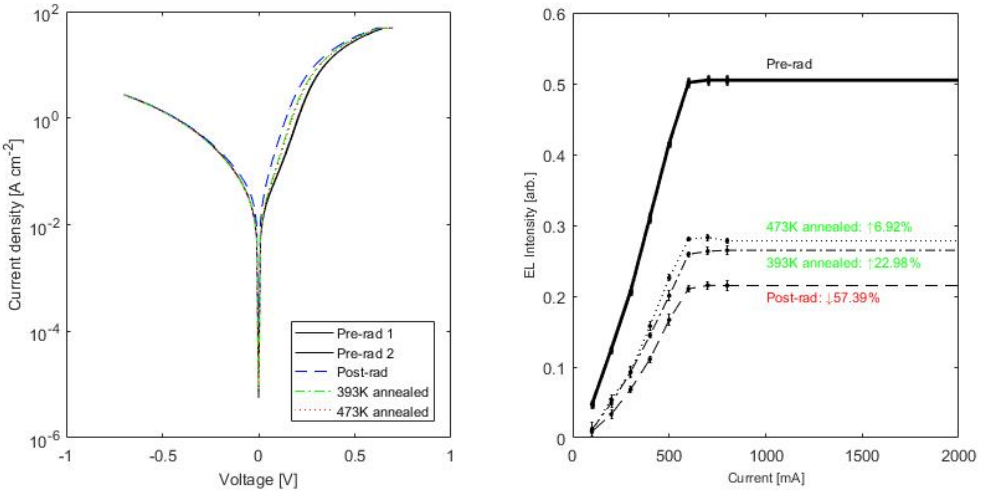

Figure 39. One of the majority I-V curves (left) and its corresponding EL plots (right) in which changes in current are relatively small, but changes in EL are large. Both I-V data and EL data of a small device mesa (r = 180 µm) were measured on a pure Ge sample (0% Sn) which was irradiated at 4×10^{13} cm^{-2}.

Nineteen of forty-five cases showed a clear increase in leakage current density following irradiation as their EL degraded, and one of thirty cases showed a clear decrease in leakage current density following annealing steps as its EL recovered. While

a few I-V plots showed the expected relationship between the EL degradation and the leakage current density, most of the I-V plots did not show obvious changes in leakage current density (Figure 39) between the four experimental stages (i.e. pre-rad, post-rad, 393 K anneal and 473 K anneal) in log scale. Therefore, new plots (Figure 40 and Figure 41) were created to show the changes in leakage current density following irradiation; the Δ leakage current density was calculated by subtracting the pre-rad leakage current density from the post-rad leakage current density.

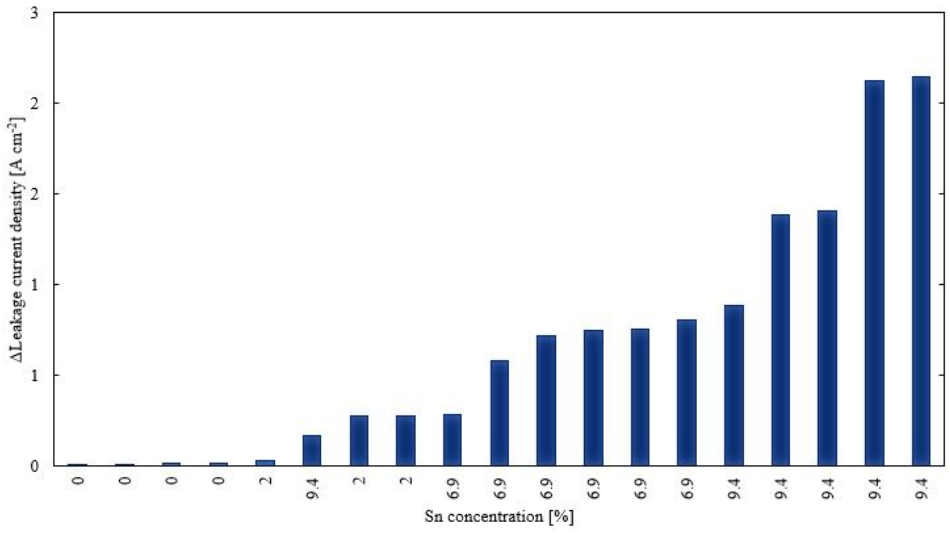

Figure 40. The relationship between the changes in leakage current density and Sn concentration. The samples were irradiated at 4×10^{13} cm^{-2}. The Δ leakage current densities of all devices are listed from smallest to largest (left to right).

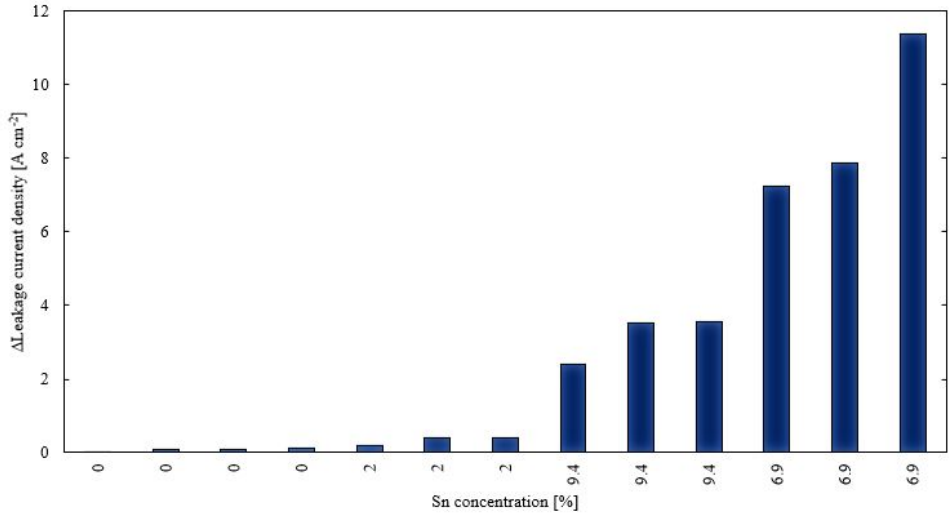

Figure 41. The relationship between the changes in leakage current density and Sn concentration. The samples were irradiated at 4×10^{14} cm^{-2}. The Δ leakage current densities of all devices are listed from smallest to largest (left to right).

In Figure 40 and Figure 41, the plot trends did not follow the original expectation; if the higher Sn samples were less susceptible to displacement damage (according to ΔEL analysis) and their Δ leakage current densities could presumably reflect the radiation response, then the Δ leakage current densities in higher Sn samples should be smaller. Because the outcome of this experiment was vastly different than the expectation, another set of plots were constructed to validate the relationship between ΔEL and Δ leakage current densities (Figure 42).

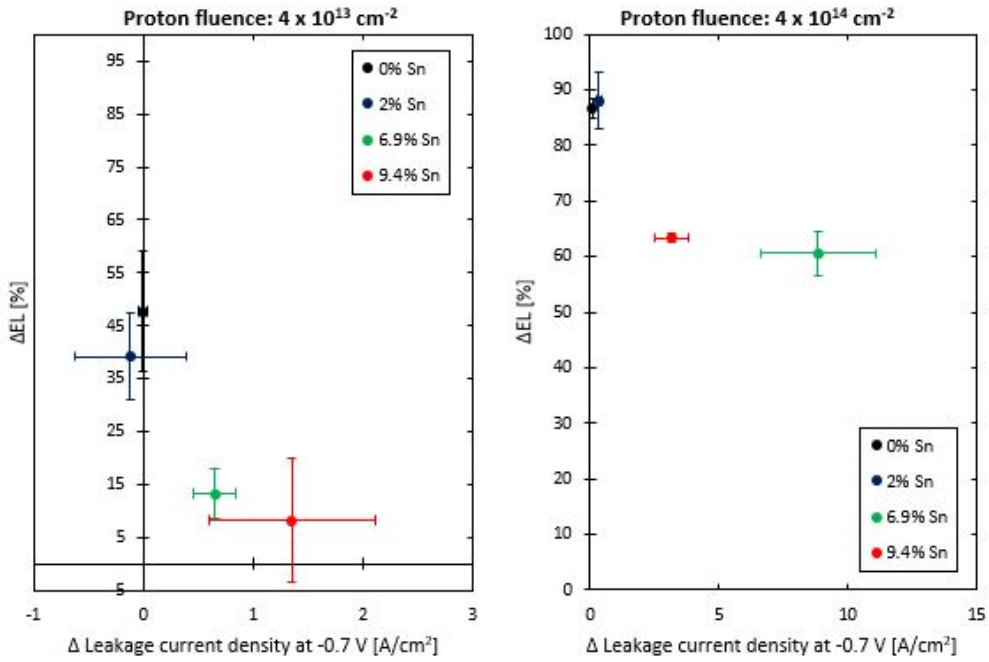

Figure 42. ΔEL versus Δ leakage current density plots showing that the higher Sn samples generally had a larger Δ leakage current density, and their EL degraded relatively lower than the ΔEL of the lower Sn samples following irradiation.

Samples with a high leakage current before irradiation increased by a greater magnitude than the smaller Sn samples' leakage currant following irradiation (Figure 42 and Figure 43). Because the same amount of fluence was applied, the number of newly introduced defects should be generally the same regardless of the Sn concentration (see the SRIM results in appendix). The resulting defect energy levels could, in principle, vary with Sn content (as will be shown in the DLTS results) and make the devices more prone (to greater or lesser degrees) to Shockley Read Hall (SRH) non-radiative recombination, but these same defects would make the devices more prone to leakage current from trap-assisted generation in similar proportion, so these results suggest the dominant mechanism for the observed radiation-induced leakage current is not SRH trap-assisted generation.

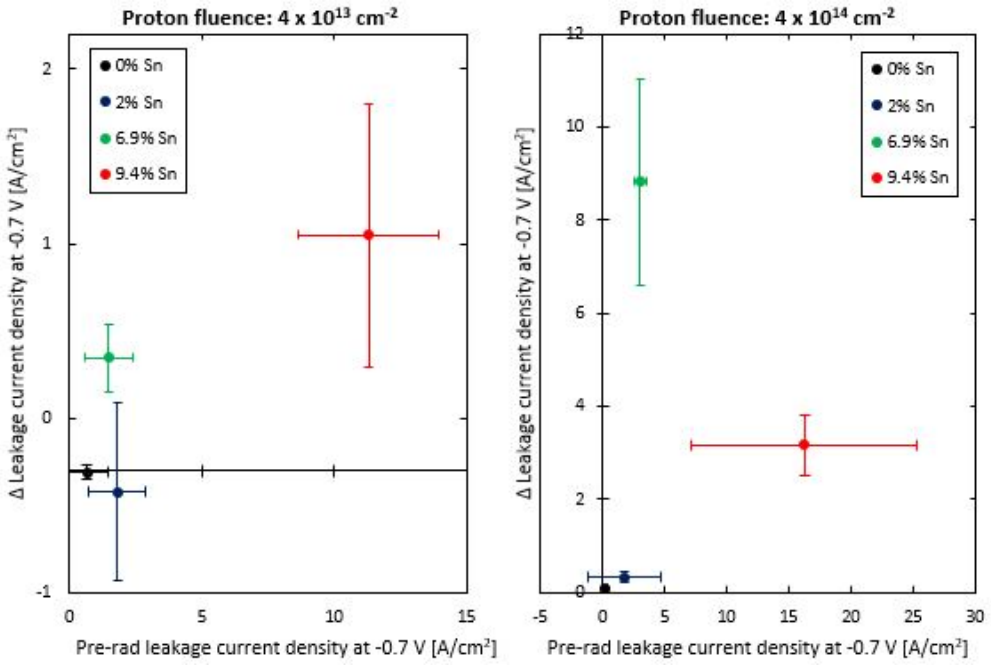

Figure 43. The Δ leakage current density and the pre-rad leakage current density relationship showing that higher Sn samples generally had a larger leakage current density (less ideal diode quality) prior to irradiation, and their Δ leakage current was generally larger as well.

4.3.3 Challenges in I-V Analysis

During the second experiment series, pre-rad I-V data were collected twice at different times in order to observe how much the pre-rad leakage current density could vary without controlled external factors applied (i.e. high heat for anneal or proton irradiation). Six of thirty-three I-V results showed significant change between the two different pre-rad plots (Figure 44). The first pre-rad data (dotted lines) were collected as soon as the samples were packaged and wire-bonded, before EL measurements were taken. The second pre-rad data (solid lines) were collected after EL measurements. High applied current during EL measurements was considered the main factor that left permanent damage on a few sensitive devices and changed their I-V profiles permanently. With these fragile device cases being noticed, the credibility of I-V

analysis diminished since the observed changes in I-V data could not only represent the displacement effects, but also the damage possibly introduced via high applied current.

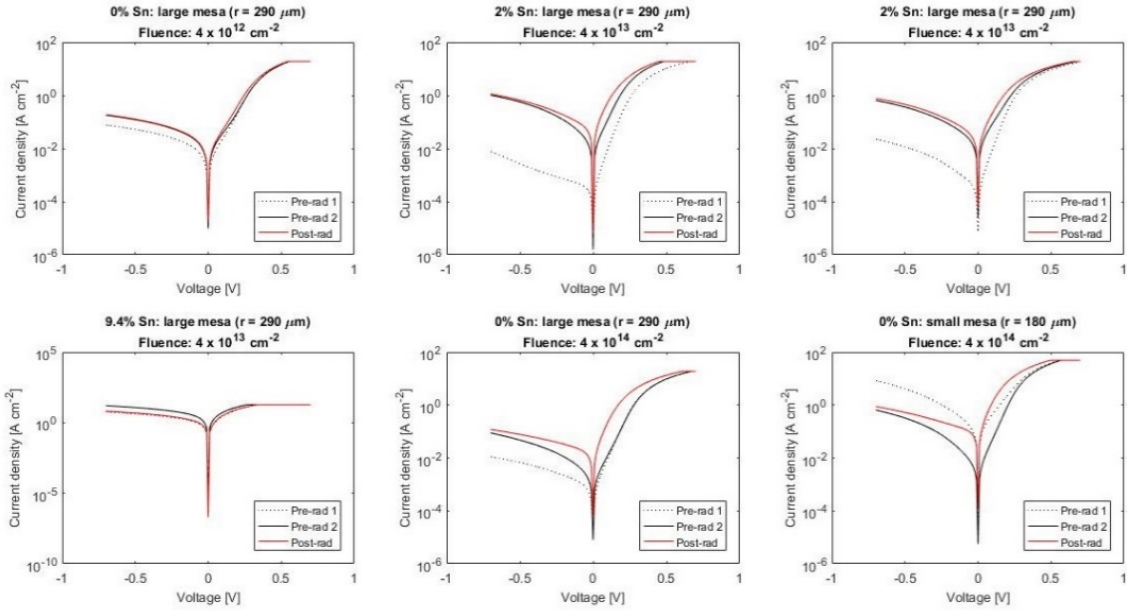

Figure 44. I-V results from the second experiment series showing significant change between the two pre-rad plots.

Five of forty-five cases showed closed-circuit breakdowns. When a device was broken as a closed-circuit, it resulted in I-V curves as shown in Figure 45 (see the 393 K and 474 K annealing plots in the left figure and the post-rad, 393 K and 474 K, annealing plots in the right figure). Although the 15% duty cycle selection was deemed safe (well below the 50% mentioned in the ASU paper [21]) for the samples when setting up the EL equipment, a few fragile samples were damaged when the applied current exceeded 1.5 A during EL measurement. However, the number of broken devices due to high applied current were considerably low, so the final I-V analysis was not greatly influenced. All of these data points considered “closed-circuit breakdowns” were removed from the plots.

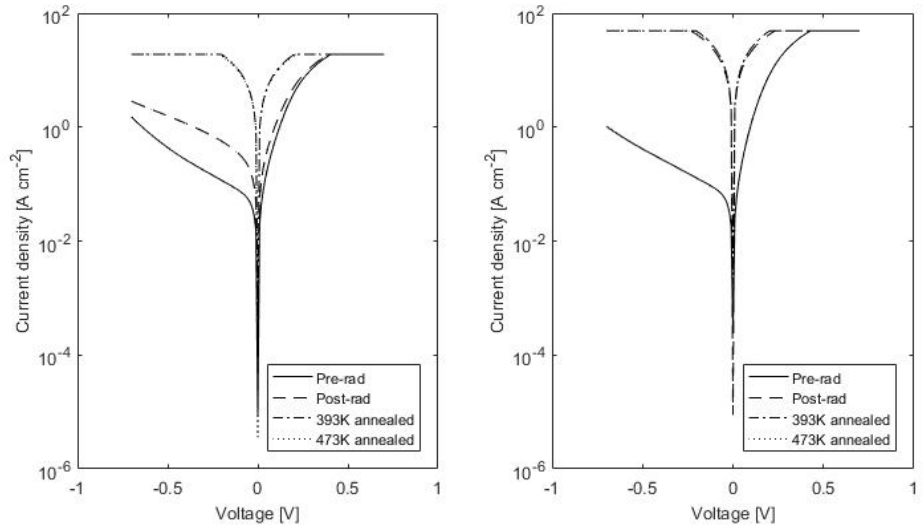

Figure 45. A large device mesa (left) and a small mesa (right) of r = 290 µm and r = 180 µm respectively on a 6.9% Sn sample irradiated at 2 × 10^{14} cm^{-2}. These I-V plots show examples of closed-circuit breakdowns; the large mesa was broken down right after the post-rad measurement, while the small mesa was broken down after the pre-rad measurement.

4.4 C-V Analysis

Pre-rad and post-rad C-V data were collected from samples irradiated at 4 × 10^{14} cm^{-2} to study the samples' doping profile and validate if the magnitude of carrier concentration, n_s, changed via displacement damage. The Semetrol software was used to collect the following data: capacitance (C), voltage (V), depletion width (W), and carrier concentration. More precisely, the W and the carrier concentration data was computed with C [23]. For C, the software used the following the equation:

$$C = A\sqrt{\frac{q\varepsilon_r\varepsilon_0 n_s}{2(V_{bi}-V)}} \tag{4}$$

where ε_r is the relative dielectric constant which was set at 14, ε_0 is the permittivity of vacuum, and V_{bi} is the calculated built-in potential. Then, the differential slope of the

linear region of the $1/C^2$ plot provided the carrier concentration. The W was collected utilizing the following equation with C:

$$W = \frac{\varepsilon_r \varepsilon_0 A}{C} \tag{5}$$

where A is the area of device mesa. With these data, the doping profile plots and bias-W plots were created for analysis (pg. 90).

4.4.1 Doping Profile Analysis

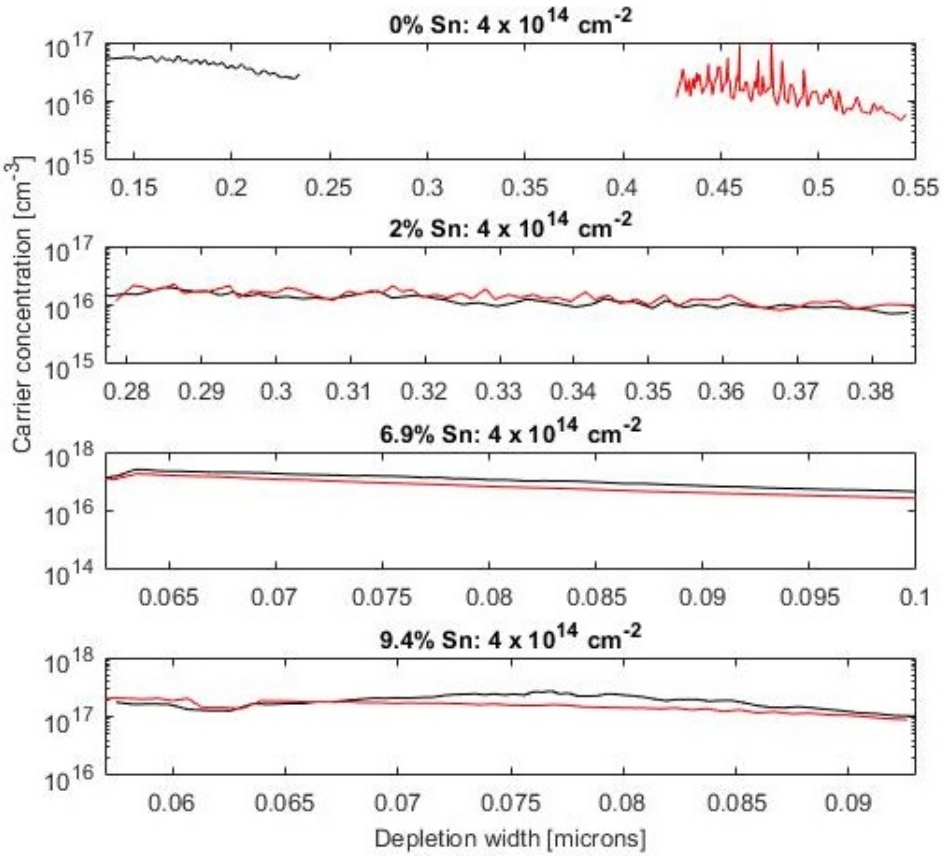

Figure 46. Doping profile plots collected at 150 K. Pre-rad plots (in black) and post-rad plots (in red) are shown to compare the change in carrier concentrations due to displacement damage. The plots represent various Sn samples irradiated at 4×10^{14} cm^{-2}.

Figure 46 shows the doping profiles measured at 150 K to observe changes in carrier concentration by displacement damage; 100 K to 150 K was a temperature range in

which dominant hole trapping occurred in the DLTS measurement, and good C-V measurements of the high Sn devices could not be taken at room temperature due to high leakage current. In log scale, the magnitude of carrier concentrations in samples did not appear to change much after being irradiated, except in the 0% Sn sample. However, the raw data indicated there were changes on the order of 10^{16} cm^{-3} on average. The calculated carrier concentrations gradually dropped as the W increased, likely corresponding to increasing leakage current at higher reverse bias. A fixed parasitic capacitance can result in a doping profile plot that appears to increase as the distance from the junction increases. Parasitic capacitance is typically unwanted as it could be an indication of a design/manufacturing flaw caused by proximity between the electronic components (i.e. the different layers in a p-i-n structure); the electric field between layers causes an electric charge to be stored unintentionally while bias is applied. The doping profile plots showed the carrier concentration decreased rather than increased which meant little to no parasitic capacitance existed [23].

Assuming the Semetrol calculated W accurately, the large W shift seen in the 0% sample plot (Figure 46) must be considered further. The reason for this W shift was a change in carrier concentration; the post-rad carrier concentration was lower than the pre-rad carrier concentration. Considering that the pure Ge samples ($x = 0$) were n-type and all other samples with Sn were p-type, more radiation-induced defects (i.e. carrier traps) below the Fermi level could have taken electrons out of the conduction band in the pure Ge samples.

4.4.2 Capacitance-Conductance-Voltage Analysis

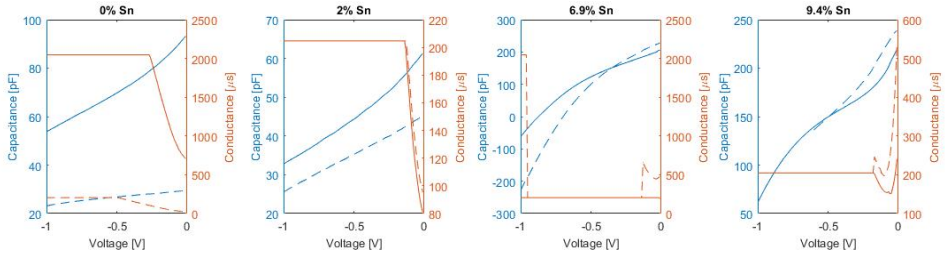

Figure 47. Capacitance-Conductance-Voltage plots of devices which were irradiated at 4×10^{14} cm^{-2} fluence. The solid lines represent pre-rad data and the dashed lines represent post-rad data. The range for the reverse bias swipe was -1 V to 0 V. The chamber temperature during measurement was 150 K.

Figure 47 shows the capacitance and conductance profiles of the corresponding plots in Figure 46 at 150 K. The range of applied reverse bias for these measurements was -1 V to 0 V, so the positive slope of the linear capacitance plots was captured; the bias range that provided the negative slope of the linear capacitance plots was not preferred for DLTS measurement because the decreasing capacitance could indicate that the diode started to conduct too much current for an accurate capacitance reading. On that note, if the device was fully depleted, the capacitance would not change with an increasing reverse bias [23]. Prior to the DLTS measurements, analyzing the C-V plots was necessary to help predict appropriate voltage ranges. For instance, an abnormal capacitance plot (i.e. non-linear plot) could indicate that the voltage range was set to measure an undesired point in a diode such as bulk, substrate, etc. As far as radiation effects go, the magnitude of C decreased after irradiation in most cases. The first plot in Figure 47 corresponds to the first plot in Figure 46. When considering (5) which showed that C and W were inversely related, the large C drop was explained. Overall, all of the plots (pre-rad and post-rad) maintained linearity within the selected bias range; this

indicated that the selected voltage parameters would enable consistent DLTS measuring conditions before and after irradiation.

Beside the capacitance, conductance data were plotted in order to show a bias point where the conductance plot and the capacitance plot intersect (Figure 47). All samples showed low conductance in the μs scale in both the pre-rad and post-rad state. When considering the radiation effects, the conductance remained almost the same in most cases after the samples were irradiated; the pure Ge sample irradiated at 4×10^{14} cm^{-2} indicated significant conductance decrease. Since conductance is given by either I/V or 1/R, the increase in resistance due to an increase in W could have caused the decrease in conductance. Overall, C-V measurements were good practice prior to DLTS analysis, helping determine carrier concentration and the device regions that could be scanned with the voltages used in DLTS.

4.5 DLTS Analysis

Figure 81 through Figure 85 show the DLTS rate-window (545 s^{-1}) spectra of hole traps in the 0% to 9.4% Sn samples which were irradiated at 4×10^{14} cm^{-2} (with the exception of the 5.3% sample which was irradiated at 2×10^{14} cm^{-2} prior to this study). A couple of these plots (depicting 0% and 9.4% Sn samples) utilized 383 K anneal data because they displayed the peak of interest most clearly. Considering that electron traps are dominant in Ge samples (i.e. hole traps are dominant in GeSn alloys), DLTS parameters and measuring techniques had to be employed according to each sample's majority carrier type in order to capture the spectra for hole traps exclusively: the current injection DLTS technique with 0.6 V forward bias was used to capture spectra for

minority carrier (hole) traps in pure Ge samples, whereas, the conventional DLTS technique with 0 V forward bias was used to capture spectra for majority carrier (hole) traps in GeSn samples. The actual DLTS parameters used for each sample are indicated below their respective rate-window figures in Appendix C.

The underlying Gaussian peak positions, magnitudes, and widths were determined from the measured DLTS spectra using the "GRG Nonlinear" option in Excel's "Solver" add-in which performed the least squares regression fitting. Because a variety of different peak combinations could provide equally good fits, the fitting results had the potential to be misleading. However, many anneal data of the same device showed consistent fitting results, and that enhanced confidence in the results of the fitting procedure. The dominant deep-level traps (labeled H1 in Figure 81 through Figure 85) at higher temperatures were presumed to be the (-/0) transition of a vacancy-phosphorus (V_{Ge}-P) complex based on literature review and knowledge that phosphorous was used in the device processing. Based on Secondary Ion Mass Spectroscopy (SIMS) measurements by ASU [24], the possibility of a small amount of phosphorous ($< 10^{16}$ cm^{-3}) existing in the as-grown intrinsic region could not be ruled out. Phosphorus, as a group V element, is an effective trap for vacancies in Ge due to the strong Coulomb interactions between the positively charged donor atoms and negatively charged vacancies [25]. Depending on the amount of Sn included in samples, these effective V_{Ge}-P complex hole traps appeared at different energy levels in the band gap following irradiation. The apparent activation energies of these hole traps were computed via Arrhenius plot fitting; those computed values are shown in Table 5 and Table 8 (as a precursor product to Table 5, Table 8 shows the energy values that were derived from Arrhenius plot fitting of the

main peak identified by stable temperature spectra within the overlapping peaks, without deconvolution). The sum of overlapping peaks should have an activation energy not too different from the energy of the V_{Ge}-P peak derived from Gaussian deconvolution in the Semetrol software if the presumed V_{Ge}-P peak was dominant in each sample. Comparison of the values in both tables gave confidence in calculating activation energies based on Arrhenius fitting of deconvoluted V_{Ge}-P peaks. The apparent cross section inferred from Arrhenius fitting were on the order of 10^{-13} cm^2, which is consistent with a previously reported value of 9×10^{-13} cm^2 for this defect in pure Ge, and the same report suggests the actual value (extrapolated to 1/T = 0) is on the order of 10^{-14} cm^2 [26]. The measured cross section values in Table 5 had large uncertainties compared to the measured activation energies, and they were thus not used to support any of the following analysis and conclusions.

Table 5. Summary of activation energies (determined for the presumed V_{Ge}-P hole trap peak) at each Sn concentration. $E_{P\text{-}V\ trap}$ represents the activation energies of V_{Ge}-P hole traps. $\sigma_{P\text{-}V\ trap}$ represents the cross sections of the hole traps.

Sn Content [%]	Deconvolved $E_{V\text{-}P\ trap}$ [eV]	$E_{V\text{-}P\ trap}$ Uncertainty	$\sigma_{V\text{-}P\ trap}$ [cm^2]	$\sigma_{V\text{-}P\ trap}$ Uncertainty	$T_{peak\ @\ 545\ Hz}$ [K]	Direct $E_{V\text{-}P\ trap}$ [eV]
0	0.35	0.015	1×10^{-12}	Large	178	0.35
2	0.30	0.02	1×10^{-13}	±10×	146	0.30
5.3	0.21	0.03	1×10^{-13}	Large	106	0.20
6.9	0.17	0.03	1×10^{-15}	±10×	97	0.21
9.4	0.16	0.03	1×10^{-12}	Large	92	0.12

When the dominant-thermally stable peak in each sample was considered V_{Ge}-P traps, V_{Ge}-P activation energies could be manually calculated to confirm the validity of the measured values shown in Table 5 (the activation energies from deconvoluted V_{Ge}-P

in the rate-window plots can be found in the 2nd column; the manually calculated activation energies can be found in the 7th column) using the following DLTS equation:

$$E_{V_{Ge}-\mathrm{P}\ trap} = k * T * \{\ln(T^2)\} - \ln(\frac{f * \sqrt{T}}{\sigma * v_{th}})\} \quad (6)$$

where k is the Boltzmann constant, 8.617×10^{-5} eV·K^{-1}, T is the temperature in [K] at which peak/valley occurred in the rate-window plot, f is the rate-window in Hertz [s^{-1}], σ is the assumed V_{Ge}-P cross section in [cm^{-2}], and v_{th} is the thermal velocity in [cm/s]. In this calculation, while V_{Ge}-P activation energy in pure Ge was presumed to be 0.35 eV, the cross section had to be about 5×10^{16} cm^{-2} in order to get a 545 Hz rate window peak at the temperatures observed (shown in the 6th column in Table 5) in their respective DLTS spectra. Keeping these assumed cross section and rate-window values constant in calculations allowed their V_{Ge}-P activation energies to be calculated while T varied in different Sn samples. The measured V_{Ge}-P activation energies roughly matched those of the calculated values in Table 5, roughly validating the experiment results.

Considering that the band gap energies narrowed as Sn content increased in alloys (see the last column in Table 1), V_{Ge}-P trap activation energies were coincidently observed further away from the mid-gap in higher Sn samples following irradiation (Figure 48). According to the plot, the V_{Ge}-P trap activation energies were somewhat parallel and roughly "pinned [27]" to the indirect conduction band edge. The pinned V_{Ge}-P trap energies were deep-level in lower Sn samples and, as the band gap narrowed in higher Sn samples, the V_{Ge}-P trap energy moved closer to the valence band, resulting in less SRH non-radiative recombination. When Figure 49 was created, the 300 K band gap energies were used instead of the 125 K band gap energies (as they were used in

Figure 48) because that temperature was close to room temperature; thus, this figure is thus comparable to the EL results. The delta of V_{Ge}-P activation energies were derived from the comparison between the V_{Ge}-P activation energy of respective Sn content to the V_{Ge}-P activation energy of 0% Sn samples. The previously discovered band gap values [28] were multiplied by 1.091 in order to properly represent the band gap values at 125 K which was the temperature chosen for DLTS analysis.

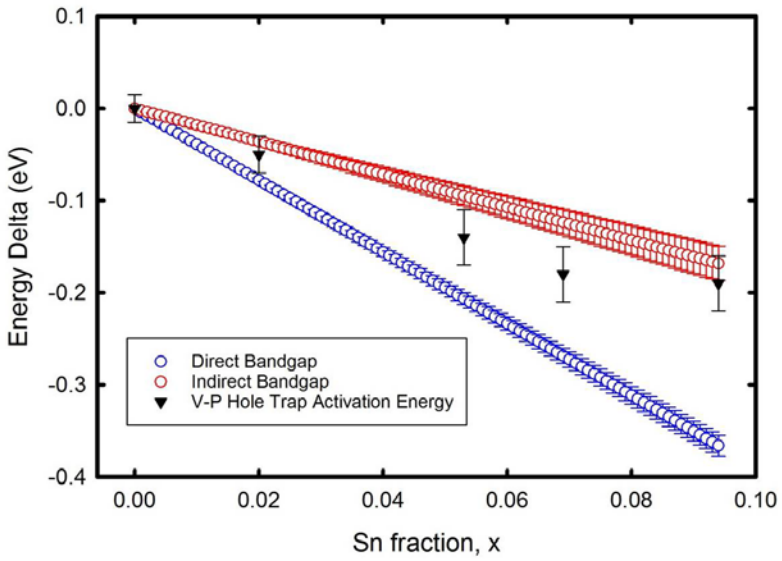

Figure 48. The relationship between the V_{Ge}-P activation energies, the expected direct and indirect band gaps, and Sn concentration.

Besides the presumed V_{Ge}-P peak observed in Figure 81 through Figure 85, two other peaks were observed in the lower temperature range: one was presumed to be the (2-/-) transition of a V_{Ge}-Sn complex and another beneath the convoluted curve was presumed to be a Ge divacancy (V_{Ge}-V_{Ge}) complex. Previous DLTS research of electron-irradiated Ge doped with Sn mentioned that these V_{Ge}-Sn and V_{Ge}-V_{Ge} complexes were less thermally stable than the V_{Ge}-P complex because Sn atoms could not effectively prevent the formation of V_{Ge}-P and the transient enhanced diffusion of phosphorus [25]

[29] [30]. At 333 K anneal, the releasing rate of V_{Ge}-Sn increased the concentration of the more stable V_{Ge}-P complex [25]. Hence, V_{Ge}-P peaks became dominant at higher annealing temperatures while other peaks became smaller.

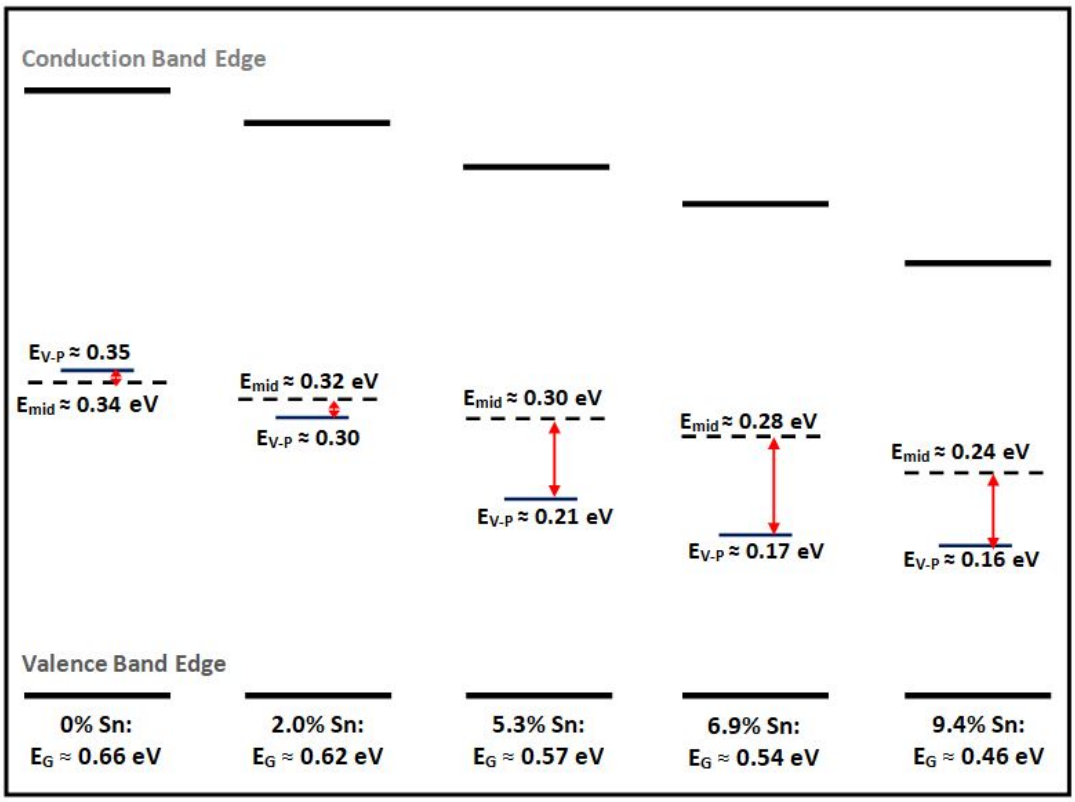

Figure 49. Approximated illustration to visualize the V_{Ge}-P level in various Sn samples that were irradiated at either 2×10^{14} cm^{-2} (5.3% Sn sample) or 4×10^{14} cm^{-2} (all other samples). The V_{Ge}-P energy level approximation will need to be confirmed with further DLTS research in the future. However, these approximated values were sufficient to illustrate the V_{Ge}-P profile in the irradiated samples.

The SRH equation (7) and sub-equations (8) were used to compute the indirect thermal recombination rate with the activation energy of hole traps (E_T) obtained in DLTS [8]. The indirect thermal recombination rates were greater in the higher Sn samples. Assuming variables other than E_T in (7) were relatively constant across different Sn samples (i.e. the result of (7) depends on E_T exclusively), the indirect thermal

recombination rate of each Sn sample could be compared to the rate of the 0% Sn sample, resulting in the ratio plot of Figure 50.

$$\left.\frac{\partial p}{\partial t}\right|_{\substack{i-thermal \\ R-G}} = \left.\frac{\partial n}{\partial t}\right|_{\substack{i-thermal \\ R-G}} = \frac{n_i^2 - np}{\tau_p(n + n_1) + \tau_p(p + p_1)} \tag{7}$$

$$\begin{aligned} n_1 &\equiv n_i e^{(E_T - E_i)/kT} \\ p_1 &\equiv n_i e^{(E_i - E_T)/kT} \end{aligned} \tag{8}$$

This plot shows the indirect thermal recombination ratio at each sample Sn content (black) computed with the SRH equation with the E_T acquired from DLTS. The ΔEL ratio at each sample Sn content (red) was captured in the plot for comparison. Since the majority of samples used for DLTS analysis (all except the 5.3% Sn sample) were irradiated at 4×10^{14} cm^{-2}, the data of Sn samples which were irradiated at 4×10^{14} cm^{-2} were used for the ΔEL ratio plot to match fluence level. In Figure 50, both EL and DLTS results show that high Sn samples were less susceptible to displacement damage because the radiation-induced hole traps were shallow level, producing a relatively higher EL signal with less indirect thermal recombination rates. The magnitude of difference in the two ratio plots did not match very well, which probably reflects deficiencies in the simplified assumptions of the SRH analysis as much as uncertainties in the EL and DLTS results.

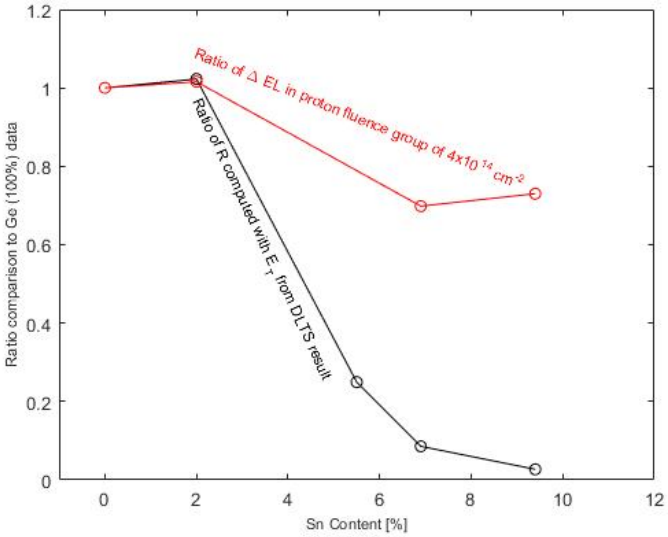

Figure 50. The indirect thermal recombination ratio at each sample Sn content (black) computed with the SRH equation and E_T acquired from DLTS results. ΔEL ratio at each sample Sn content (red) was captured in the plot for comparison.

V. Conclusions

5.1 Research Conclusion

The main result of this research strongly suggests that GeSn alloys with high Sn concentration are more resistant to luminescence degradation effects of displacement damage than their Ge counterparts. The EL experiments showed that $Ge_{1-x}Sn_x$ devices with higher Sn concentration were up to 10 times more resistant to proton displacement damage than the Ge (x = 0) devices. DLTS measurements showed that the dominant radiation-induced deep-level carrier trap (presumed to be a V_{Ge}-P complex) had an energy level that was near mid-gap in the 0% and 2.0% Sn devices, but was far from mid-gap in the 6.9% and 9.4% devices; thus offering explanation for the higher rate of non-radiative recombination in the irradiated 0% and 2.0% Sn devices. While this mechanism was presumed to depend on the presence of P impurities, the result may also be expected to apply to GeSn alloys containing other common group V impurities, such as As and Sb. High concentrations of radiation-induced atomic displacements were necessary to cause appreciable degradation in the EL from these devices, suggesting such light emitting devices would be very tolerant to harsh space radiation environments regardless of Sn concentration. However, GeSn based detector devices may be much less tolerant to trap-assisted generation current resulting from these same concentrations of defects. In fact, the I-V measurement results showed that radiation-induced reverse bias leakage current was up to 10 times greater in the high Sn devices than in the low Sn devices, presumably based on other leakage current mechanisms yet to be quantified, such as surface

conduction paths; these may depend on the total ionizing dose as much as the displacement damage dose.

5.2 Future Work and Recommendations

If a temperature dependent EL setup can be realized, then the results found in this research can be extended to include various temperature effects on EL intensity. In order to accomplish this, the sample has to be kept in a vacuum chamber while the temperature changes; surface effects could be an issue if a vacuum chamber is not utilized. Setting up the equipment to measure EL in the vacuum chamber could be the most challenging task, since positioning the fiber optics to the most optimum light-emitting spot (within 1 mm) is time consuming and challenging. Nevertheless, if the capability to measure the temperature dependent EL is realized, the results could relate better to DLTS research.

Ternary samples (GeSiSn) could have been used for this research instead of binary samples if a sufficient number of samples were available. While Sn content in the i-layer varies from ~3.5% to 11%, the ternary samples include Si content which should be preferably kept constant near 3%; 3% Si content mitigates a low thermal stability issue in samples with > 0.09 Sn content [31]. At high temperatures, metastable Ge and Sn alloys tend to decompose via Sn segregation and phase precipitation, which compromises device functionality and structural integrity. With Si content inclusion, the ternary sample's device properties and band gap structures could differ from binary samples'; for example, the indirect-to-direct cross over point for a ternary sample was approximated around 14.5% Sn whereas binary samples' cross over point was estimated at 6.7% Sn.

Therefore, displacement damage effects in both ternary and binary samples can result in different conclusions. Since only a small number of ternary samples were locally available by the time this research began, this research effort pressed on with binary samples. At some point in the future, results/methods found from this research can support research of the same kind with ternary samples.

As GeSn alloy technology matures, it could replace current photonic/optoelectronic devices used in real space applications. In general, such device capabilities are not limited to light emission, but also light detection. Additional study of the radiation tolerance of detection-related performance parameters (e.g. changes in detectivity and leakage current) would give a more complete picture of the suitability of these materials for harsh radiation environments. Additionally, for both light emission and detection, spectral changes brought about by radiation-induced defects should be studied if a spectroscopic system of sufficient sensitivity is available.

The Van Allen radiation belt must be considered when a space application is studied. Typically, the Van Allen radiation belt traps as much electrons as protons. Heavy ions like protons likely create extended defects and more complex traps when compared to irradiation with light particles such as electrons. However, one of the reference papers mentioned that high energy electrons and low dose proton irradiation can introduce similar defects in Ge [32]; although, increased proton irradiation doses usually lead to the introduction of different and more complex defects. Thus, it is worthwhile to irradiate the GeSn alloys with high energy electrons and compare those electron-induced defect results to the displacement damage results investigated in this research.

Appendix A. SMU (Agilent B2901A) Setup Procedure

The following instructions explain how to start/setup the SMU (Agilent B2901A) to source pulses by receiving a trigger signal from the function generator:

1. Complete the equipment setup as shown in Figure 14
2. Turn on SMU
3. Press “more” on the right side → Press “show pulse” → turn on “pulse” from “off” with dial
4. Change peak to “3 V” and width to “3 ms”
5. From the side options, select “show trigger” → change option for trigger to “manual” → change “period” to “10 ms” under “source”
6. Trigger “Auto” under source → click “more” on the right side → find and click “EXT1” → click “more” on bottom to find/click “I/O” → click “DIO” → click “config” → select function to “trigger in” → select polarity to “pos” → click “ok”
7. Select “count” under source → change to “Inf”
8. Select “config” → press “common” → click “wait” → select state to “off” under source → click “ok”
9. Make sure the SMU and all other device parameters follow as shown in Table 4

Appendix B. SRIM Calculation

Before irradiation, the Stopping and Range of Ions in Matter (SRIM) simulation was used to calculate the number of vacancies created in the intrinsic region of the devices via incident proton and recoiling ions within the crystal. SRIM is a program designed for calculating features of the transport of ions in matter [33]; in this case, the simulation was completed to see the 2 MeV proton beam interaction in the defined crystal structures as shown in Figure 51. The type of samples used in this experiment besides the pure Ge were varied by a Sn content of 2 %, 6.9 %, and 9.4 % (in their intrinsic regions) and were designated PIN 13, PIN 12, and 54 Bp respectively; these samples were GeSn pin diodes grown on n-type Ge buffered Si.

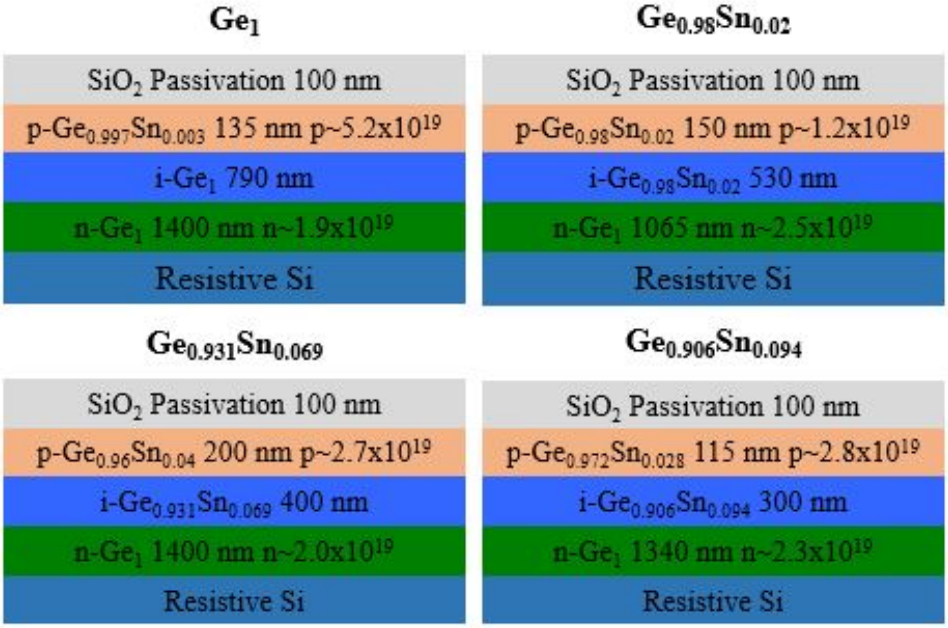

Figure 51. Stack schematics of all the samples used in this experiment. These schematics show the percentage of Sn content, thickness, and doping concentration of each layer.

After the target matter information (Sn content, thickness, doping concentration, etc.) was defined in SRIM, the transporting ion was defined to be 200,000 protons which

had 2 MeV incident energy. The simulations were done in monolayer collision steps, and a single device simulation took nearly two days. The results were plotted as shown in Figure 52. In Figure 52, the blue plots represent the actual SRIM results and the red plots represent the average value of the SRIM results over an individual region.

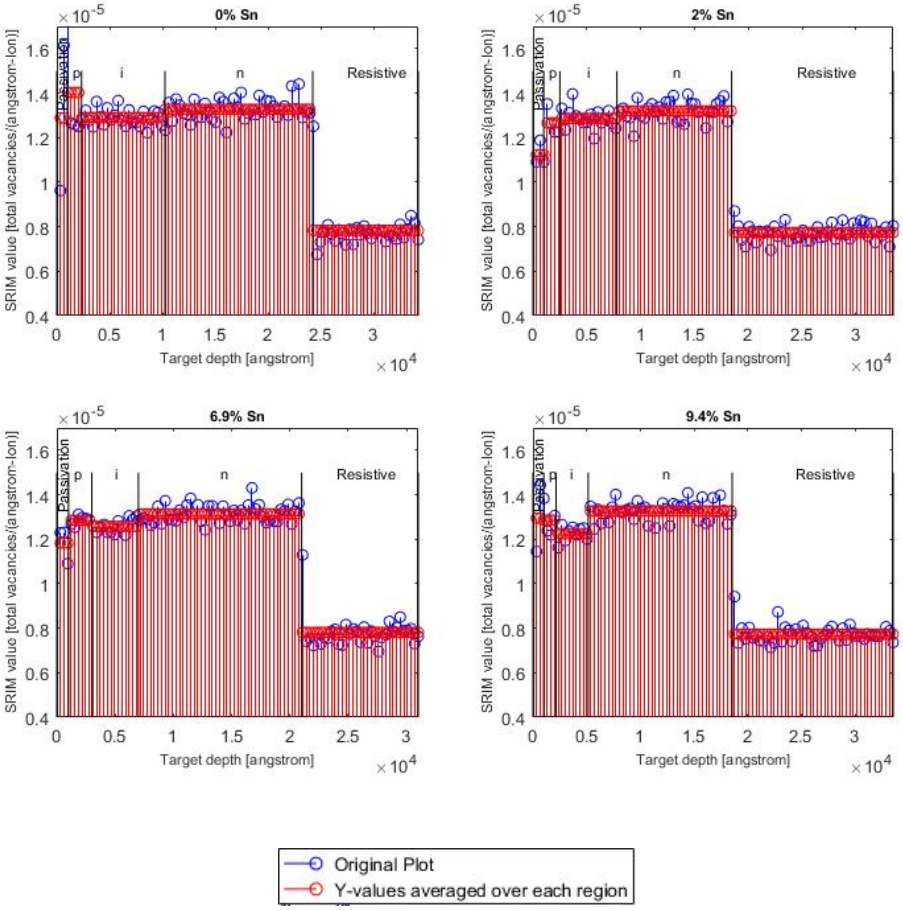

Figure 52. 2 MeV proton irradiation SRIM results showing the number of vacancies created per angstrom per ion in different target regions. The blue plots represent the SRIM results; and the red plots represent the average of the SRIM results over an individual region.

With the numbers that SRIM produced (i.e. vacancies/angstrom-ion), one more step had to be taken to find the vacancy densities. Since we know the fluence of the incident proton beam, vacancy density was calculated by multiplying the averaged SRIM

result (over a region of interest) by corresponding fluence and unit conversion factor (1 Angstrom = 10^{-8} cm):

$$Vacancy\ Density\ \left[\frac{Vacancies}{cm^3}\right] = Avg.SRIM\ value\ \left[\frac{Vacancies}{Angstrom - Ion}\right] * \frac{1[Angstrom]}{10^{-8}[cm]} * Fluence[\frac{Ion}{cm^2}] \quad (9)$$

Table 6. The initial vacancy densities created in the intrinsic regions of each device.

Sample ID	Sn content [%]	Vacancy density over i-region			
		Proton fluence of 4×10^{12} cm^{-2} [Vacancies/(cm3)]	Proton fluence of 4×10^{13} cm^{-2} [Vacancies/(cm3)]	Proton fluence of 2×10^{14} cm^{-2} [Vacancies/(cm3)]	Proton fluence of 4×10^{14} cm^{-2} [Vacancies/(cm3)]
Ge 472	0	5.16×10^{15}	5.16×10^{16}	2.58×10^{17}	5.16×10^{17}
PIN 13	2	5.15×10^{15}	5.15×10^{16}	2.57×10^{17}	5.15×10^{17}
PIN 12	6.9	5.03×10^{15}	5.03×10^{16}	2.52×10^{17}	5.03×10^{17}
PIN 54	9.4	4.90×10^{15}	4.90×10^{16}	2.45×10^{17}	4.90×10^{17}

Table 6 shows the vacancy densities created in the intrinsic regions in each device via incident proton and residual recoil effects. Overall, the initial vacancy densities in each fluence group were approximately the same, with a slightly higher initial vacancy density in the samples which had less Sn content. Because the Coulomb potential of the positively charged (4+) Ge and Sn atomic cores are the same, the difference between the two is in the mass. For instance, the maximum energy transfer to target atom during the 2 MeV proton elastic collision for Ge (0.108 MeV) was greater than Sn (0.0667 MeV) because the atomic mass of Ge was lighter than Sn. Nonetheless, it is important to note that the differences in the SRIM results were relatively small which indicated that the EL degradation trend related to Sn content did not result from differences in initial vacancy concentrations.

Additionally, the possibility of p-n nuclear reactions was considered. However, 2 MeV proton energy was much lower than the threshold energy which was the minimum

energy required for nuclear reaction. According to the National Nuclear Data Center (NNDC) database [34], p+ Sn-118 and p+Ge-72 reactions did not undergo p-n reaction when incident proton energy was only 2 MeV.

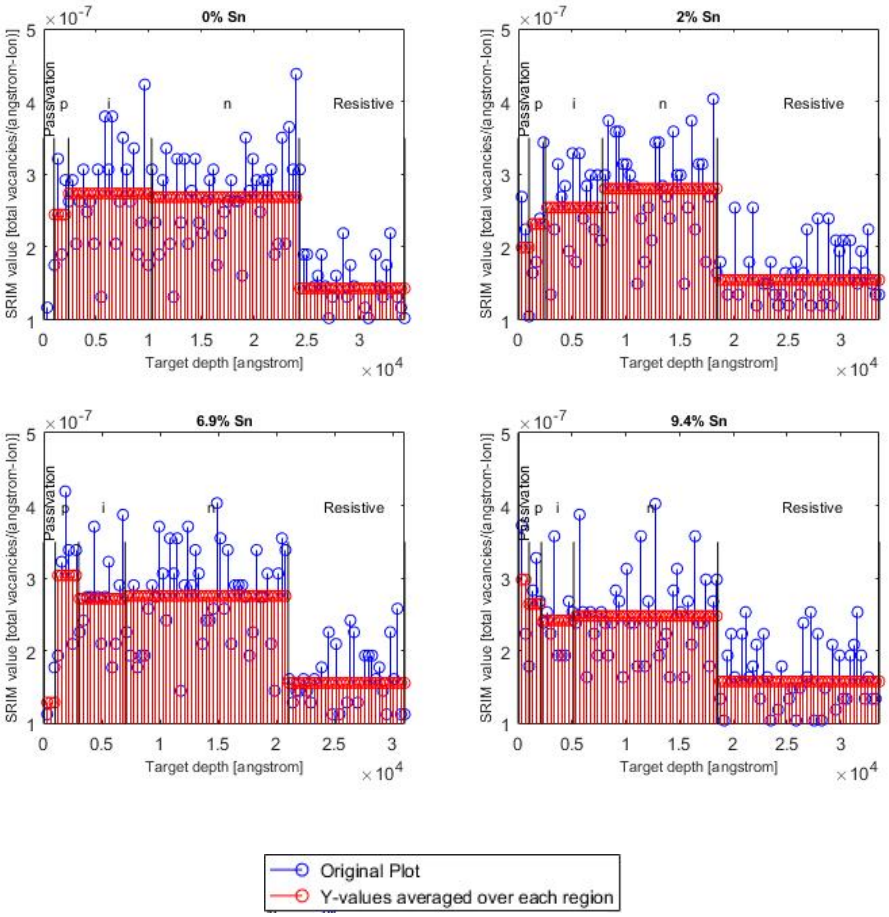

Figure 53. 100 MeV proton irradiation SRIM results showing the number of vacancies created per angstrom per ion at particular matter depths. The blue plots represent the SRIM results; and the red plots represent the average of the SRIM results over an individual region.

As a side reference, 100 MeV SRIM calculation was performed with the same method mentioned above (Figure 53) in order to show that low energy protons cause more displacement damage as compared to high energy protons. As mentioned in the

Theory section of this document (Figure 9), the SRIM results (Figure 54) supported the idea that high energy protons cause a smaller amount of displacement.

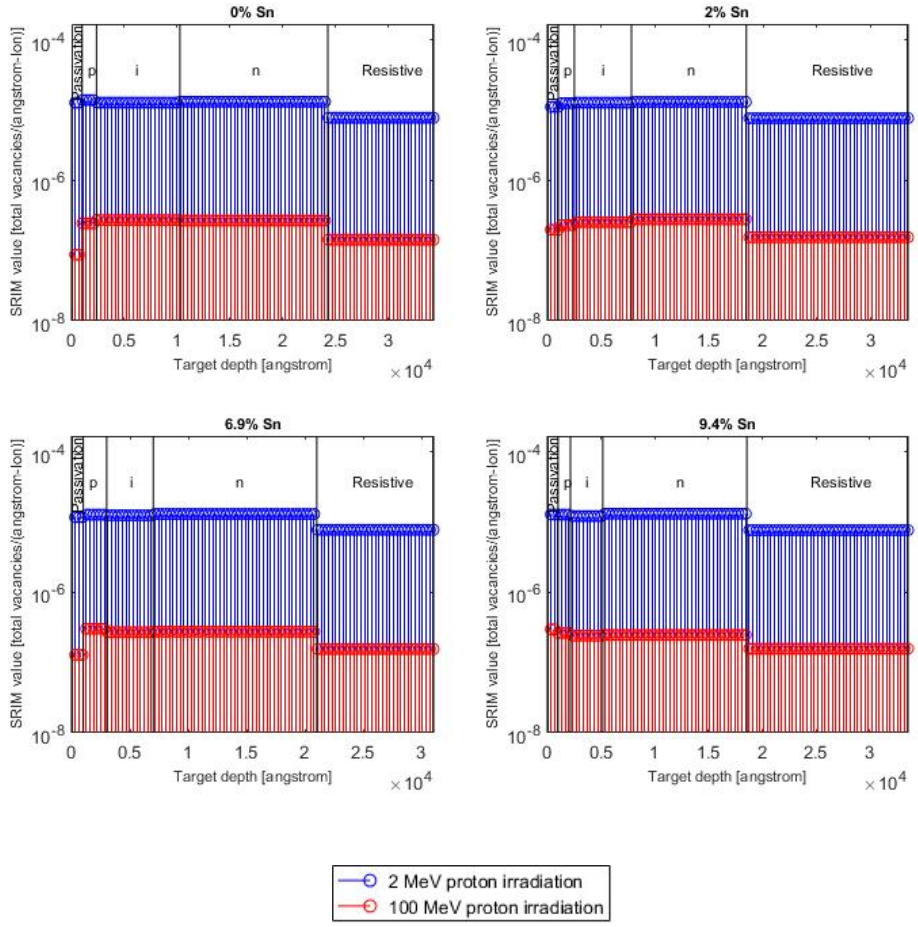

Figure 54. 2 MeV (blue) and 100 MeV (red) SRIM plots show that low energy protons cause greater displacement damage.

Appendix C. Extended Research Data

C.1 I-V Data

Results from the First Experiment Series

0% Sn

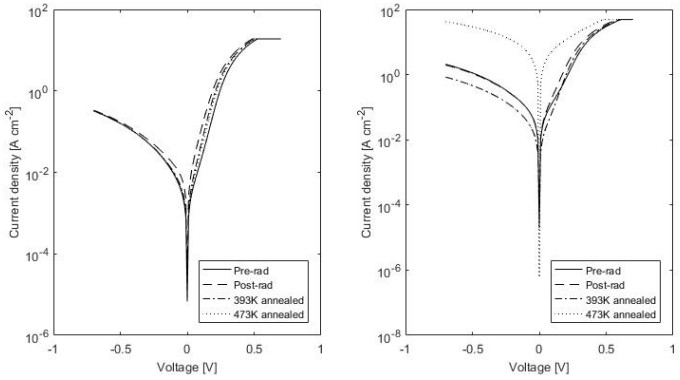

2% Sn

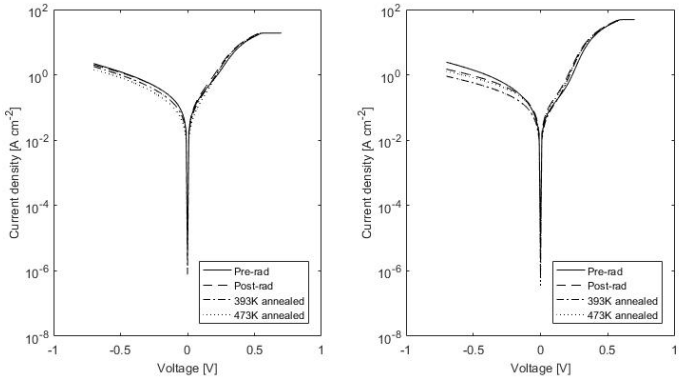

6.9% Sn

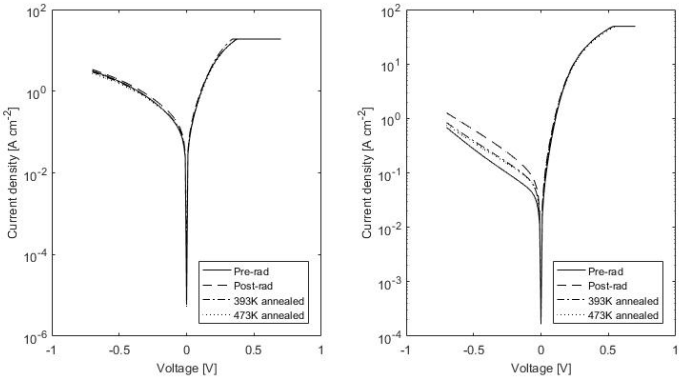

9.4% Sn

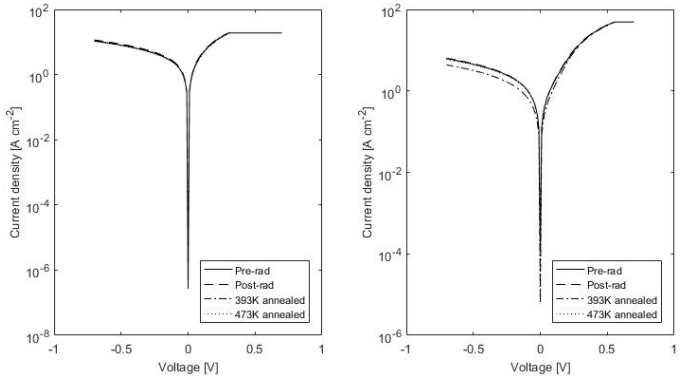

Figure 55. IV plots representative of various Sn content samples which were irradiated at a proton fluence of 4×10^{13} cm^{-2}. Two different device mesa sizes were subjected to the measurement; plots on the left side represent the data of larger mesas and the plots on the right side represent smaller mesas. Each plot contains all data throughout the planned experimental phases (i.e. pre-rad, post-rad, 393 K annealing, and 473 K annealing).

0% Sn

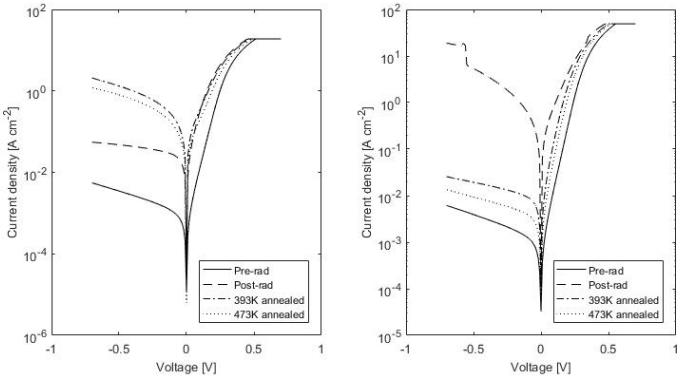

6.9% Sn

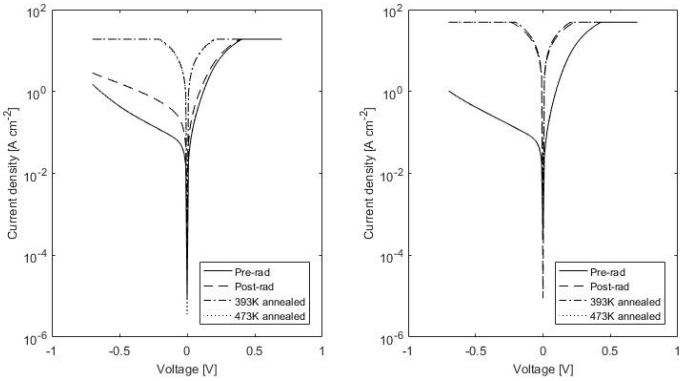

Figure 56. IV plots representative of various Sn content samples which were irradiated at a proton fluence of 2×10^{14} cm^{-2}. Two different device mesa sizes were subjected to the measurement: plots on the left side represented the data of larger mesas and the plots on the right side represented smaller mesas. Each plot contained all of the data throughout the planned phases (i.e. pre-rad, post-rad, 393 K annealing, and 473 K annealing).

Results from the Second Experiment Series

0% Sn

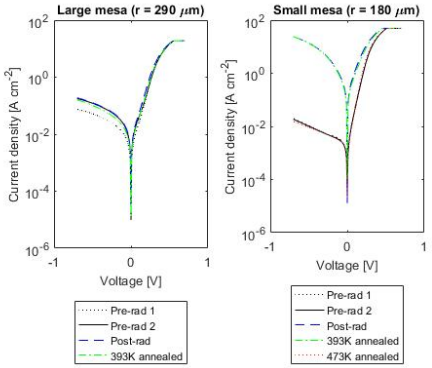

Figure 57. IV plots are shown for a 0% Sn sample which was irradiated at a proton fluence of 4 × 10^{12} cm^{-2}. The right plot contains all data throughout the planned experimental phases (the 473 K annealing plot in red is overlapped with the pre-rad plot in black) whereas the left plot does not contain the 473 K annealing plot because its gold wire was broken during EL measurement.

0% Sn

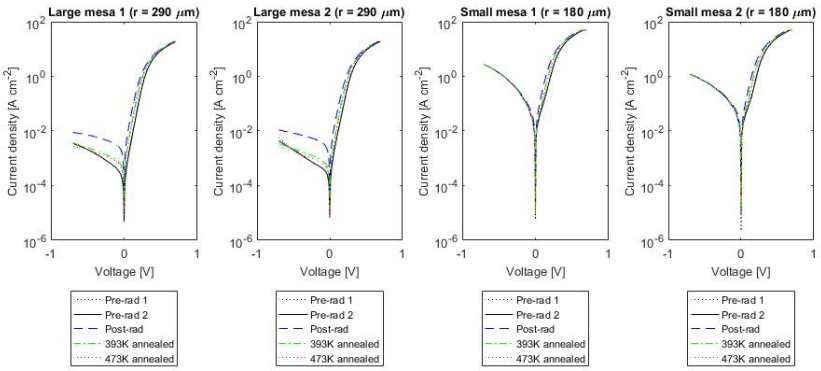

2% Sn

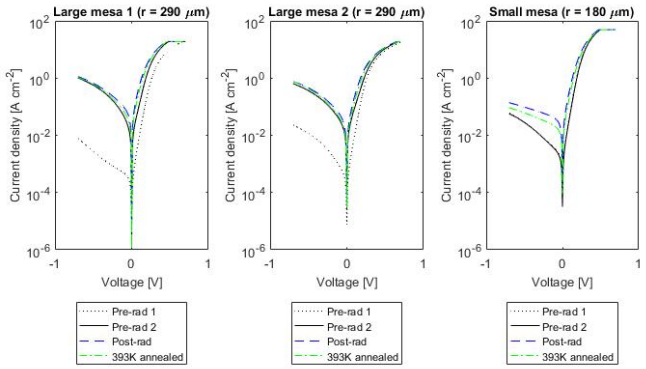

6.9% Sn

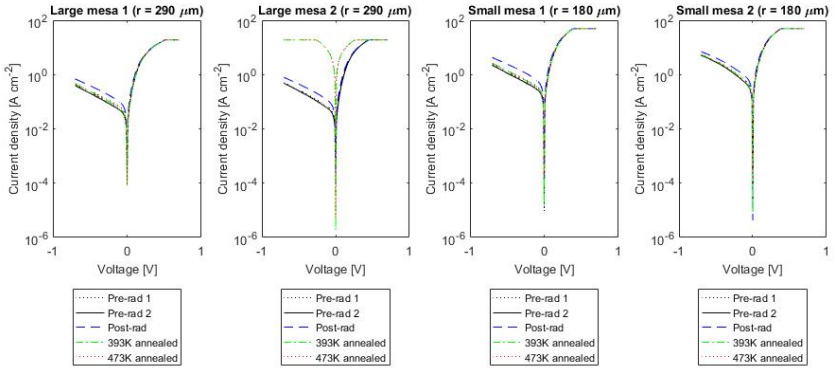

9.4% Sn

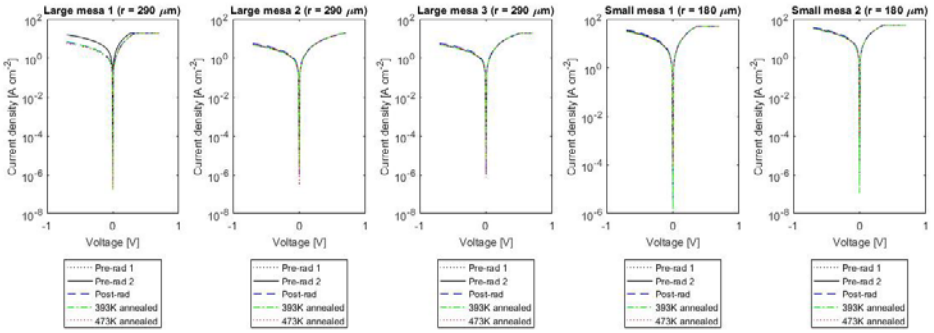

Figure 58. IV plots for various Sn content samples which were irradiated at a proton fluence of 4 × 10^{13} cm^{-2}. The series of plots which represent 2% Sn sample do not contain 473 K anneal data because this particular sample was not annealed along with samples in the same fluence group due to additional DLTS measurements which were performed in different annealing conditions.

0% Sn

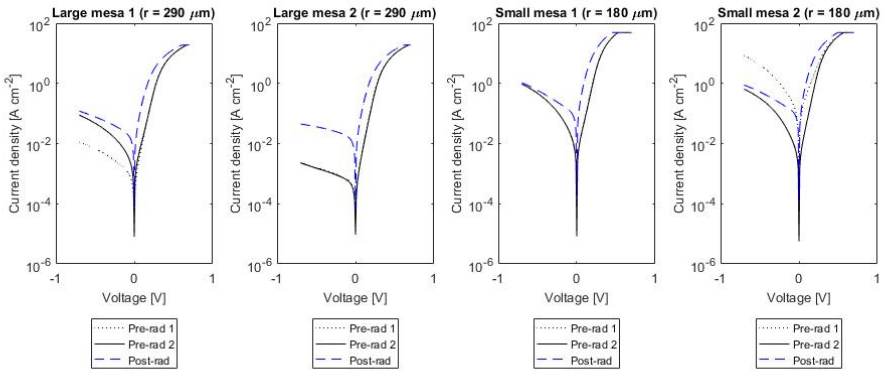

2% Sn

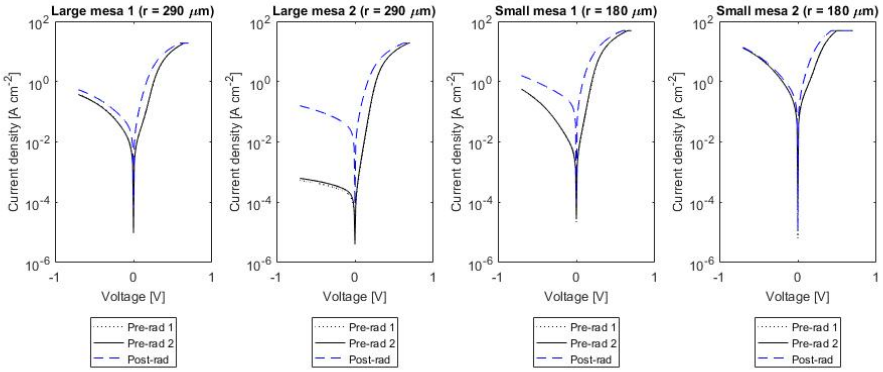

6.9% Sn

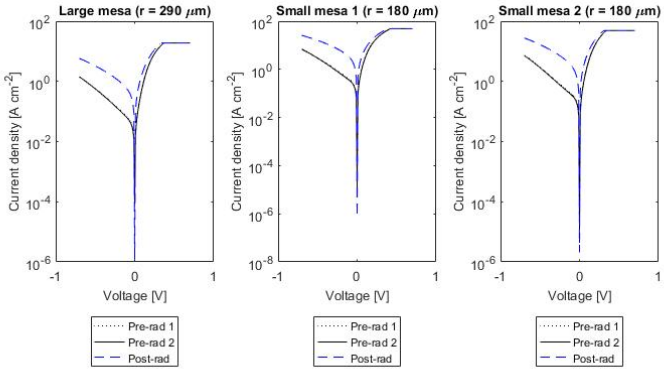

9.4% Sn

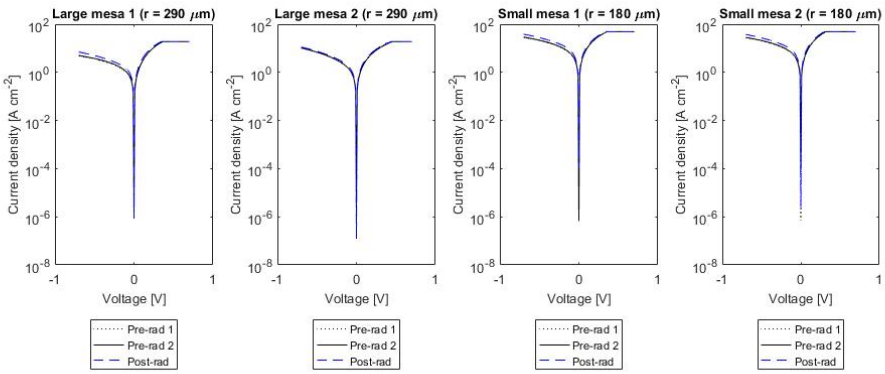

Figure 59. IV plots for various Sn samples which were irradiated at a proton fluence of 4×10^{14} cm^{-2}. Since all samples in this group were subject to a different annealing treatment (30 K increments anneal), IV data of the samples annealed at 393 K and 473 K could not be collected due to logistics and schedule concerns. Hence, only the pre-rad and the post-rad plots were compared in this figure.

C.2 EL Data

Pre-rad EL Comparison

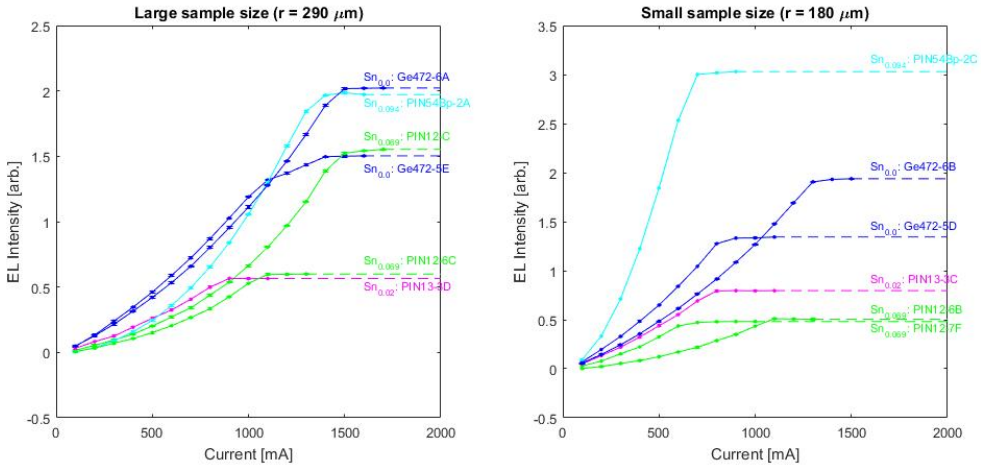

Figure 60. Pre-rad EL intensities of the samples chosen for the first experimental series. These were compared in order to represent the various sample qualities. Blue plots represent the 0% Sn samples; magenta plots represent the 2% Sn samples; cyan plots represent the 6.9% Sn samples; green plots represent the 9.4% Sn samples. EL results were categorized by device mesa size when plotted: large mesas (left) and small mesas (right).

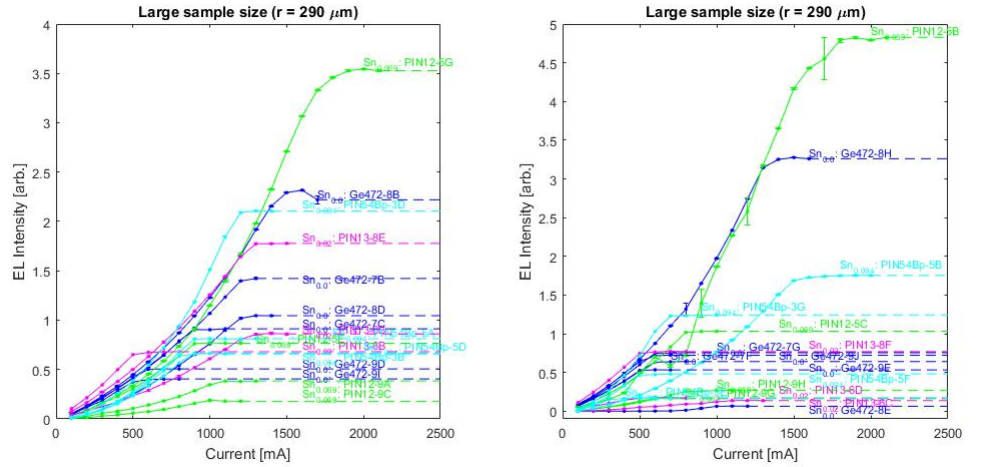

Figure 61. Pre-rad EL intensities of the samples chosen for the second experimental series. These were compared in order to represent the various sample qualities. Blue plots represent the 0% Sn samples; magenta plots represent the 2% Sn samples; cyan plots represent the 6.9% Sn samples; green plots represent the 9.4% Sn samples. EL results were categorized by device mesa size when plotted: large mesas (left) and small mesas (right).

EL Changes Throughout Pre-rad, Post-rad, 393 K Anneal, and 473 K Anneal

0% Sn

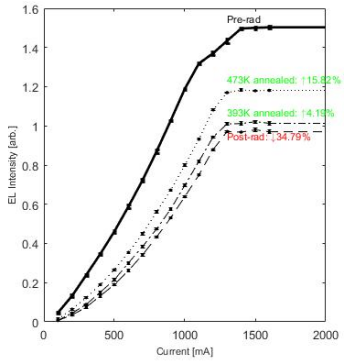

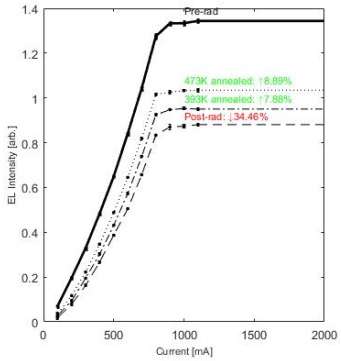

2% Sn

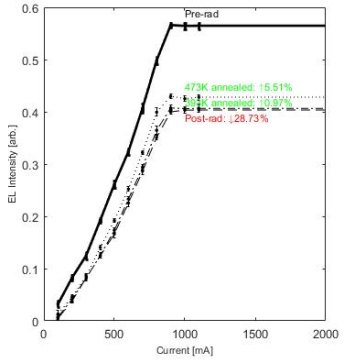

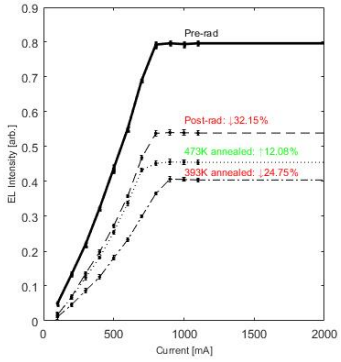

6.9% Sn

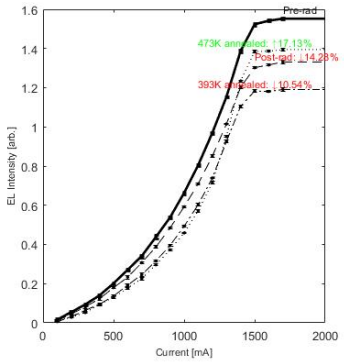

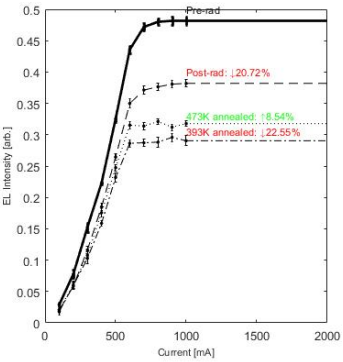

9.4% Sn

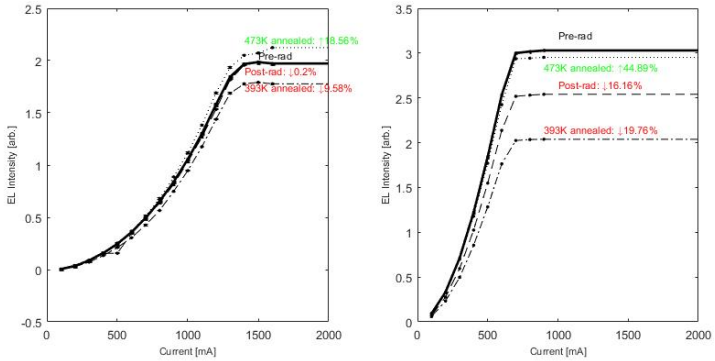

Figure 62. EL plots for various Sn content samples which were irradiated at a proton fluence of 4 × 10^{13} cm^{-2}. Two different device mesa sizes were subjected to measurement: the plots on the left side represent the data of larger mesas and the plots on the right side represent smaller mesas. Each plot contains all data throughout the planned phases (i.e. pre-rad, post-rad, 393 K annealing, and 473 K annealing).

0% Sn

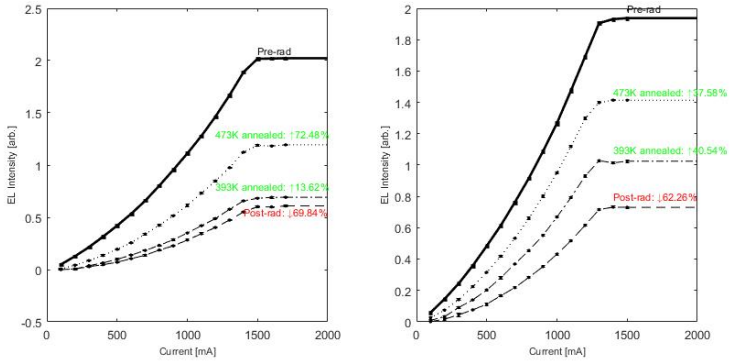

6.9% Sn

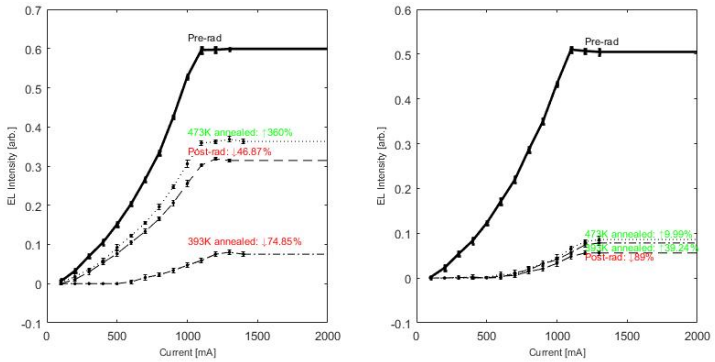

Figure 63. EL plots for various Sn content samples which were irradiated at a proton fluence of 2 × 10^{14} cm^{-2}. Two different device mesas were subjected to the measurement: the plots on the left side represent the data of larger mesas and the plots on the right side represent smaller mesas. Each plot contains all data throughout the planned phases (i.e. pre-rad, post-rad, 393 K annealing, and 473 K annealing).

0% Sn

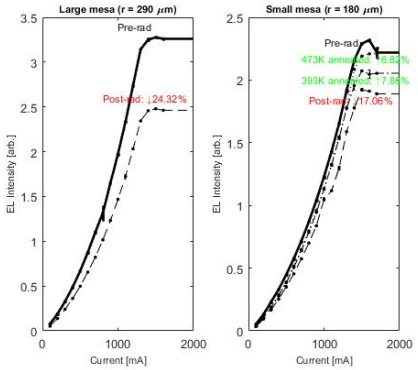

Figure 64. EL plots for a 0% Sn sample which was irradiated at a proton fluence of 4×10^{12} cm^{-2}. The right plot contains all data throughout the planned experimental phases (i.e. pre-rad, post-rad, 393 K anneal, and 473 K anneal) whereas the left plot does not contain a 393 K and 473 K annealing plot because the gold wire was broken during EL measurement.

0% Sn

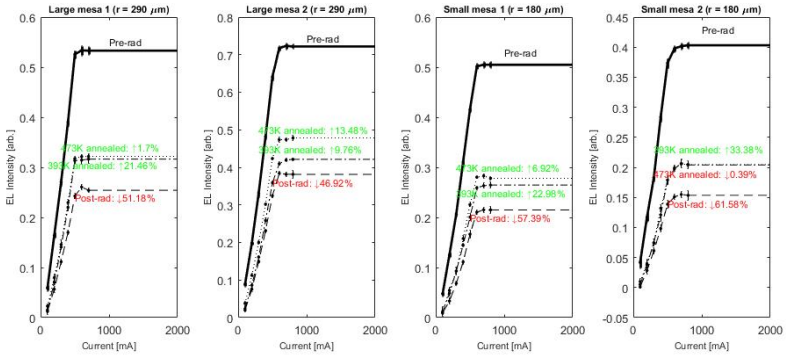

2% Sn

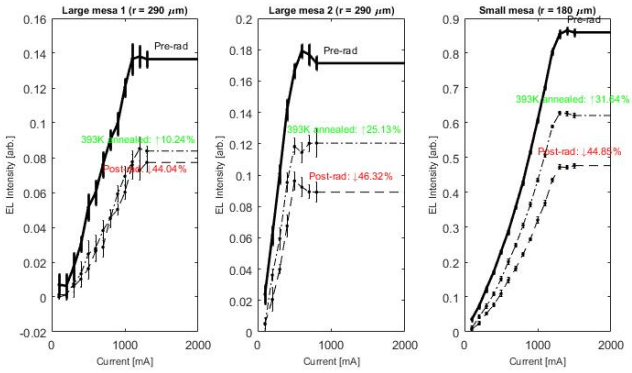

6.9% Sn

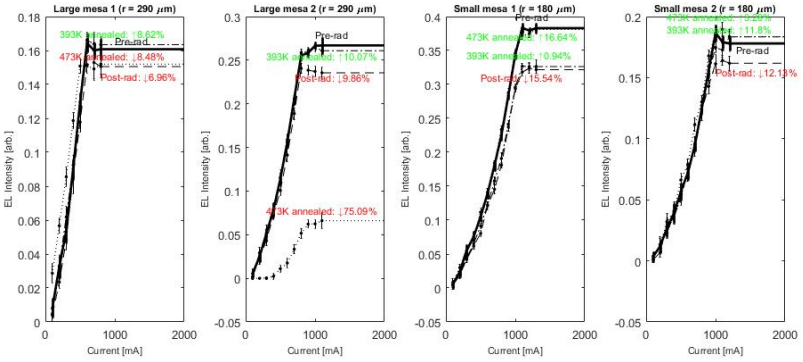

9.4% Sn

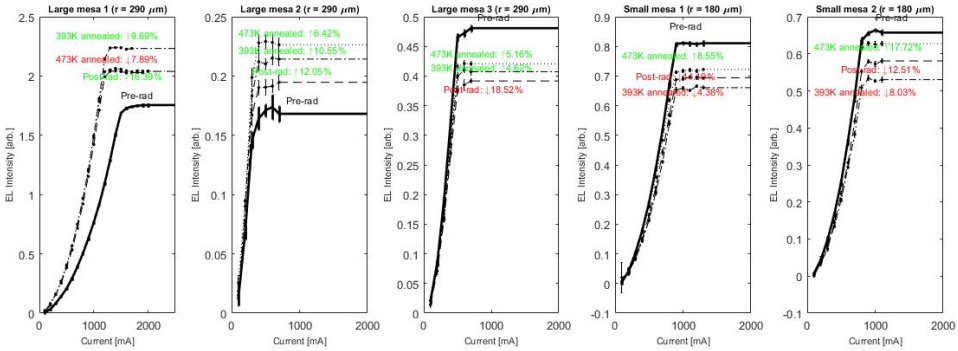

Figure 65. EL plots for various Sn samples which were irradiated at a proton fluence of 4×10^{13} cm^{-2}. The plots which represent 2% Sn sample do not contain 473 K annealing plots because this particular sample was not annealed along with this (fluence) group of samples due to additional DLTS measurements which were performed in different annealing procedures.

0% Sn

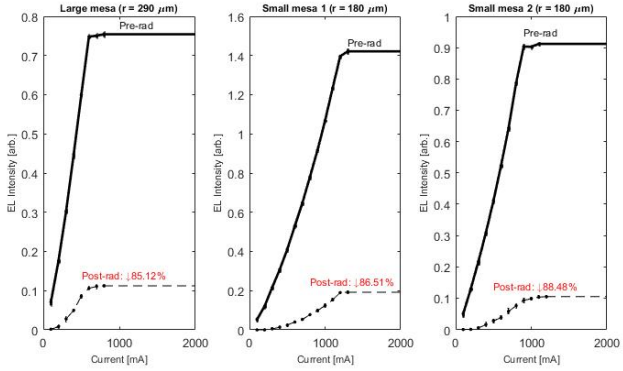

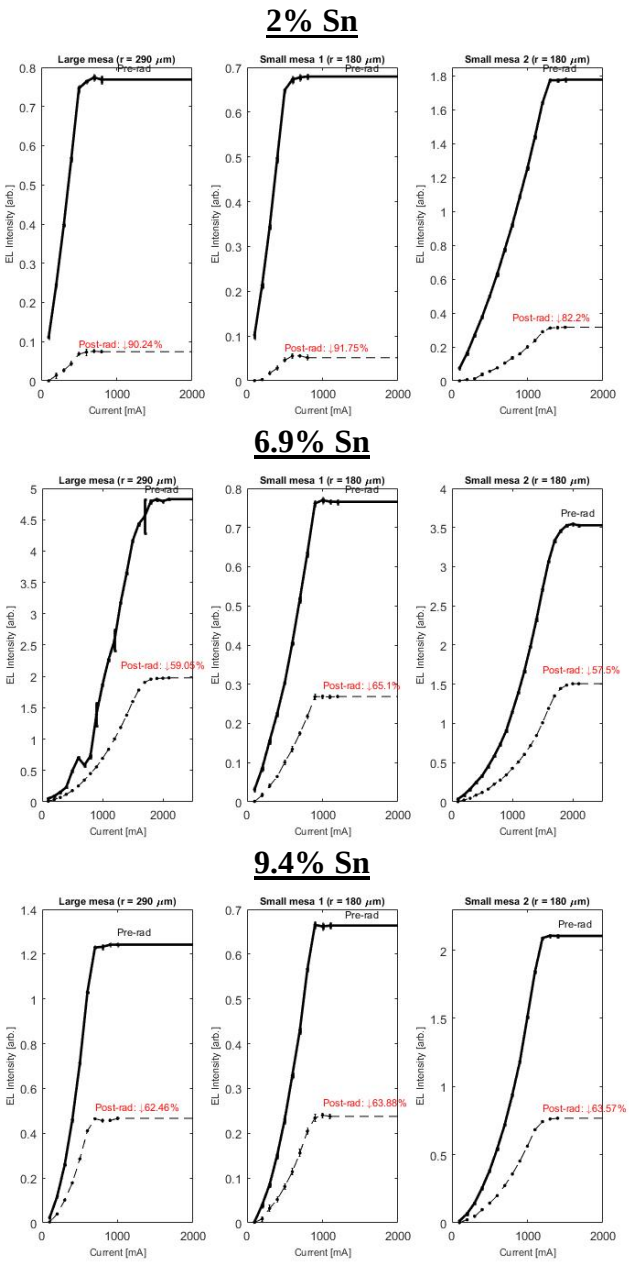

Figure 66. EL plots for various Sn samples which were irradiated at a proton fluence of 4×10^{14} cm^{-2}. Since all samples in this group were subject to a different annealing treatment (30 K increment annealing), EL data of the samples that were annealed at 393 K and 473 K could not be collected due to logistics and schedule restrictions. Hence, only the pre-rad and post-rad plots were compared in this figure.

Consolidated EL Summary (ΔEL versus Sn content)

Table 7. The numerical values of the ΔEL data which were used in Figure 24. The contents in this table are categorized by proton fluence level (low fluence (top) to high fluence (bottom)).

Sn Content [%]	ΔEL_{Avg} [%]	ΔEL_{Std} (1σ) [%]	95% CI [%]	2 MeV Proton Fluence [cm^{-2}]
0	20.690	5.134	49.48224	4×10^{12}
0	47.721	11.324	5.78072	4×10^{13}
2	39.216	8.147	6.837383	4×10^{13}
6.9	13.247	4.783	5.78072	4×10^{13}
9.4	12.315	7.135	5.093783	4×10^{13}
0	66.051	5.358	49.48224	2×10^{14}
6.9	46.874	0	0	2×10^{14}
0	86.703	1.688	13.68252	4×10^{14}
2	88.063	5.134	13.68252	4×10^{14}
6.9	60.550	4.016	7.363379	4×10^{14}
9.4	63.303	0.747	13.68252	4×10^{14}

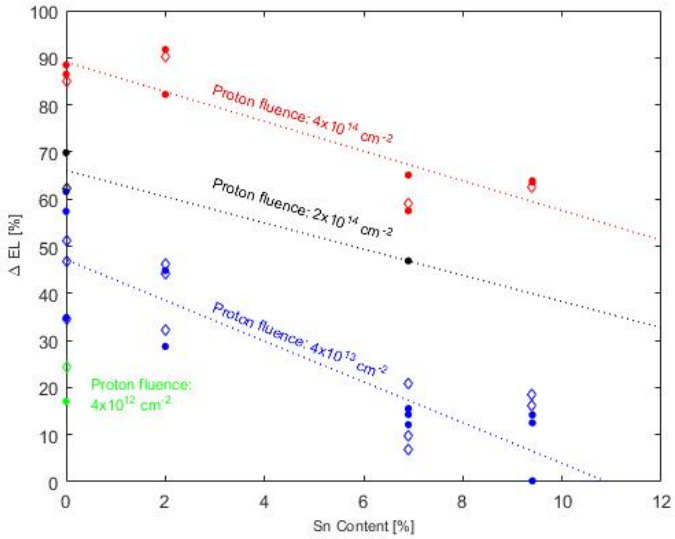

Figure 67. Organized pre-rad/post-rad ΔEL plots; their data depends on Sn content in the samples and irradiating proton fluence. Smaller device mesas were indicated by diamonds, and larger mesas were indicated by standard dots. The linear fits (dotted lines) were done with a combination of the smaller and the larger mesa data in the same fluence group. Three outliers (identified in the previous plot) were removed.

Consolidated EL Summary (ΔEL versus Proton Fluence)

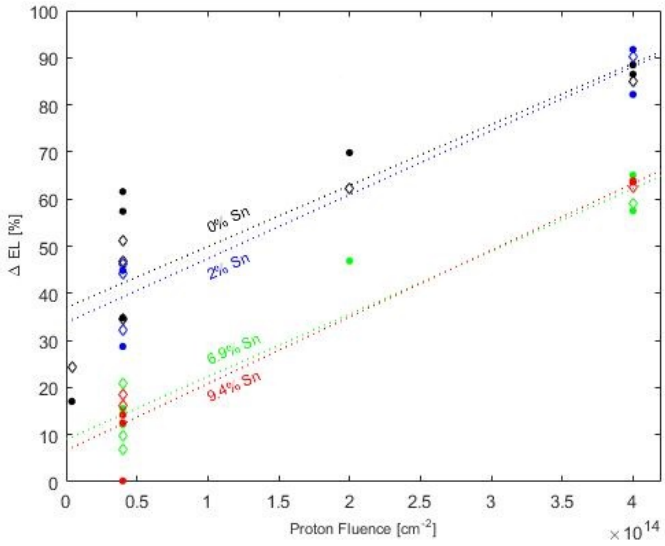

Figure 68. Plot showing how the various Sn samples' ΔEL depend on the irradiating proton fluence. Smaller device mesas were indicated by diamonds, and larger mesas were indicated by standard dots. The linear fits were done with a combination of the smaller and the larger mesa data of the same Sn group. Three corresponding outliers that were identified in the previous plots above were removed.

Annealing effects to ΔEL

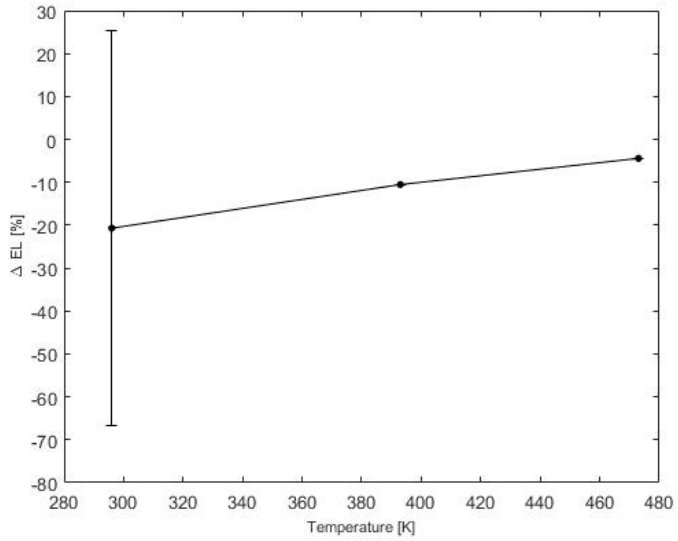

Figure 69. ΔEL and anealing temperature relationship. The 0% Sn sample was irradiated at 4 × 10^{12} cm^{-2}. The data points at 393 K and 473 K do not have error bars because the 95% CI could not be computed with a sample population of n = 1.

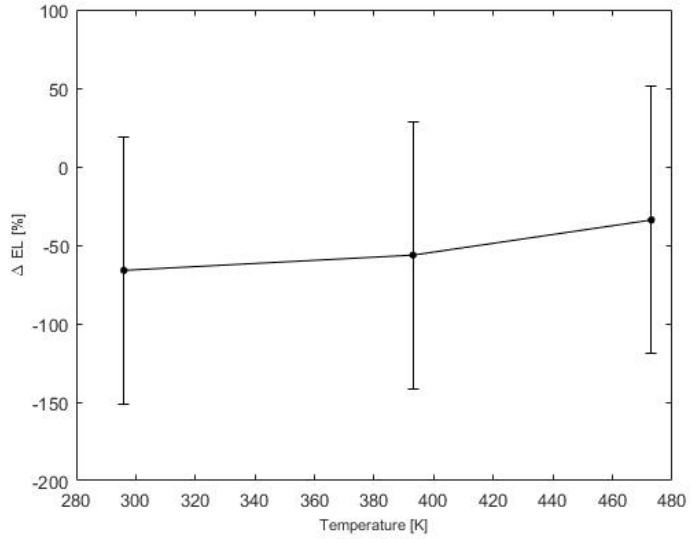

Figure 70. ΔEL and anealing temperature relationship. The 0% Sn sample was irradiated at 2 × 10^{14} cm^{-2}. The error bars are the 95% CI of each data point which has the sample population of n = 2.

C.3 C-V Data

C-V plots

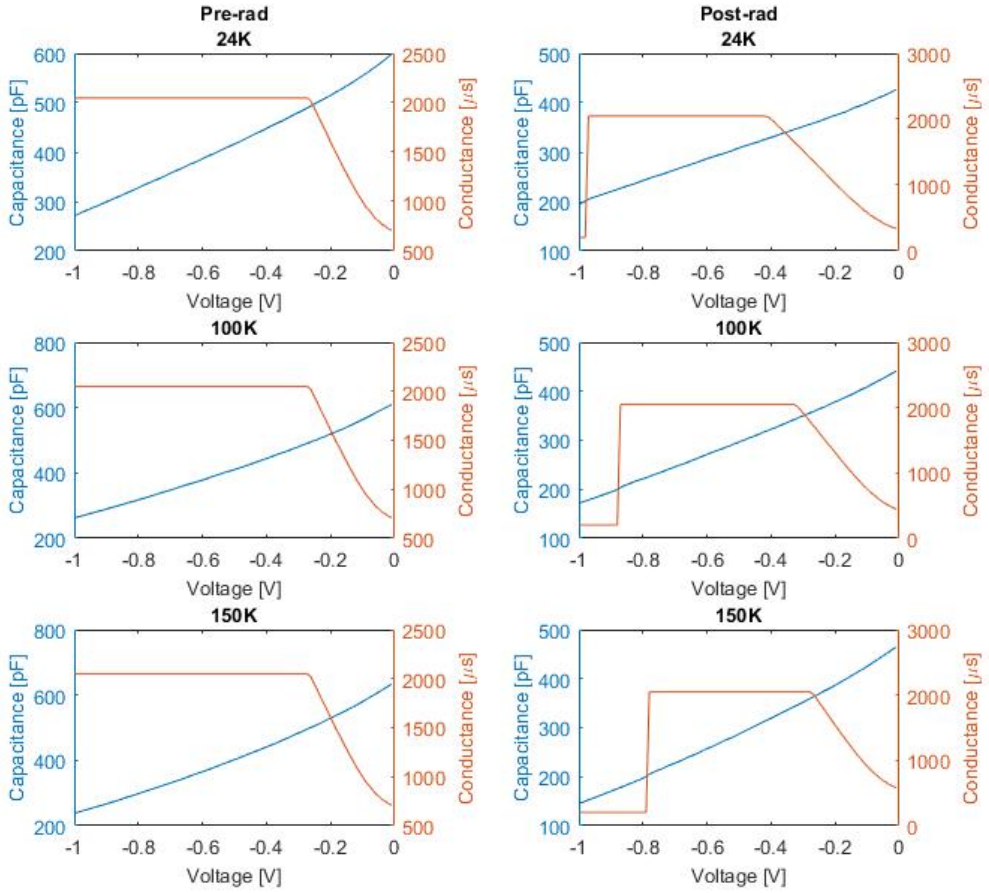

Figure 71. Pre-rad C-V plots (left) and post-rad C-V plots (right) representing a deviced on a 2% Sn sample irradiated at 4×10^{13} cm^{-2}. In each sequence, three measurements were taken of the sample at different temperatures: 24 K, 100 K, and 150 K.

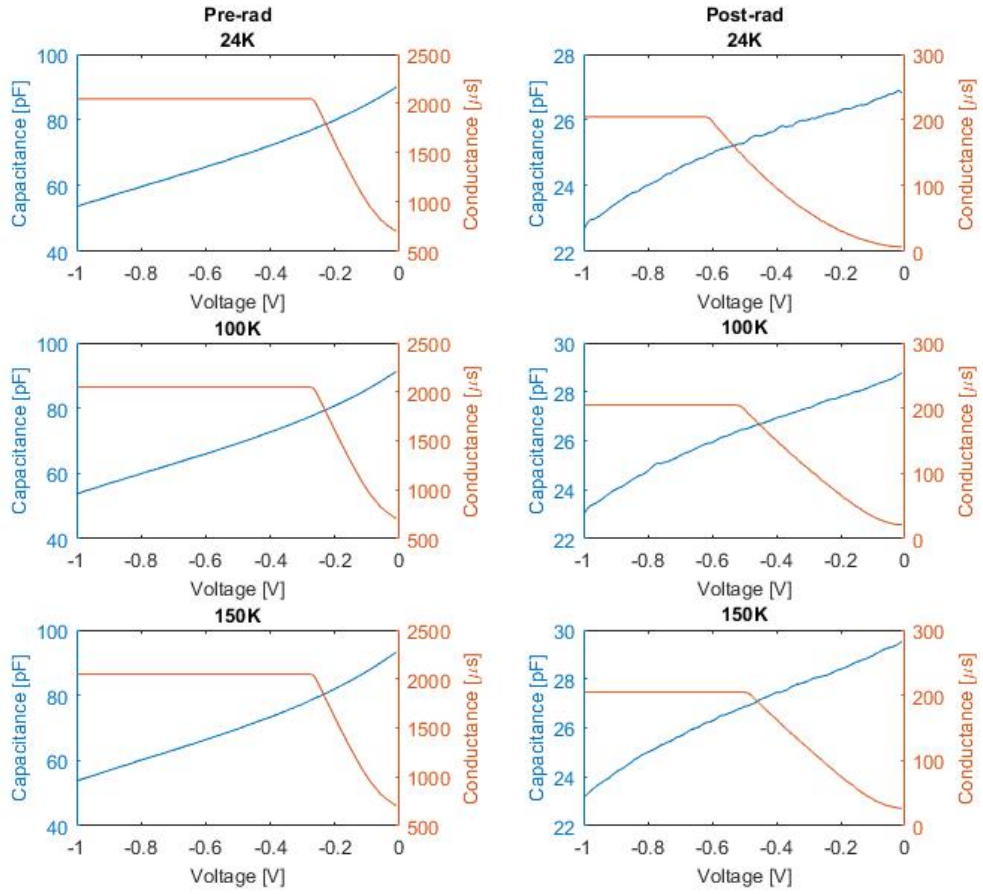

Figure 72. Pre-rad C-V plots (left) and post-rad C-V plots (right) representing a device on a 0% Sn sample irradiated at 4×10^{14} cm^{-2}. In each sequence, three measurements were taken of the sample at different temperatures: 24 K, 100 K, and 150 K.

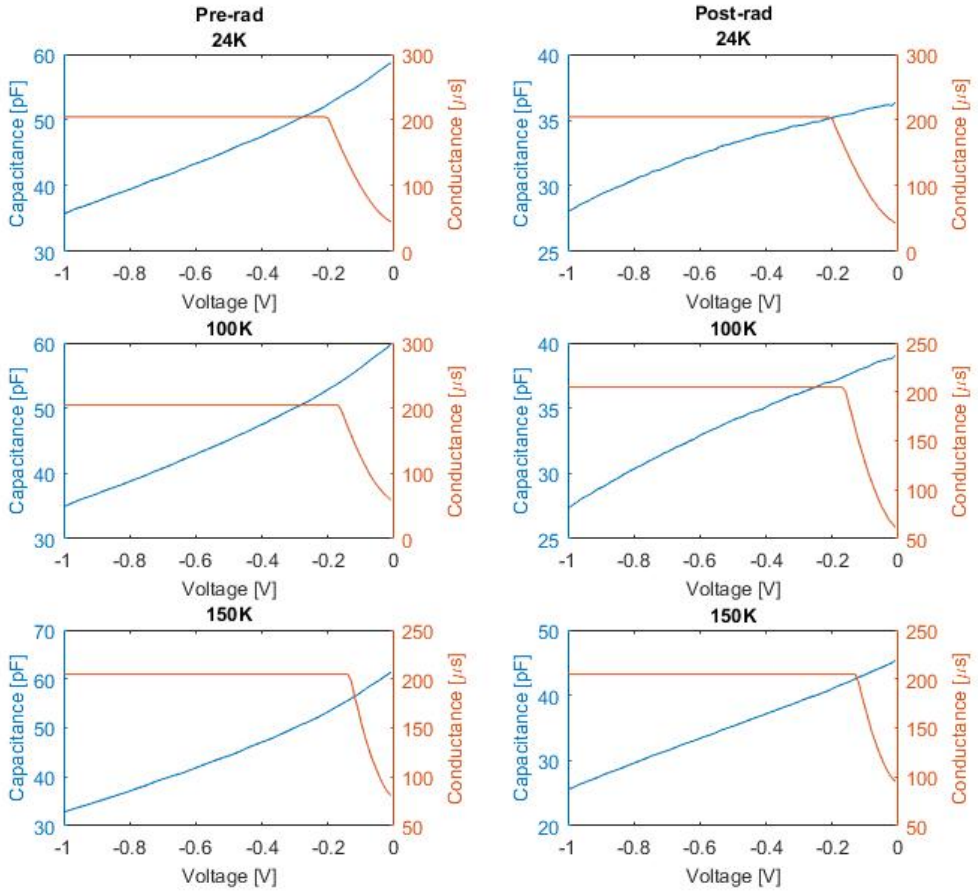

Figure 73. Pre-rad C-V plots (left) and post-rad C-V plots (right) representing a device on a 2% Sn sample irradiated at 4×10^{14} cm^{-2}. In each sequence, three measurements were taken of the sample at different temperatures: 24 K, 100 K, and 150 K.

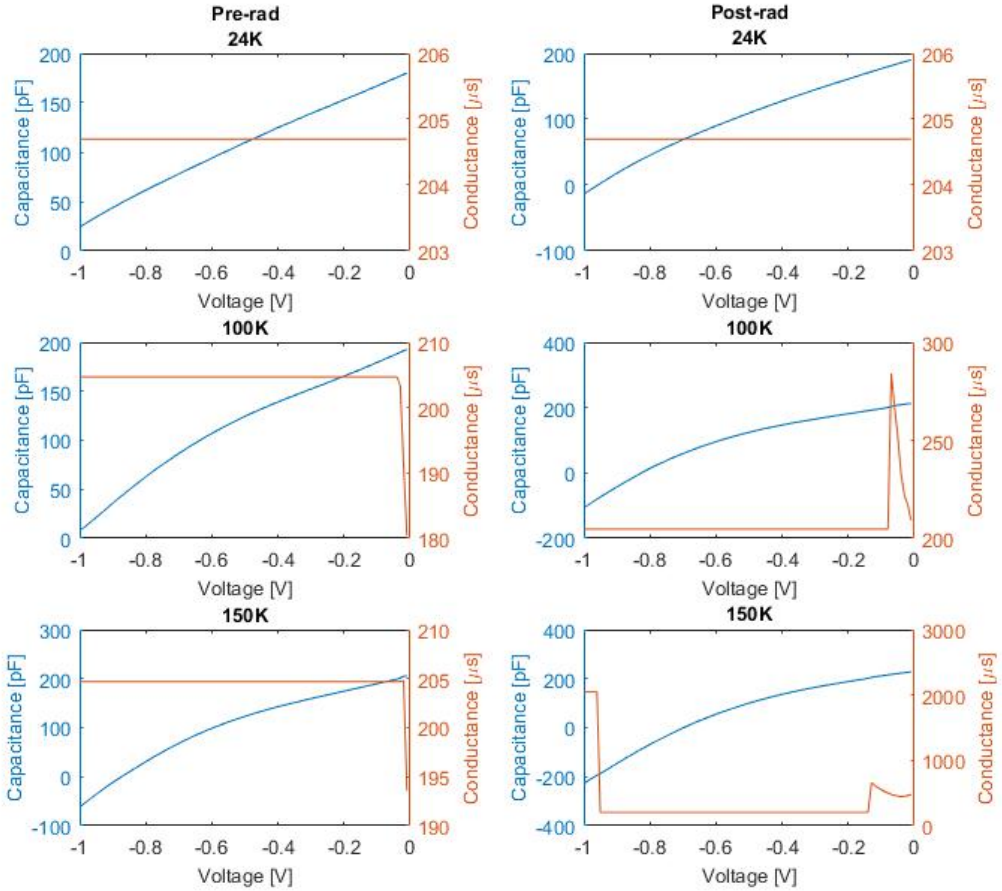

Figure 74. Pre-rad C-V plots (left) and post-rad C-V plots (right) representing a device on a 6.9% Sn sample irradiated at 4×10^{14} cm^{-2}. In each sequence, three measurements were taken of the sample at different temperatures: 24 K, 100 K, and 150 K.

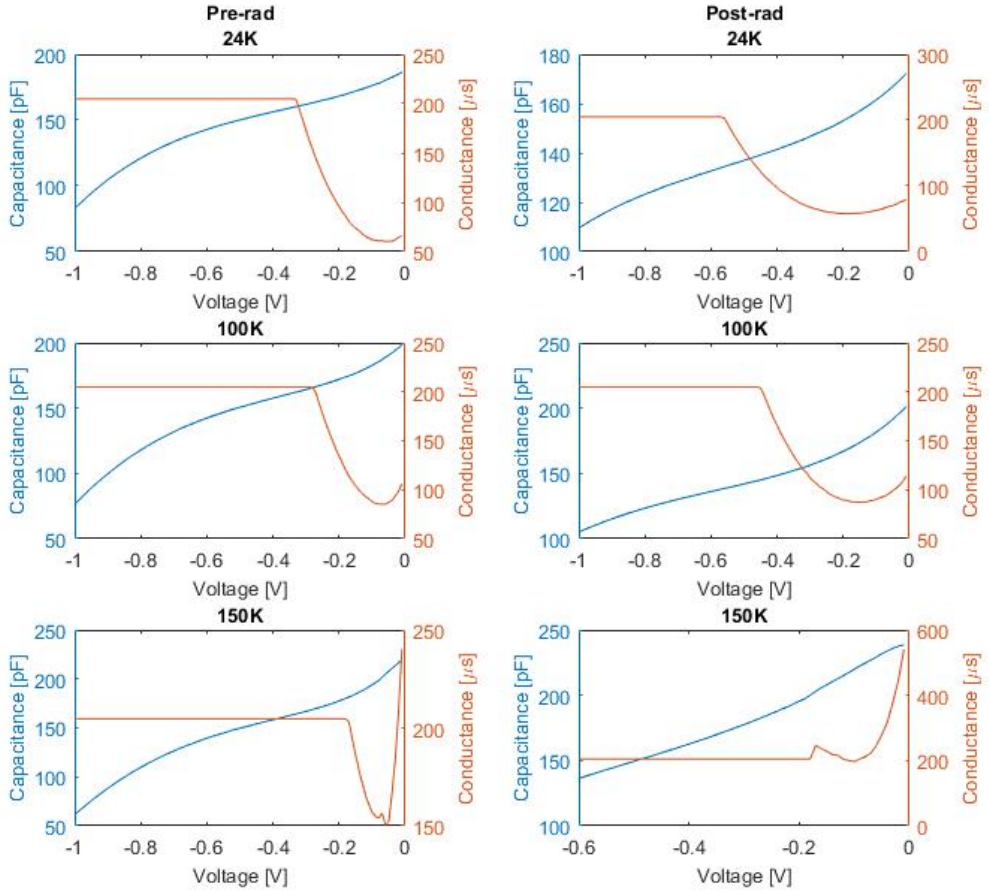

Figure 75. Pre-rad C-V plots (left) and post-rad C-V plots (right) representing a device on a 9.4% Sn sample irradiated at 4×10^{14} cm^{-2}. In each sequence, three measurements were taken of the sample at different temperatures: 24 K, 100 K, and 150 K.

Doping Profile Plots

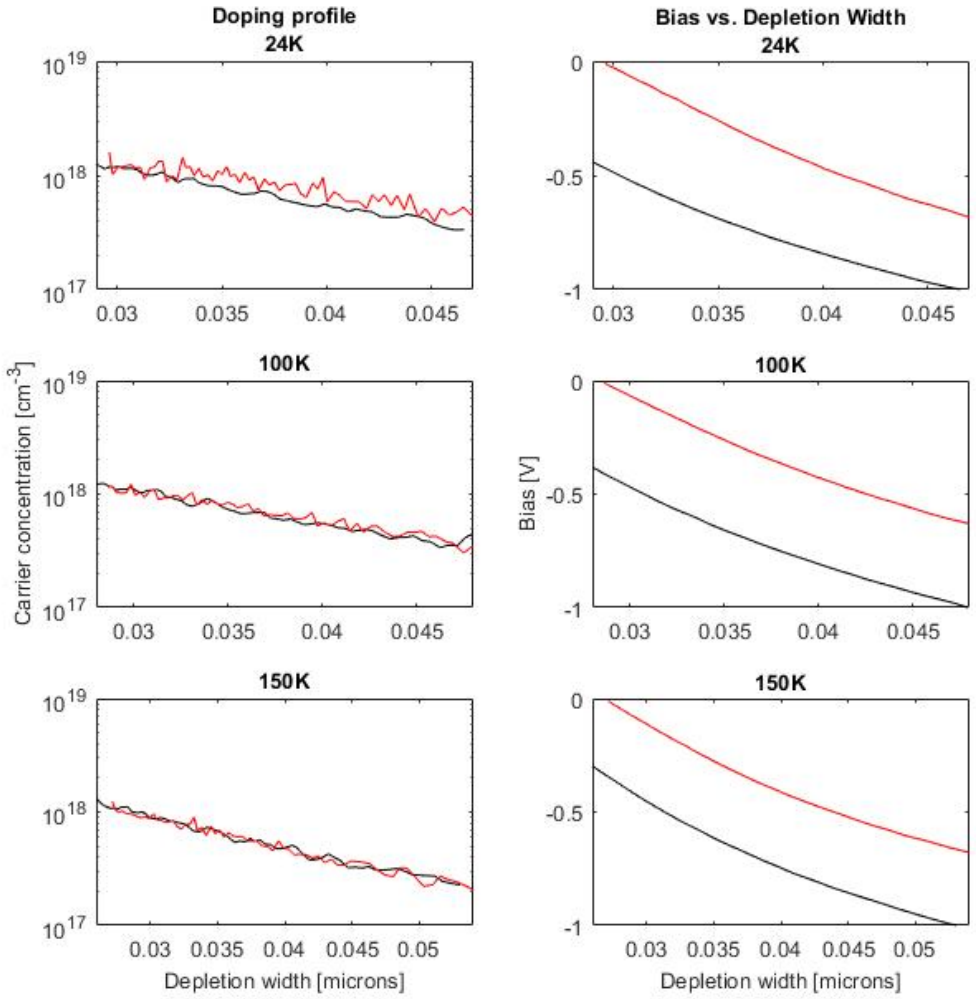

Figure 76. Doping Profile plots (left) and Bias vs. Depletion Width plots (right) representing a device on a 2% Sn sample irradiated at 4×10^{13} cm^{-2}. The standard plots represent pre-rad data, and the red plots represent post-rad data. In each sequence, three measurements were taken of the sample at different temperatures: 24 K, 100 K, and 150 K.

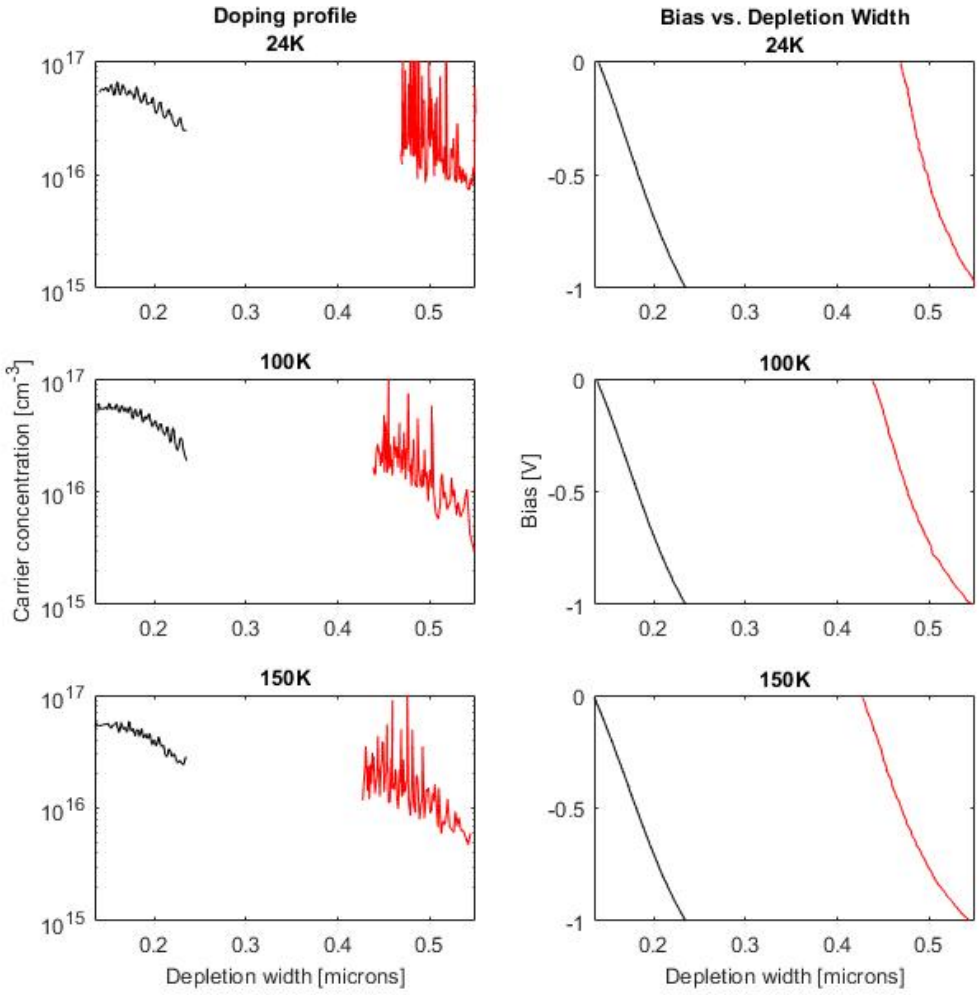

Figure 77. Doping Profile plots (left) and Bias vs. Depletion Width plots (right) representing a device on a 0% Sn sample irradiated at 4×10^{14} cm^{-2}. The standard plots represent pre-rad data, and the red plots represent post-rad data. In each sequence, three measurements were taken of the sample at different temperatures: 24 K, 100 K, and 150 K.

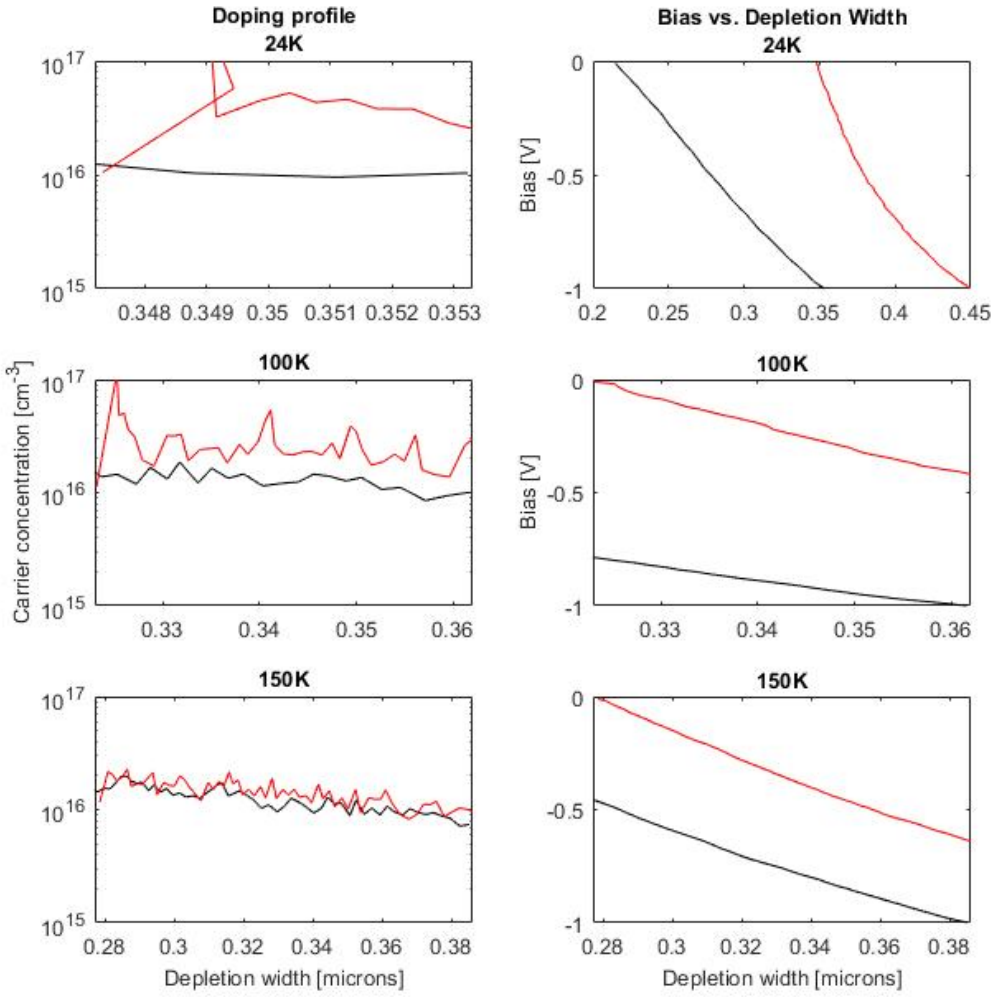

Figure 78. Doping Profile plots (left) and Bias vs. Depletion Width plots (right) representing a device on a 2% Sn sample irradiated at 4×10^{14} cm^{-2}. The standard plots represent pre-rad data, and the red plots represent post-rad data. In each sequence, three measurements were taken of the sample at different temperatures: 24 K, 100 K, and 150 K.

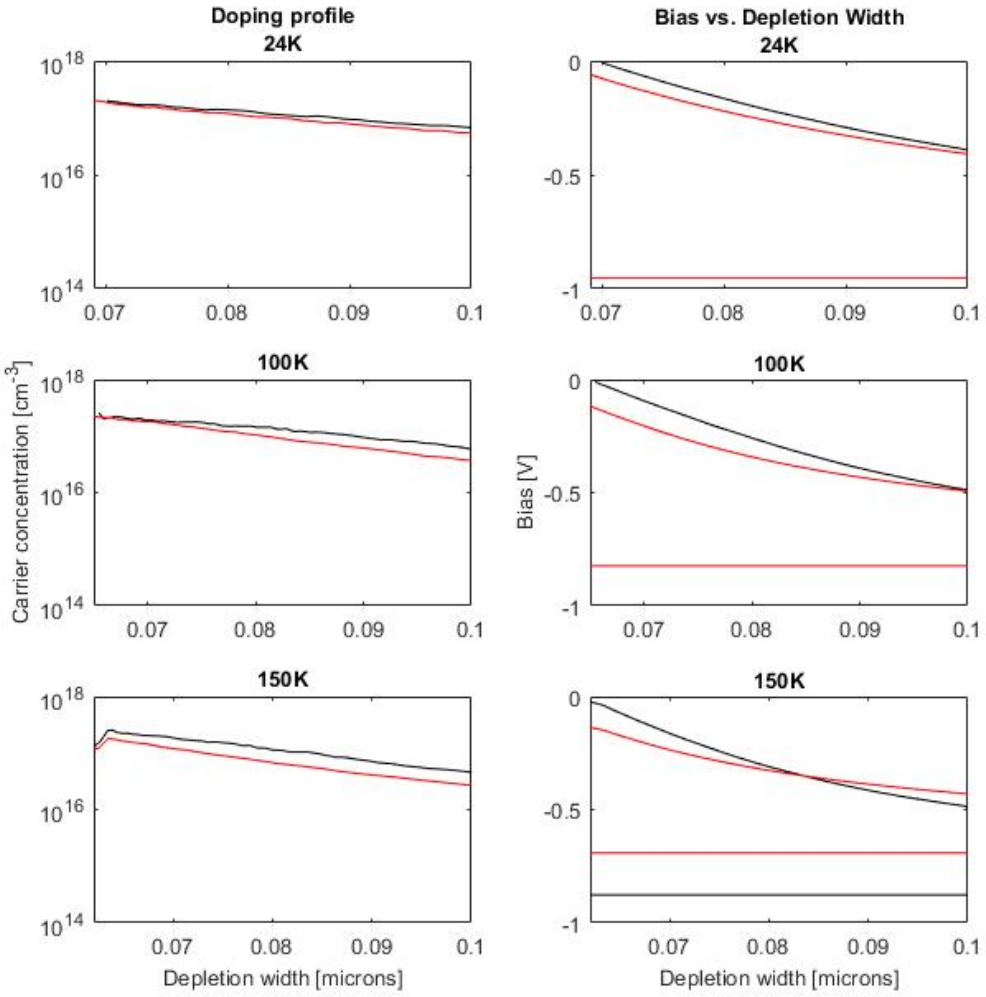

Figure 79. Doping Profile plots (left) and Bias vs. Depletion Width plots (right) representing a device on a 6.9% Sn sample irradiated at 4×10^{14} cm^{-2}. The standard plots represent pre-rad data, and the red plots represent post-rad data. In each sequence, three measurements were taken of the sample at different temperatures: 24 K, 100 K, and 150 K.

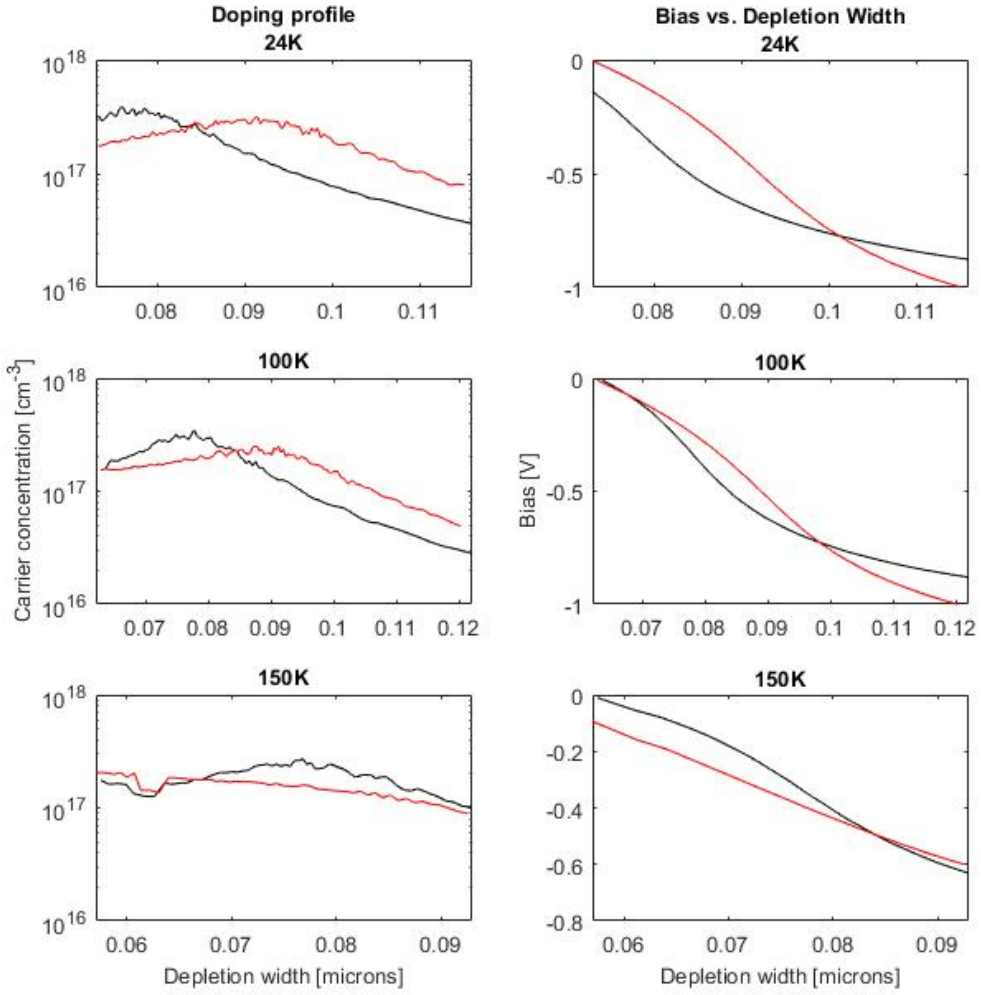

Figure 80. Doping Profile plots (left) and Bias vs. Depletion Width plots (right) representing a device on a 9.4% Sn sample irradiated at 4×10^{14} cm^{-2}. The standard plots represent pre-rad data, and the red plots represent post-rad data. In each sequence, three measurements were taken of the sample at different temperatures: 24 K, 100 K, and 150 K.

C.4 DLTS Data

0% Sn Rate-window Plot

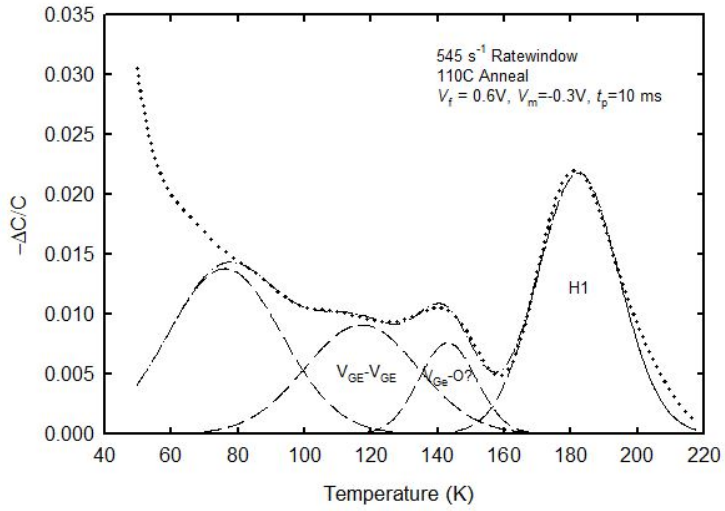

Figure 81. DLTS rate-window (545 s^{-1}) spectra of hole traps in a 0% Sn sample following 383 K anneal after 4 × 10^{14} cm^{-2} irradiation. The minority carrier (hole) spectrum was obtained by the current injection DLTS technique with parameters of V_f=0.6 V, V_m=-0.3 V, and 10 ms pulse width. The V_{Ge}-P peak is labeled H1.

2% Sn Rate-window Plot

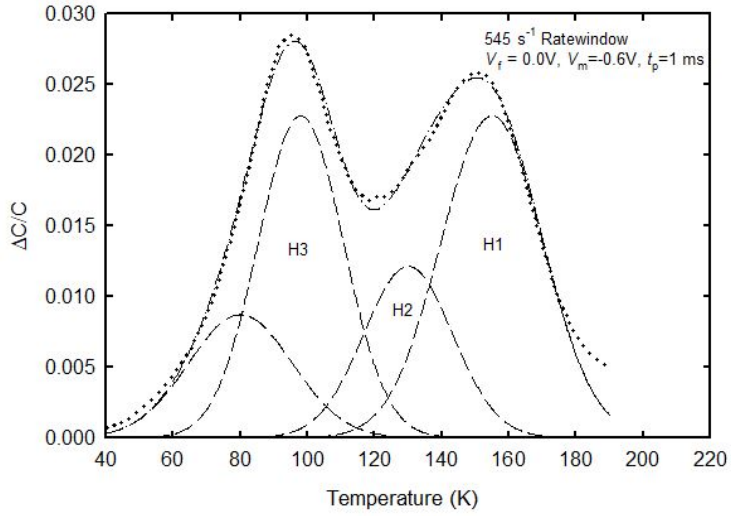

Figure 82. DLTS rate-window (545 s^{-1}) spectra of hole traps in a 2% Sn sample following 4 × 10^{14} cm^{-2} irradiation. The majority carrier spectrum was obtained by the traditional DLTS technique with parameters of V_f=0.0 V, V_m=-0.6 V, and 1 ms pulse width. The V_{Ge}-P peak is labeled H1; the V_{Ge}-V_{Ge} peak is labeled H2; the V_{Ge}-Sn peak is labeled H3.

5.3% Sn Rate-window Plot

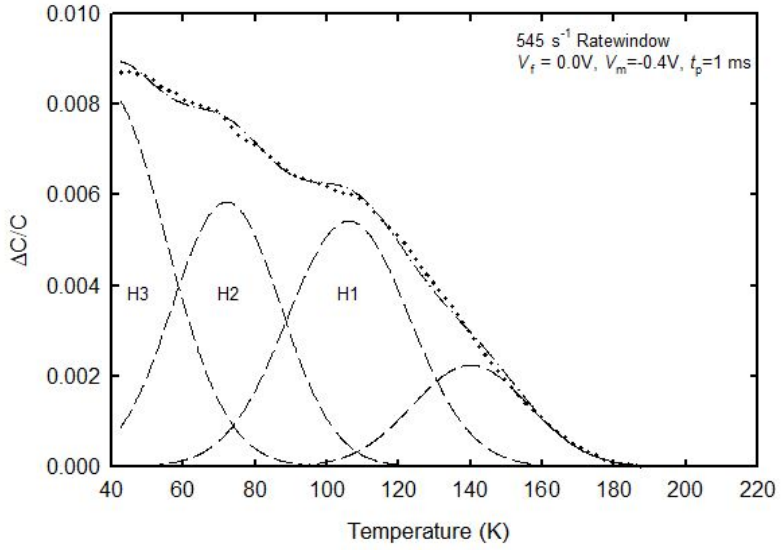

Figure 83. DLTS rate-window (545 s^{-1}) spectra of hole traps in a 5.3% Sn sample following 2 × 10^{14} cm^{-2} irradiation. The majority carrier spectrum was obtained by the traditional DLTS technique with parameters of V_f=0.0 V, V_m=-0.4 V, and 1 ms pulse width. The V_{Ge}-P peak is labeled H1; the VGe-VGe peak is labeled H2; the V_{Ge}-Sn peak is labeled H3.

6.9% Sn Rate-window Plot

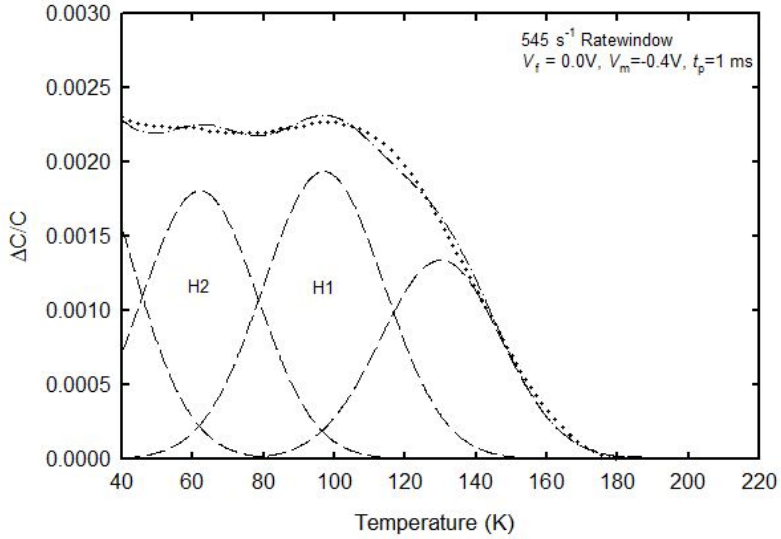

Figure 84. DLTS rate-window (545 s^{-1}) spectra of hole traps in a 6.9% Sn sample following 4 × 10^{14} cm^{-2} irradiation. The majority carrier spectrum was obtained by the traditional DLTS technique with parameters of V_f=0.0 V, V_m=-0.3 V, and 1 ms pulse width. The V_{Ge}-P peak is labeled H1; the V_{Ge}-V_{Ge} peak is labeled H2.

9.4% Sn Rate-window Plot

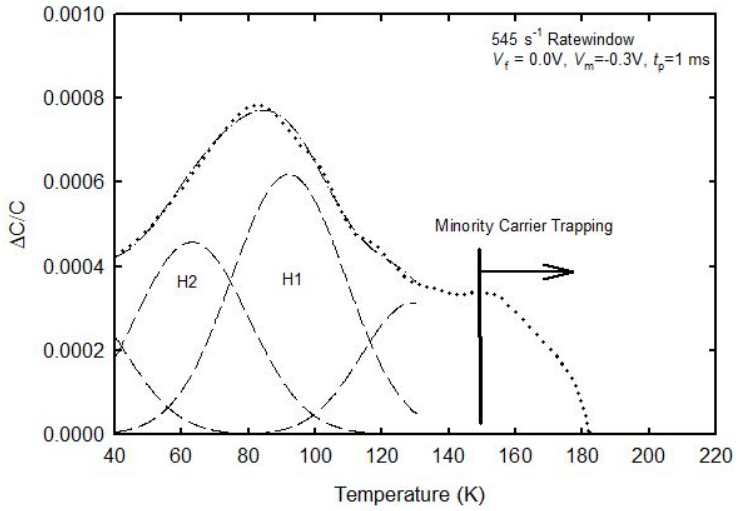

Figure 85. DLTS rate-window (545 s^{-1}) spectra of hole traps in a 9.4% Sn sample following 383 K anneal after 4 × 10^{14} cm^{-2} irradiation. The majority carrier spectrum was obtained by the traditional DLTS technique with parameters of V_f=0.0 V, V_m=-0.3 V, and 1 ms pulse width. The V_{Ge}-P peak is labeled H1; the V_{Ge}-V_{Ge} peak is labeled H2; the V_{Ge}-Sn peak is labeled H3.

Table 8. Summary of activation energies (determined for the presumed main peak within non-deconvoluted curve in DLTS rate-window plot) at each Sn concentration.

Sn Content [%]	No Deconvolve Main Peak Activation Energy [eV]	Activation Energy Uncertainty	$\sigma_{P\text{-}V\ trap}$ [cm^2]	Main 545 Hz Peak Temp [K]
0	0.36	0.02	1×10^{-13}	180
2	0.3	0.02	1×10^{-13}	156
5.3	0.2	0.01	5×10^{-13}	102
6.9	0.21	0.03	1×10^{-12}	98
9.4	0.125	0.02	1×10^{-14}	73

Bibliography

[1] E. G. Stassinopoulos and J. P. Raymond, "The space radiation environment for electronics," *IEEE*, vol. 76, no. 11, pp. 1423-1442, 1988.

[2] L. M. S. Martines, "Analysis of LEO Radiation Environment and its Effects on Spacecraft's Critical Electronic Devices," Embry-riddle Aeronautical University, Daytona beach, FL, 2011.

[3] J. Gallagher, C. Senaratne, C. Xu, P. Sims, D. Aoki, D. Smith and J. Menendez, "Electroluminescence from GeSn heterostructure pin diodes at the indirect to direct transition," *Appl. Phys. Lett.*, vol. 106, p. 091103, 2015.

[4] B. Wang, Z. Q. Fang, B. Claflin, J. Kouvetakis and K. Y. Yeo, ""Electrical characterization and deep-level transient spectroscopy of Ge0.873Si0.104Sn0.023 photodiode grown on Ge platform by ultra-high vacuum chemical vapor deposition," *Thin Solid Films*, vol. 654, pp. 77-84, 2018.

[5] S. Gupta, E. Simoen, Y. S. R. Loo, C. Porret, F. Gencarelli, K. Paredis, H. Bender, J. Lauwaert and H. Vrielinck, "Electrical properties of extended defects in strain relaxed GeSn," *Appl. Phys. Lett.*, vol. 113, p. 022102, 2018.

[6] M. Ryu, M. Ahoujja, Y. Yeo, T. Harris, R. Beeler and J. Kouvetakis, "Degenerate parallel conducting layer and conductivity type conversion observed from p-Ge1−ySny (y = 0.06%) grown on n-Si substrate," *Appl. Phys. Lett.*, vol. 101, p. 131110, 2012.

[7] S. L. Rumyantsev, M. E. Levinshtein and M. Shur, Handbook series on semiconductor parameters, World Scientific Pub Co Inc, 1996.

[8] R. F. Pierret, Semiconductor Device Fundamentals, Pearson Education, Inc. and Dorling Kindersley Publishing Inc., 1996.

[9] R. Geiger, T. Zabel and H. Sigg, "Group IV direct band gap photonics: methosd, challenges, and opportunities," *Frontiers in Materials*, vol. 2, pp. Article 52, 18pgs, 2015.

[10] T. R. Harris, M.-Y. Ryu, Y. K. Yeo, B. Wang, C. L. Senarathne and J. Kouvetakis, "Direct bandgap cross-over point of Ge1-ySny grown on Si estimated through temperature-dependent photoluminescence studies," *Journal of Applied Physics,* vol. 120, p. 085706, 2016.

[11] J. Gallagher, C. Senaratne, C. Xu, P. Sims, D. Aoki, D. Smith, J. Menendez and J. Kouvetakis, "Non-radiative recombination in Ge1-ySny light emitting diodes: The role of strain relaxation in tuned heterostructure designs," *Journal of Applied Physics,* vol. 117, p. 245704, 2015.

[12] C. J. Marshall and P. W. Marshall, "DISPLACEMENT EFFECTS," in *PROTON EFFECTS AND TEST ISSUES FOR SATELLITE DESIGNERS*, Greenbelt, Maryland USA, NSREC, 1999, pp. 51-100.

[13] A. H. Johnston, "Proton Displacement Damage in Light-Emitting and Laser Diodes," in *RADECS 2000 Data Workshop*, Pasadena, California USA, 2000.

[14] A. H. Johnston, B. G. Rax and L. E. Selva, "Proton Degradation of Light-Emitting Diodes," *IEEE Transactions on Nuclear Science,* vol. 46, pp. 1781-1789, 2000.

[15] P. W. Marshall, C. J. Dale and E. A. Burke, "Space Radiation Effects on Optoelectric Materials and Components for a 1300 nm Fiber Optic Data Bus," *IEEE Trans. Nucl. Sci.*, vol. 39, no. 6, pp. 1982-1989, 1992.

[16] A. L. Barry, A. J. Houdayer, P. F. Hinrichsen, W. G. Letourneau and J. Vincent, "The Energy Dependence of Lifetime Damage Constants in GaAs LEDs for 1-500 MeV Protons," *IEEE Trans. Nucl. Sci.*, vol. 42, no. 6, pp. 2104-2107, 1995.

[17] D. K. Schroder, "The concept of generation and recombination lifetimes in semiconductors," *IEEE,* vol. 29, no. 8, pp. 1336-1338, 1982.

[18] C. T. O'Daniel, "NEUTRON RADIATION EFFECTS ON Ge AND GeSn SEMICONDUCTORS," AFIT/ENP, Dayton,OH, 2016.

[19] P. W. Marshall, C. J. Dale, G. P. Summers and E. A. Wolicki, "Proton, neutron, and electron-induced displacement damage in germanium," *IEEE transactions on nuclear science,* vol. 36, no. 6, pp. 1882-1888, 1989.

[20] J. D. Gallagher, C. Xu, C. L. Senaratne, T. Aoki, P. M. Wallace, J. Kouvetakis and J. Menéndez, "Non-radiative recombination in Ge1-ySny light emitting diodes: The role of strain relaxation in tuned heterostructure designs," *J. Appl. Phys.*, vol. 117, p. 245704, 2015.

[21] J. Mathews, "Investigation of Light Absorption and Emission in Ge and GeSn Films Grown on Si Substrates," Arizona state university, Tempe, AZ, 2011.

[22] D. M. Lane , "Confidence Interval on the Mean," Rice University, University of Houston Clear Lake, and Tufts University, [Online]. Available: http://onlinestatbook.com/2/estimation/mean.html. [Accessed 24 January 2019].

[23] D. Johnstone, *DEEP LEVEL TRANSIENT SPECTROSCOPY: System User's Manual*, Semetrol, 2011.

[24] J. D. Gallagher, "The Optical and Electronic Properties of Ge1-ySny and Ge1-x-ySixSny Materials and Devices for Silicon-Integrated Optoelectronics," Arizona state university, Tempe,AZ, 2015.

[25] V. P. Markevich, A. R. Peaker, B. Hamilton, V. V. Litvinov, Y. M. Pokotilo, S. B. Lastovskii, J. Coutinho, A. Carvalho, M. J. Rayson and P. R. Briddon, "Tin-vacancy complex in germanium," *Journal of Applied Physics*, vol. 109, pp. 083705-1-6, 2011.

[26] V. Markevich, I. Hawkins, A. Peaker, K. Emtsev, V. Litvinov, L. Murin and L. and Dobaczewski, "Vacancy-goup-V-impurity atom pairs in Ge crystals doped with P, As, Sb, and Bi," *Physical Review B*, vol. 70, p. 235213, 2004.

[27] M. Mamor, M. Elzain, K. Bouziane and S. H. Al Harthi , "Deep-level transient spectroscopy study of the E center in n-Si and partially relaxed n-Si0.9Ge0.1 alloy layers," *PHYSICAL REVIEW B*, vol. 77, pp. 035213-1-7, 2008.

[28] L. Jiang, J. D. Gallagher, C. L. Senaratne, T. Aoki, J. Mathews, J. Kouvetakis and J. Menéndez, "Compositional dependence of the direct and indirect band gaps in Ge1−ySny alloys from room temperature photoluminescence: implications for the indirect to direct gap crossover in intrinsic and n-type materials," *IOP Publishing Ltd*, vol. 29, pp. 1-14, 2014.

[29] M. C. Peterson and A. N. Larsen, "Divacancy defects in germanium studied using deep-level transient spectroscopy," *PHYSICAL REVIEW* , vol. 82, pp. 075203-1-6, 2010.

[30] S. Zaima, O. Nkatsuka, N. Taoka, M. Kurosawa, W. Takeuchi and M. Sakashita, "Growth and applicaiton of GeSn-related group-IV semiconductor materials," *Sci. Techniol. Adv. Mater.*, vol. 16, pp. 1-22, 2015.

[31] J. D. Gallagher, C. Xu, C. L. Senaratne, T. Aoki, P. M. Wallace, J. Kouvetakis and J. Menéndez, "Ge1− x − y Si x Sn y light emitting diodes on silicon for mid-infrared photonic," *Journal of Applied Physics*, vol. 118, p. 135701, 2015.

[32] C. Nyamhere, A. G. M. Das, F. D. Auret, A. Chawanda, C. A. PinedaVargas and A. Venter, "Deep level transient spectroscopy (DLTS) study of defects introduced in antimony doped Ge by 2 MeV proton irradiation," Physica B, Port Elizabeth, 6031, South Africa, 2011.

[33] J. F. Ziegler, J. P. Biersack and M. D. Ziegler, SRIM: The Stopping and Range of Ions in Matter, Morrisville, NC: Lulu Press Co., 2015.

[34] LANL, "Qtool: Calculation of Reaction," LANL, 4 3 1997. [Online]. Available: https://t2.lanl.gov/nis/data/qtool.html. [Accessed 31 10 2018].

[35] J. L. Barth, C. S. Dyer and E. G. Stassinopoulos, "Space, Atmospheric, and Terrestrial Radiation," *TRANSACTIONS ON NUCLEAR SCIENCE,* vol. 50, pp. 466-482, 2003.

[36] D. Johnstone, *CURRENT-VOLTAGE-TEMPERATURE CHARACTERIZATION: System User's Manual*, SEMETROL, 2011.

[37] R. Hull and J. C. Beam, Germanium Silicon: Physics and Materials, Semiconductor and Semi-metals Vol. 56, San Diego, 1999.

[38] R. Soref, "Mid-infrared photonics in silicon and germanium," *Nat. Photonics*, vol. 4, pp. 495-497, 2010.

[39] J.-M. Belloir, V. Goiffon, C. Virmontois, P. Paillet, M. Raine, P. Magnan and O. Gilard, "Dark Current Spectroscopy on Alpha Irradiatiated Pinnes Photodiode

CMOS Image Sensors," *IEEE Transitions on Nuclear Science, Institute of Electrical and Electronics Engineerins,* vol. 63, pp. 2183-2192, 2016.

[40] C.-T. Sah, R. N. Noyce and W. Shockley, "Carrier Generation and Recombination in p-n Junctions and p-n Junction Chatacteristics," *Proceedings of the IRE,* vol. 45, pp. 1228-1242, 1957.

[41] E. Kasper, K. M., M. Oehme and T. Arguirov, "Germanium tin: silicon photonics toward the mid-infrared," *Photonics Research,* vol. 1, pp. 69-76, 2013.

[42] G. R. Savich, "Analysis and Suppression of Dark Currents in Mid-Wave Infrared Photodetectors," University of Rochester , Rochester, New York , 2015.

[43] R. Widenhorn, M. Blouke, A. Weber, A. Rest and E. Bodegom, "Temperature dependence of dark current in a CCD," in *Proceedings of SPIE* , Portland, OR, 2002.

[44] A. Dalvi, N. P. Reddy and S. C. Agarwal, "TheMeyer–Neldelruleandhoppingconduction," *SolidStateCommunications,* pp. 613-615, 2011.

[45] M. E. Dunn, "Electrical Characterization of 4H-SiC p-n junction diodes," AFIT/ENP, Dayton, OH, 1995.

[46] H. Chen, P. Verheyen, P. De Heyn, G. Lepage, J. De Coster, S. Balakeishnan, P. Absil, G. Roelkens and J. Van, "Dark current analysis in high-speed germanium p-i-n waveguide photodetectors," *Journal of Applied Physics* , p. 119, 2016.

[47] W. He and Z. Celik-butler, "1/f noise and dark current components in HgCdTe MIS infrared detectors," *Solid-State Electronics,* vol. 39, pp. 127-132, 1996.

[48] R. Beeler, D. J. Smith, J. Kouvetakis and J. Menendez, "GeSiSn Photodiodes With 1eV Optical Gaps Grown on Si(100) and Ge(100) Platforms," *IEEE JOURNAL OF PHOTOVOLTAICS,* vol. 2, pp. 434-440, 2012.

[49] M. Verdun, G. Beaudoin, B. Portier, N. Bardou, C. Dupuis, I. Sagnes, R. Haidar, F. Pardo and J.-L. Pelouard, "Dark current investigation in thin P-i-N InGaAs photodiodes for nano-resonators," *Journal of Applied Physics* , p. 120, 2016.

[50] C.-T. Sah, R. Noyce and W. Shockley, "Carrier Generation and Recombination 1n P-N Junctions and P-N Junction Characteristics," *PROCEEDINGS OF THE IRE* , pp. 1228-1237, 1957.

[51] E. Kasper, J. Werner, M. Oehme, S. Escoubas, N. Burle and J. Schulze, "Growth of silicon based germanium tin alloys," *Thin Solid Films,* pp. 3196-3200, 2011.

[52] A. N. Larsen and A. Mesli, "Capacitance-transient spectroscopy on irradiation-induced defects in Ge," *Optica Applicata,* vol. XXXVI, no. 2-3, pp. 246-256, 2006.

[53] T. J. Anderson, A. D. Koehler, P. Specht, B. D. Weaver, J. D. Greenlee, M. J. Tadjer, J. K. Hite, M. A. Mastro, M. Porter, M. Wade, O. D. Duson, M. Luysberg, K. D. Hobert, T. R. Weatherford and F. J. Kub, "Failure Mechanisms in AlGaN/GaN HEMTs Irradiated with 2MeV Protons," in *CS MANTECH Conference*, Scottsdale, AZ, 2015.

[54] Z. Meisel, C. R. Brune, S. M. Grimes, D. C. Ingram, T. N. Massey and A. V. Voinov, "The Edwards Accelerator Laboratory at Ohio University," in *Conference on the Application of Accelerators in Research and Industry*, Ft. Worth, TX, 2016.

[55] S. M. Sze and K. K. Ng, Physics of Semiconductor Devices, Hoboken, NJ: John Wiley & Sons, Inc., 2007.

[56] C. Chang, H. Li, S.-H. Huang, L.-C. Lin and H.-H. Cheng, "Temperature-dependent electroluminescence from GeSn heterojunction light-emitting diode on Si substrate," *Japanese Journal of Applied Physics,* p. 55, 2016.

[57] M. Oehme, K. Kostecki, T. Arguirov, G. Mussler, M. Ye, M. Gollhofer, M. Schmid, M. Kaschel, A. Korner, M. Kittler, D. Buca and E. Kasper, "GeSn Heterojunction LEDs on Si Substrates," *IEEE photonic technology latters,* vol. 26, no. 2, pp. 187-189, 2014.

[58] J. Fage-Peferson and A. N. Larsen, "Irradiation-induced defects in Ge studies by transient spectroscopies," *Physical review B*, vol. 62, pp. 10117-10124, 2000.

[59] A. Alkauskas, M. D. McCluskey and C. G. Van de Walle, "Tutorial: Defects in semiconductors—Combining experiment and theory," *Journal of Applied Physics*, vol. 119, p. 181101, 2016.

[60] M.-Y. Ryu, T. R. Harris, Y. K. Yeo, R. T. Beeler and J. Kouvetakis, "Temperature-dependent photoluminescence of Ge/Si and Ge1-ySny/Si, indicating possible indirect-to-direct bandgap transition at lower Sn content," *Appl. Phys. Lett.* , vol. 102, p. 171908, 2013.

[61] H.-J. Jo, G. H. Kim, J. S. Kim, M.-Y. Ryu and Y.-K. Yeo, "Observation of temperature-dependent heavy- and light-hole split direct bandgap and tensile strain from GeSn using photoreflectance spectroscopy," *Current Applied Physics*, pp. 84-87, 2015.

[62] E. Simoen, F. De Stefano, G. Enenman, B. De Jaeger, C. Claeys and F. Crupi, "On the Temperature and Field Dependence of Trap-Assisted Tunneling Current in Ge p+n Junctions," *IEEE Electron Device Letters*, vol. 30, no. 5, pp. 562-564, 2009.

[63] University of Rochester, "urresearch.rochester.edu," The InAs-Based nBn Photodetector and Dark Current. [Online]. Available: https://www.google.com/url?sa=t&rct=j&q=&esrc=s&source=web&cd=1&ved=2ahUKEwjV3ZWM_OXdAhUS0IMKHX1FB3EQFjAAegQICRAC&url=https%3A%2F%2Furresearch.rochester.edu%2FfileDownloadForInstitutionalItem.action%3FitemId%3D12468%26itemFileId%3D28601&usg=AOvVaw2yrOE0ok. [Accessed 1 Oct 2018].

[64] Jesús del Alamo, "Lecture 4 - Carrier generation and recombination," in *Course materials for 6.720J Integrated Microelectronic Devices*, Cambridge, MA , Massachusetts Institute of Technolog, 2007, pp. 2-19.

[65] A. Sonzogni, D. Brown and E. McCutchan, "National Nuclear Data Center," Brookhaven National Laboratory, 1994. [Online]. Available: https://www.nndc.bnl.gov/. [Accessed 16 Oct 2018].

[66] T. F. Luera, J. G. Kelly, H. J. Stein, M. S. Lazo, C. E. Lee and L. R. Dawson, "Neutron Damage Equivalence for Silicon, Silicon Dioxide, and Gallium Arsenide," *IEEE Trans. Nucl. Sci.,* vol. 34, no. 6, pp. 1557-1563, 1987.

[67] P. J. Griffin, J. G. Kelly, T. F. Luera, A. L. Barry and M. S. Lazo, "Neutron Damage Equivalence in GaAs," *IEEE Trans. Nucl. Sci.,* vol. 38, no. 6, pp. 1216-1224, 1991.

[68] G. P. Summers, C. J. Dale, E. A. Burke, E. A. Wolicki, P. W. Marshall and M. A. Gehlhausen, "Correlation of Particle-Induced Displacement Damage in Silison," *IEEE Trans. Nucl. Sci.,* vol. 34, pp. 1134-1139, 1987.

[69] R. L. Pease, E. W. Enlow, G. L. Dinger and P. W. Marshell, "Comparison of Neutron and Proton Carrier Removal Rates," *IEEE Trans. Nucl. Sci.,* vol. 34, no. 6, pp. 1140-1146, 1987.

[70] C. J. Dale, P. W. Marshall, E. A. Burke, G. P. Summer and E. A. Wolicki, "High Energy Electron Induced Displacement Damage in Silicon," *IEEE Trans. Nucl. Sci.,* pp. 1208-1214, 1988.

[71] R. J. Walters, S. R. Messenger, G. Summers, E. A. Burke and C. J. Keavney, "Space Radiation Effects in InP Solar Cells," *IEEE Trans. Nucl. Sci.,* vol. 38, no. 6, pp. 1153-1158, 1991.

[72] H. Ohyama, J. Vanhellemont, Y. Takami, K. Hayama, T. Kudo, H. Sunaga, I. Hironaka, Y. Uwatoko, J. Poortmans and M. Caymas, "Degradation and Recovery of Proton Irradiated SiGe Devices," *IEEE Trans. Nucl. Sci.,* vol. 43, no. 6, pp. 3089-3096, 1996.

REPORT DOCUMENTATION PAGE

Form Approved
OMB No. 0704-0188

1. REPORT DATE *(DD-MM-YYYY)*	2. REPORT TYPE	3. DATES COVERED *(From - To)*
21-03-2019	Master's Thesis	Sept 2017 – Mar 2019

4. TITLE AND SUBTITLE
Displacement Damage Effects in GeSn Light Emitting Diodes

5a. CONTRACT NUMBER

5b. GRANT NUMBER

5c. PROGRAM ELEMENT NUMBER

6. AUTHOR(S)
Choe, Kevin K., Captain, USAF

5d. PROJECT NUMBER

5e. TASK NUMBER

5f. WORK UNIT NUMBER

7. PERFORMING ORGANIZATION NAME(S) AND ADDRESS(ES)
Air Force Institute of Technology
Graduate School of Engineering and Management (AFIT/ENP)
2950 Hobson Way, Building 640
WPAFB OH 45433-8865

8. PERFORMING ORGANIZATION REPORT NUMBER
AFIT-ENP-MS-19-M-073

9. SPONSORING/MONITORING AGENCY NAME(S) AND ADDRESS(ES)
Air Force Office of Scientific Research
AFOSR/RTB1
8725 North Randolph Street
Arlington, Virginia 22203-1768

10. SPONSOR/MONITOR'S ACRONYM(S)
AFOSR/RTB1

11. SPONSOR/MONITOR'S REPORT NUMBER(S)

12. DISTRIBUTION/AVAILABILITY STATEMENT
DISTRUBTION STATEMENT A. APPROVED FOR PUBLIC RELEASE; DISTRIBUTION UNLIMITED.

13. SUPPLEMENTARY NOTES
This material is declared a work of the U.S. Government and is not subject to copyright protection in the United States.

14. ABSTRACT
Potential future use on Earth-orbiting satellites calls for investigation into the suitability of GeSn based photonic devices in high energy proton environments. The electroluminescence (EL) intensity of Ge1-xSnx (x = 0, 0.02, 0.069, and 0.094) light emitting diodes was measured before and after irradiation by 2 MeV protons at relatively high fluence levels. The results showed that GeSn devices with higher Sn content were up to 10 times more resistant against proton displacement damage than the pure Ge (x = 0) devices. As Sn concentration increased, the band gap decreased, and V-P hole trap energy level moved further from the mid-gap level, resulting in less EL degradation via Shockley Read Hall (SRH) process.

15. SUBJECT TERMS
Germanium Tin, LED, Semiconductor Radiation Effects, Displacement Damage, Proton, Electroluminescence

16. SECURITY CLASSIFICATION OF:			17. LIMITATION OF ABSTRACT	18. NUMBER OF PAGES	19a. NAME OF RESPONSIBLE PERSON
a. REPORT	b. ABSTRACT	c. THIS PAGE			Lt Col Michael R. Hogsed, AFIT/ENP
					19b. TELEPHONE NUMBER *(Include area code)*
U	U	U	UU	128	(937) 255-3636 x4547; Michael.Hogsed@afit.edu